AD 738489

DISTRIBUTION STATEMENT A
Approved for public release;
Distribution Unlimited

D D C
RECEIVED
MAR 27 1972
C

Reproduced by
NATIONAL TECHNICAL
INFORMATION SERVICE
Springfield, Va. 22151

UNCLASSIFIED

Security Classification

DOCUMENT CONTROL DATA - R & D

(Security classification of title, body of abstract and indexing annotation must be entered when the overall report is classified)

1. ORIGINATING ACTIVITY *(Corporate author)*
Lockheed Palo Alto Research Laboratory
Lockheed Missiles & Space Company, Inc.
Palo Alto, Calif. 94304

2a. REPORT SECURITY CLASSIFICATION
Unclassified

2b. GROUP

3. REPORT TITLE

HIGH-EFFICIENCY, SINGLE-FREQUENCY LASER AND MODULATOR STUDY

4. DESCRIPTIVE NOTES *(Type of report and inclusive dates)*
First Annual Technical Report, 1 September 1970 – 30 September 1971

5. AUTHOR(S) *(First name, middle initial, last name)*

Robert C. Ohlmann et al.

6. REPORT DATE
30 September 1971

7a. TOTAL NO. OF PAGES
95

7b. NO. OF REFS
21

8a. CONTRACT OR GRANT NO.
N00014-71-C-0049

b. PROJECT NO.
ARPA Order No. 306

c. Program Code No. 421

d.

9a. ORIGINATOR'S REPORT NUMBER(S)
LMSC-N-JY-71-8

9b. OTHER REPORT NO(S) *(Any other numbers that may be assigned this report)*

10. DISTRIBUTION STATEMENT

Distribution of this document is unlimited.

11. SUPPLEMENTARY NOTES

12. SPONSORING MILITARY ACTIVITY
Office of Naval Research
Physics Programs, Physical Sciences Division
Arlington, Va. 22217

13. ABSTRACT

Theoretical and experimental studies on (1) mode filters for single-frequency Nd:YAG lasers, (2) wide-bandwidth optical modulators, and (3) laser communication systems and components are reported. Stable single-frequency output power of 0.8 W is obtained from a Nd:YAG laser by using a combination of a tilted etalon and a thin metallic film in the laser cavity. Detailed analyses have been made to reduce the insertion loss of mode filters to an absolute minimum so that efficiency can be increased. The electrooptic modulator uses a microwave interdigital filter structure and has a 1.4-GHz bandwidth. A new circuit design aimed at increasing modulation depth for a given rf power has been obtained and tested. The results show that over 50% depth of modulation of 1.06-μm radiation is achievable with 10 W of rf drive power. No optical damage or beam distortion of $LiNbO_3$ was observed under continuous radiation of 14 kW/cm^2 green light when the crystal was at 180°C.

DD FORM 1 NOV 65 1473

UNCLASSIFIED

Security Classification

14. KEY WORDS	LINK A ROLE	LINK A WT	LINK B ROLE	LINK B WT	LINK C ROLE	LINK C WT
Lasers						
Solid-state lasers						
Neodymium						
Yttrium aluminum garnet						
Laser modes						
Laser communications						
Optical communications						
Wideband laser communications						
Laser modulators						
Optical modulators						
Electrooptic crystals						
Optical damage						
Laser communication system						

HIGH-EFFICIENCY, SINGLE-FREQUENCY LASER AND MODULATOR STUDY

First Annual Technical Report

N-JY-71-8 30 September 1971

R. C. Ohlmann, W. Culshaw, K. K. Chow, H. V. Hance,
W. B. Leonard, and J. Kannelaud

ARPA Order No. 306 Contract No. N00014-71-C-0049
Program Code 421
Effective Date of Contract: 1 September 1970
Expiration Date: 31 October 1972
Amount: $284,900
Scientific Officer: Director, Physics Programs,
Physical Sciences Division
Office of Naval Research, Arlington, Va. 22217
Principal Investigator: R. C. Ohlmann (415) 493-4411, ext. 45275

Sponsored by the
Advanced Research Projects Agency
ARPA Order No. 306

The views and conclusions contained in this document are those of the authors and should not be interpreted as necessarily representing the official policies, either expressed or implied, of the Advanced Research Projects Agency or the U.S. Government.

ABSTRACT

Theoretical and experimental studies on (1) mode filters for single-frequency Nd:YAG lasers and (2) wide-bandwidth optical modulators are reported. Stable single-frequency output power of 0.8 W was obtained from a Nd:YAG laser pumped by a 1-kW tungsten lamp. The mode filter consisted of a tilted etalon and a thin metallic film in the laser cavity. Detailed analyses have been made to reduce the insertion loss of mode filters to an absolute minimum so that efficiency can be increased. The electrooptic modulator uses a microwave interdigital filter structure and has a 1.4-GHz bandwidth. A new circuit design aimed at increasing modulation depth for a given rf power has been obtained and tested. The results show 74% depth of modulation of 0.51 μm light over the 1–2 GHz band using 5-W rf input. For 1.06 μm radiation, modulation depth of 52% can be achieved using 10-W rf input power. No optical damage or beam distortion of $LiNbO_3$ was observed under continuous radiation of 14 kW/cm^2 green light when the crystal was at 180°C.

CONTENTS

Section		Page
	ABSTRACT	ii
	ILLUSTRATIONS	iv
	TABLES	viii
1	INTRODUCTION	1-1
	1.1 General Comments	1-1
	1.2 Single-Frequency Nd:YAG Laser	1-2
	1.3 Wide-Bandwidth Optical Modulator	1-3
	1.4 List of Publications	1-7
2	SINGLE-FREQUENCY Nd:YAG Studies	2-1
	2.1 Introduction and Summary of Single-Frequency Laser Studies	2-1
	2.2 Tilted Fabry-Perot Etalon and Metallic Film Mode Selector	2-4
	2.2.1 Frequency Responses of Suitable Mode Filter Designs	2-4
	2.2.2 Tilt Loss of the Intracavity Fabry-Perot Etalon	2-7
	2.2.3 Insertion Loss of the Metallic Film – Reflector Etalon	2-12
	2.3 Double-Nichrome-Film Quartz Etalon Mode Filter	2-19
	2.4 Laser Cavity Design for Efficient Single-Frequency Nd:YAG Lasers	2-21
	2.5 Experimental Results	2-27
	2.5.1 Laser Design	2-27
	2.5.2 Tilted Fabry-Perot Etalon and Metallic-Film Mode Selector Experiments	2-29
	2.5.3 Double Metallic Film Mode Selector	2-34

Section		Page
	2.6 Comparison of Known and Potential Single-Frequency Techniques	2-35
	2.6.1 LMSC Two-Component Tilted Fabry-Perot Etalon and Metallic Film Mode Filter	2-35
	2.6.2 Uniform Cavity-Field Intensity Longitudinal Mode Technique	2-36
	2.6.3 Spatial Homogeneous Single-Frequency Operation by Translation of the Nd:YAG Rod	2-37
	2.6.4 Single-Frequency Operation by the Electrooptic Elimination of Spatial Hole Burning	2-38
	2.6.5 Other Potential Methods for Single-Frequency Operation	2-39
3	WIDE-BANDWIDTH OPTICAL MODULATOR	3-1
	3.1 Summary of Work Performed During the First Three Quarters	3-1
	3.1.1 Study of the Modulator Circuit	3-1
	3.1.2 Interferometric Modulation Studies	3-12
	3.1.3 Electrooptic/Thermal Control Circuit	3-14
	3.1.4 Beam Profile Studies in $LiNbO_3$ and Evaluation of Efficient Crystals	3-17
	3.2 Work Performed During the Fourth Quarter	3-19
	3.2.1 Study of the Modulator Circuit	3-19
	3.2.2 Crystal Fabrication	3-28
	3.2.3 Modification of the Electrooptic/Thermal Control Unit	3-29
	3.2.4 Crystal Damage Test	3-32
4	CONCLUSIONS AND RECOMMENDATIONS	4-1
	4.1 Single-Frequency Laser Studies	4-1
	4.2 Optical Modulator Studies	4-3
5	REFERENCES	5-1

ILLUSTRATIONS

Figure		Page
1-1	1- to 2-GHz Modulator, Showing Details of Electroptic Crystal Assembly for Automatic Electrooptical Bias	1-4
2-1	Tilted Fabry-Perot Etalon – Nichrome Film Mode Filter for Single-Frequency Nd:YAG Lasers. Total power reflection coefficient versus frequency deviation from resonance condition	2-5
2-2	Power Reflection Coefficients or Power Loss of the Tilted Fabry-Perot Etalon Versus Design Parameters for TEM_{oo} Mode	2-10
2-3	Single Metallic Layer Multilayer Reflector Etalon	2-13
2-4	Diagram Showing the Parameters Used for Computations on a Single Layer of the Reflecting System	2-13
2-5	Power Reflection and Transmission Coefficients of a 50-Å-Thick Ni-Cr Film on a 2-mm-Thick Quartz Etalon for Various Numbers N of Quarter-Wave Dielectric Layers on the Reflector Side	2-16
2-6	Power Reflection and Transmission Coefficients of a 100-Å-Thick Ni-Cr Film on a 2-mm-Thick Quartz Etalon for 13 and 9 Quarter-Wave Dielectric Layers on the Reflector Side	2-17
2-7	Double-Nichrome-Film Quartz Etalon Mode Filter for Single-Frequency Nd:YAG Lasers; Total Power Reflection Coefficient Versus Frequency Deviation From Resonance Condition	2-20
2-8	Use of Laser Rod As Intracavity Focusing Lens With Appropriate Curvatures R on Rod	2-23
2-9	Beam Spot Radius at the YAG Rod Versus Curved Mirror – Rod Distance d_1 for Various Mirror Radii R_1 and Focal Lengths of the Laser Rod	2-26
2-10	Increasing the TEM_{oo} Mode Volume in the Laser Rod With an Intracavity Focusing Lens	2-27
2-11	Nd:YAG Laser Configuration Used in Mode Selector Experiments	2-29

Figure		Page
2-12	Output Frequency Spectra of Operating Nd:YAG Laser	2-30
2-13	Output Frequency Spectra of Operating Nd:YAG Laser	2-32
2-14	Mode Selection Using Uniform Cavity-Field Intensity in the Rod	2-37
2-15	Arrangement Used for Demonstrating Electrooptic Elimination of Spatial Hole Burning. Two lithium niobate crystals with their c-axes as shown are modulating the phase of the standing wave pattern in the rod	2-38
2-16	Single Traveling Wave Ring Type Laser for Single-Frequency Operation of the Nd:YAG Laser Without Spatial Hole Burning	2-40
3-1	A Low-Pass Prototype Tchebyscheff Filter Circuit, Normalized to $\omega_1' = 1$ rad/sec and Generator Impedance $g_0 = 1\ \Omega$. Values of g's are: $g_0 = 1\ \Omega$, $g_1 = 0.6703$ F, $g_2 = 1.1926$ h, $g_3 = 2.3661$ F, $g_4 = 0.8419$ h, and $g_5 = 1.9841\ \Omega$	3-3
3-2	The Strip-Line Capacity-Loaded Interdigital Line Filter, Together With Its Generator and Load	3-4
3-3	An Approximate Equivalent Circuit for the Four-Element Capacity-Loaded Interdigital Line Filter	3-4
3-4	Approximate Equivalent Circuits of the Output Section of the Capacity-Loaded Interdigital Modulator. The electrooptic crystal serves as the resonating capacitance for the inductive length of the line	3-6
3-5	Modulator Circuit Design: Effective Generator Impedance, 19 Ω; Load Impedance, 19 Ω	3-9
3-6	A Four-Section Short-Step Tchebyscheff Transformer for 50:19 Ω Impedance Transformation	3-10
3-7	Input VSWR of Two 50:19 Ω Transformers Connected Back-to-Back	3-11
3-8	Input VSWR of the Modulator/Transformer Combination Shown in Fig. 3-4	3-11
3-9	Automatic Bias Control of Modulator	3-15
3-10	Modulation Index as a Function of Frequency of 5-W of rf Drive Power at the Input	3-20
3-11	Design Values for Modulator Model 2	3-22
3-12	Details of the Crystal Mount	3-23
3-13	Design of Transformer Model 2	3-24

TABLES

Table		Page
2-1	Power Reflection and Transmission Coefficients for a 50 Å Nichrome Film and Multilayer Reflector Etalon for Various Numbers N of Quarter-Wave Dielectric Layers	2-18
2-2	Power Reflection and Transmission Coefficients for a 100 Å Nichrome Film on a Multilayer Quartz Etalon	2-18

Section 1
INTRODUCTION

1.1 GENERAL COMMENTS

The research effort reported here has the broad objective of contributing to the development of wide-bandwidth, high-data-rate laser communication systems. Specifically, the investigation has followed three major tasks:

(1) Design, fabrication, test, and operation of mode filters for Nd:YAG solid state lasers so as to obtain at least 1-W output power in a single mode (single frequency) at 1.06 μm

(2) Analysis, design, fabrication, and test of a 1-GHz bandwidth optical modulator for 1.06-μm radiation

(3) Study and evaluation of laser communication system configurations and components that will lead to the formulation of realistic and appropriate objectives for component development

The selection of these tasks has been based on the concept that a realistic approach to the development of ultra-wideband laser communication systems must include developing a sufficiently stable and efficient laser source in the visible or near-infrared (a spectral region where fast, sensitive detectors are becoming available) and developing a broad-bandwidth efficient optical modulator.

The progress and results achieved during the first year of the contract are presented in depth in this report. The efforts have been primarily spent on the first two tasks, the single-frequency laser and the optical modulator. The work done on the communication system theoretical studies, Task 3, is included in a separate report.

The contract for this research has been extended in time and scope to specifically include optimization of the efficiency of the Nd:YAG laser and extending the bandwidth of the optical modulator to 2 GHz. Experimental and theoretical work to accomplish these extended objectives has started, and results will be reported in the Fifth Quarterly Report.

1.2 SINGLE-FREQUENCY Nd:YAG LASER

The solid-state laser using neodymium in yttrium aluminum garnet (Nd:YAG) has the greatest promise at present as an efficient modest-power source of coherent radiation and deserves development into a long-life, reliable space-qualified cw transmitter source. However, the output of the free-running cw laser is too noisy for use in a communication source; it exhibits both low-frequency perturbations and rf noise from the uncorrelated oscillation of many axial cavity modes within the broad frequency band (up to 50 GHz) where excess laser gain exists. Stable single-frequency operation is required to allow use of the laser as the source in a cw broadband communication system using a microwave subcarrier. One method of achieving single frequency operation is by the use of mode filters within the laser cavity.

Theoretical and experimental investigations have been conducted on mode filters of three types: Fabry-Perot etalons, thin metallic films, and metallic gratings. These are placed within the laser cavity to provide frequency selectivity while having low insertion loss for one axial mode, and thus allow single-frequency operation of the Nd:YAG laser. A detailed theoretical analysis of the frequency spectrum and loss characteristics of these filters, both singly and in combination, indicates that a good solution to the problem of efficiently providing 1-W output power in a single mode is the combination of a tilted Fabry-Perot etalon and a thin (50 to 100 Å) metallic film mode selector. The advantage of this combination is that the best properties of each are utilized to obtain the required selectivity for the single-frequency operation of the Nd:YAG laser at the 1-W level of output power, and with the requisite low insertion loss. Experiments with this two-component mode filter in our present Nd:YAG laser gave 0.8-W single-frequency output.

The 0.8-W single-frequency output power of the Nd:YAG laser was obtained using a tungsten lamp to pump the 5-mm-diam and 30-mm-long Nd:YAG rod in a spherical pumping enclosure. The rod was water-cooled using a flow rate and hydrodynamic design which gave minimum thermal and vibrational noise. The resonant cavity consisted of an etalon end mirror coated with a metal film (Ni-Cr) of about 50-Å thickness on one side and a high reflectance dielectric coating on the other, a tilted Fabry-Perot etalon, the Nd:YAG rod with a 25-cm curvature on one end, and a 5-cm-radius, 3.5-%-transmission end mirror. With this arrangement the TEM_{00} spot radius in the rod was 1.1 mm. The major experimental difficulty observed was the optical damage occurring on the 5-cm-radius mirror. More highly damage resistant mirrors are being procured to solve this problem.

A complete description of the work on single-frequency Nd:YAG lasers performed during the past year is given in Section 2. It includes the theoretical studies on losses and selectivity of the single longitudinal mode filters, the laser cavity designs for maximizing output power, the experimental results that have been obtained, and a comparison of the mode filter technique with other techniques for obtaining single-mode operation.

1.3 WIDE-BANDWIDTH OPTICAL MODULATOR

The optical modulator design that has been studied employs an electrooptic crystal in a 1.2-GHz bandwidth bandpass microwave interdigital filter structure, as shown in Fig. 1-1. Excellent results have been obtained at LMSC using this device, with $LiNbO_3$ as the modulating crystal, for the modulation of 0.6328- and 0.5145-μm laser radiation. Since the efficiency of the device drops at longer wavelengths, as is true of all electrooptic modulators, new techniques have been developed for increasing the efficiency for modulation of the 1.06-μm radiation from a Nd:YAG laser.

The approach that has been pursued is the investigation of rf filter designs having internal or terminal impedance characteristics different from conventional designs so that, for a given rf power-flow through the circuit, high rf voltage across the

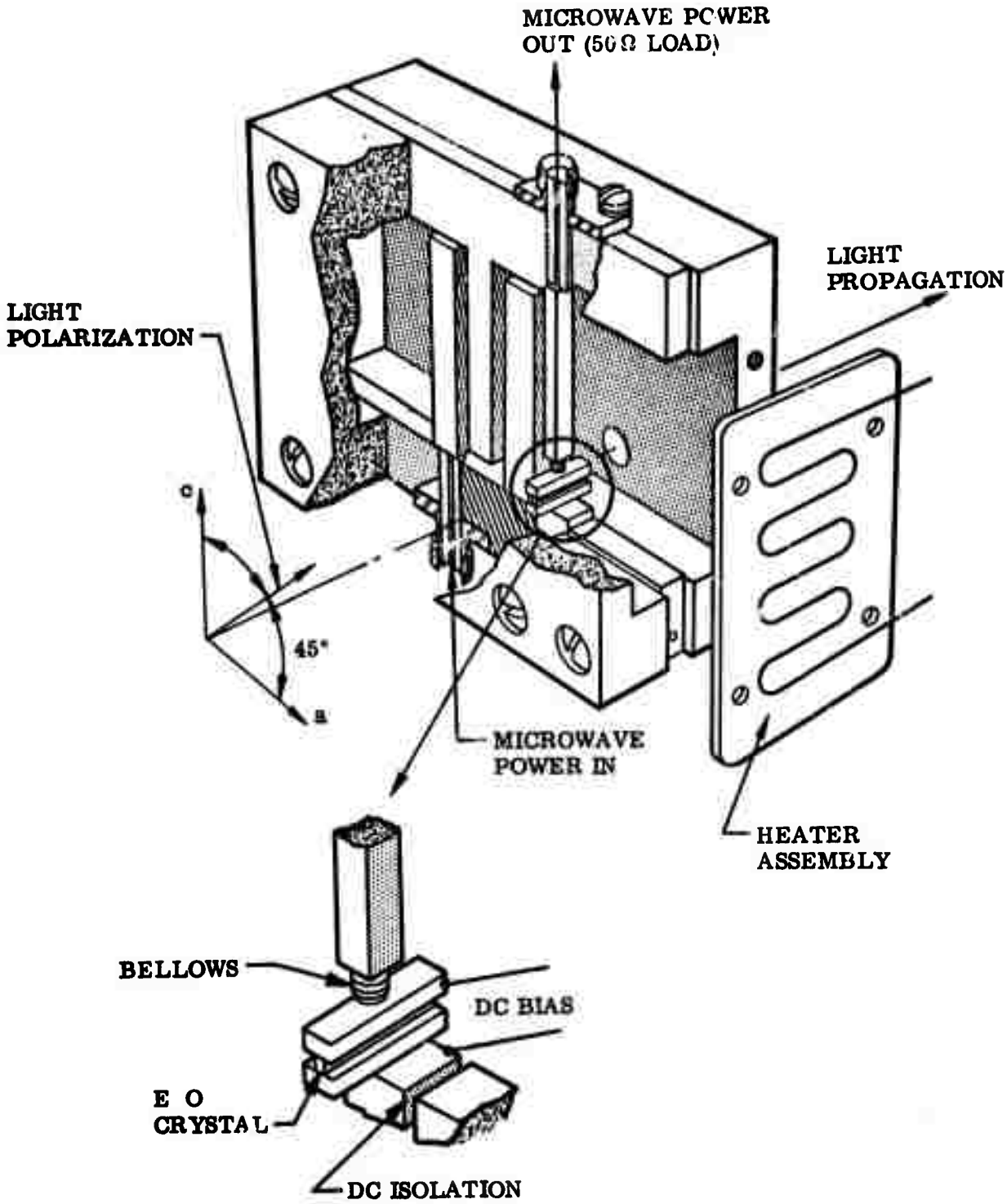

Fig. 1-1 1- to 2-HGz Modulator, Showing Details of Electrooptic Crystal Assembly for Automatic Electrooptical Bias

modulating crystal may be obtained. Unfortunately, conventional filter theory has been concerned primarily with terminal characteristics rather than internal characteristics. Therefore, for the internal characteristics to be varied as independent design parameters, new theoretical formulations had to be developed. We found that only a moderate change in conventional theory was required to achieve a design suitable for our purpose if the terminal characteristics were allowed to vary. A detailed discussion with our consultant, Professor George Matthaei, aided us in the theoretical reformulation. Basically, this approach allows the attenuation characteristics within the passband to be relaxed slightly so as to give more flexibility to the output-section design necessary to arrive at the desired higher rf voltage per unit power-flow. A computer design program was set up to obtain numerical designs for the modulator. From these designs, two modulators were fabricated and tested, yielding the following results.

For 0.5145-μm radiation, modulator Model 1 showed greater than 60% of modulation depth over a large portion of the band (3-dB bandwidth 865 MHz) for 3.6-W of rf power flowing through the circuit. Modulator Model 2, an improved design, showed 70% modulation depth for 3.6-W of rf power flowing through the circuit, and 87% modulation depth for 6.7-W power flow, with a 3-dB bandwidth of greater than 1 GHz. From these results, greater than 50% modulation depth at 1.06 μm can be attained using 7.5-W power-flow through the modulator.

Another approach that has been investigated for improving modulator efficiency is to use an interferometric mode of operation rather than the usual birefringence mode, the latter of which requires a polarizer to obtain intensity modulation. In the interferometric mode, the crystal, driven in the same interdigital filter structure, is part of a high-transmission Fabry-Perot etalon. Theoretical studies have indicated that increased efficiency is possible using this mode of operation. Uncoated $LiNbO_3$ crystals which had a reflectivity of 14% were first used for these experiments. The results showed good agreement with theory. Later, $LiNbO_3$ crystals of 30 to 35% end reflectivities were obtained for this use; such reflectivities appeared to represent the practical optimum for the currently obtainable crystals. Unfortunately, because of the imperfect parallelism of the end faces and internal beam distortion problems,

the results obtained were not significantly better than those for the 14% reflectivity case. Thus, the successful testing of this approach will have to await the availability of better quality crystals and cutting techniques.

For the interferometric mode, the optical bias point is determined by the optical length of the crystal and cannot be controlled by an external compensator as in the case of the birefringence mode. Therefore, a controller device must be used; such a device is also useful for birefringence modulation. Two controllers, of different control sensitivity, were designed, tested, and found to work well.

Some studies of more efficient electrooptic crystals for the modulator than $LiNbO_3$ were conducted. Small samples of barium sodium niobate (BANANA) and strontium barium niobate (SBN 50-50) suitable for the modulator were obtained from crystal growers. Static birefringence tests and preliminary modulation tests indicated that the optical quality of these materials was questionable. Nevertheless, because they were the only materials currently available, additional tests were made after these crystals had been antireflection (AR) coated for both 1.06- and 0.53-μm wavelengths. The strong rf absorption and dc conduction associated with the BANANA sample received rendered it unsuitable for our purposes; and the large capacitance associated with the SBN crystal made it impossible to match it to the present modulator circuit.

The problems of crystal optical damage and stability in vacuum also have been carefully examined. No optically induced damage occurred in $LiNbO_3$ when it was maintained at 170 to 180°C at optical power densities of 14 kW/cm^2 (0.4880- and 0.5145-μm radiation). Also, no measurable beam deviation from Gaussian was observed at these densities. The stability of $LiNbO_3$ in vacuum was good; no discoloration occurred. One sample of $Sr_{0.6}Ba_{0.4}(NbO_3)_2$ was found to discolor slightly at an optical intensity of 9 kW/cm^2. However, not enough data were gathered to determine whether this discoloration was an intrinsic property of SBN. Damage threshold for $LiTaO_3$ was also tested, and was found to be of the same order as $LiNbO_3$.

1.4 LIST OF PUBLICATIONS

The following is a list of publications of work that has been supported in part by this contract.

(1) P. S. Castro, K. K. Chow, H. V. Hance, W. B. Leonard, R. C. Ohlmann, S. E. Patterson, D. G. Peterson, R. B. Ward, and R. F. Whitmer, "A 1-Gbit/sec CW Laser Communication Experiment," Paper 13-B.8, IEEE/OSA Conference on Laser Engineering and Applications, Washington, D.C., 2–4 Jun 1971

(2) W. Culshaw and J. Kannelaud, "Two-Component Mode Filters for Optimum Single-Frequency Operation of Nd:YAG Lasers," IEEE JQE, Vol. QE-7, pp. 381–387, Aug 1971

(3) H. V. Hance, K. K. Chow, R. C. Ohlmann, D. G. Peterson, and R. B. Ward, "Modulation/Demodulation Techniques for an Optical 1-Gigabit/Second Inter-satellite Data Transmission System," presented at International Telemetry Conference, Washington, D.C., 27–29 Sep 1971

Section 2
SINGLE-FREQUENCY Nd:YAG STUDIES

2.1 INTRODUCTION AND SUMMARY OF SINGLE-FREQUENCY LASER STUDIES

These contractual efforts are directed to the development of an efficient, single-frequency Nd:YAG laser capable of 1 W output at 1.06 μm with relatively low values of unsaturated single-pass gains ($\leq$ 5%). The initial investigations have been made using a Nd:YAG rod pumped in a spherical pump cavity with a tungsten lamp at 1-kW input power. This pumping technique gives laser gains of 5% and also allows suitable structures, mode filters, and laser cavities to be designed for efficient operation.

The first quarterly report deals with the elimination of laser rod vibrations and with providing an adequate rate of cooling water flow along the laser rod for quiet stable operation. The importance of precise alignment of the rod with respect to the cavity mode was also emphasized. The application of single- and two-component mode filters to produce a single oscillation in the resonant laser cavity was also considered. Initial designs of a double-nichrome-film mode filter and of the tilted Fabry-Perot etalon-nichrome film mode filters were established.

The semiannual report deals with the optimization of these designs and with the possible use of a single, highly reflective (~ 75 to 85%) Fabry-Perot etalon for single-frequency operation in some instances. Here the idea of an angular spectrum of plane waves constituting the particular cavity mode was applied to deduce the intracavity tilt loss of such etalons as a function of beam waist size, etalon reflectivity, etalon thickness and tilt angle. Experimental results agreed with such computations and the work allowed the optimization of such etalon designs. Further work on the double-nichrome-film mode selector indicated its limitations and showed that the tilted F-P etalon-nichrome film construction represented a good practical solution for producing single-frequency operation of Nd:YAG lasers with low insertion loss.

The third quarterly report dealt with measurements on the threshold of the Nd:YAG lasers using the high reflectivity etalons for single-frequency operation. This showed that 85% reflectivity was too high due to the high insertion loss of the etalon, resulting in a considerable increase in the threshold of the laser. Furthermore, it was difficult to prevent the laser from using such a highly reflective etalon as the laser end mirror, in which case the etalon did not act as a single-frequency mode filter. Optimum designs for a 5-mm-thick, 60% reflective, tilted etalon in combination with a 64-Å nichrome film placed on a 2-mm thick quartz etalon were established. In addition, thicker F-P etalons of lower reflectivity were shown to be advantageous in some instances. Further experimental studies were performed on the double-nichrome-film mode filter which indicated its sensitivity to cavity perturbations and the difficulties in maintaining single-frequency operation with such a device.

It was also shown that the optimization of the single-frequency power output requires an adequate TEM_{00} mode volume within the laser rod to reduce the effects of saturation and to use efficiently the total population inversion within the laser rod. Optimum cavity designs were thus established using intracavity focussing elements and a short radius laser mirror. With cavity designs using one 10-cm-radius mirror and a plane mirror and with the rod end given a convex curvature to act as a focussing element, a TEM_{00} power output of 1.1 W at 1.06 μm was obtained using 1-kW input to a tungsten lams as the pump source in the spherical cavity. On inserting the tilted F-P etalon-nichrome film mode selecter, a single-frequency output of 0.5 W was obtained. Since the calculated mode radius in the rod is only 0.75 mm, the mode uses only a small portion of the 5-mm-diameter rod. Theory showed that this may be increased by using a 5-cm-radius mirror. When the mode radius in the rod increases to 1.05 mm, it was predicted that the TEM_{00} power would increase to 2 W and permit 1 W of single-frequency output to be attained.

To facilitiate reaching this objective, complete design curves for efficient single-frequency Nd:YAG lasers were deduced and were given in the third quarterly report. These showed that the two-component tilted Fabry-Perot etalon-nichrome film mode

filter developed at LMSC has a very small insertion loss (~ 0.1%) and will allow single-frequency outputs of 1 W to be obtained from low gain (~ 5%) Nd:YAG lasers. This is in contrast to some other schemes to be discussed later which make use of intracavity polarizers or Faraday rotators and which, in general, produce higher insertion losses. Other topics dealt with in the earlier reports included computerized solutions of the beam modes in cavities with internal focussing elements, and with the use of a laser output mirror with a continuously variable power transmission to measure the basic design parameters such as laser gain, insertion loss, and the saturation parameter of operating Nd:YAG lasers. The stabilization of the single-frequency laser using a Fabry-Perot etalon has also been considered, and the initial work done on incorporating the more efficient potassium-rubidium lamp pumping was also reported.

In what follows we shall elaborate on the basic ideas given here and report on the work done in the fourth quarter. First, we shall compare the two-mode filters developed and point out their respective advantages and limitations, giving the experimental results obtained on single-frequency operation. This will be followed with the results obtained with the more efficient 5-cm-radius mirror and with the difficulties encountered. With this mirror curvature a single-frequency power output of 0.8 W has been observed using tungsten lamp pumping, a result achieved because the laser rod was more adequately filled with the TEM_{00} mode. Some difficulties have been encountered with such short-radius mirrors and the rod radius (25 cm) used, especially when the F-P etalon is inserted and tilted. These are associated with the increased sensitivity of such laser cavities, and with the slight modification of the electric field of the mode due to tilted etalons. Such effects, which occur only in the more sensitive cavity designs, are presently under investigation.

Finally, some comparison is given of the LMSC mode filter approach with other known methods for single-frequency operation of the Nd:YAG lasers. This includes the use of a ring type, or traveling wave mode, of laser operation which might be beneficial because of its more efficient use of the population inversion, since spatial hole burning would then be eliminated.

2.2 TILTED FABRY-PEROT ETALON AND METALLIC FILM MODE SELECTOR

2.2.1 Frequency Responses of Suitable Mode Filter Designs

Figures 2-1a and 2-1b show the overall power reflection coefficient of the two component tilted F-P etalon-nichrome film, mirror etalon as a function of the frequency deviation from resonance. It is clear that the transmission curve of the tilted etalon may be made selective enough to suppress adjacent axial modes while the metallic film-laser mirror etalon falls off in reflectivity sufficiently so that oscillations at other resonances of the F-P etalon are suppressed. These additional resonances are spaced more closely for the thicker 11-mm F-P quartz etalon as shown in Fig. 2-1, but the lower reflectivity required with a thicker etalon for a given etalon selectivity is advantageous in some instances.

The power transmission curves and the selectivity Q for such F-P etalons may be deduced from the usual formulas (Ref. 2-1).

$$T = \frac{(1 - R)^2}{1 - 2R \cos 2 (k_z d + \psi) + R^2}$$

$$Q = \frac{\pi n d}{\lambda} \left(\frac{1 + R}{1 - R}\right) \tag{2.1}$$

where

k_z = $2\pi n/\lambda$
n = the refrective index
R = the reflectivity of the etalon surfaces
ψ = the phase shift in reflection

These formulas allow one to compare the transmission and selectivity of various etalons, as well as to deduce the overall power reflection coefficient of the etalon

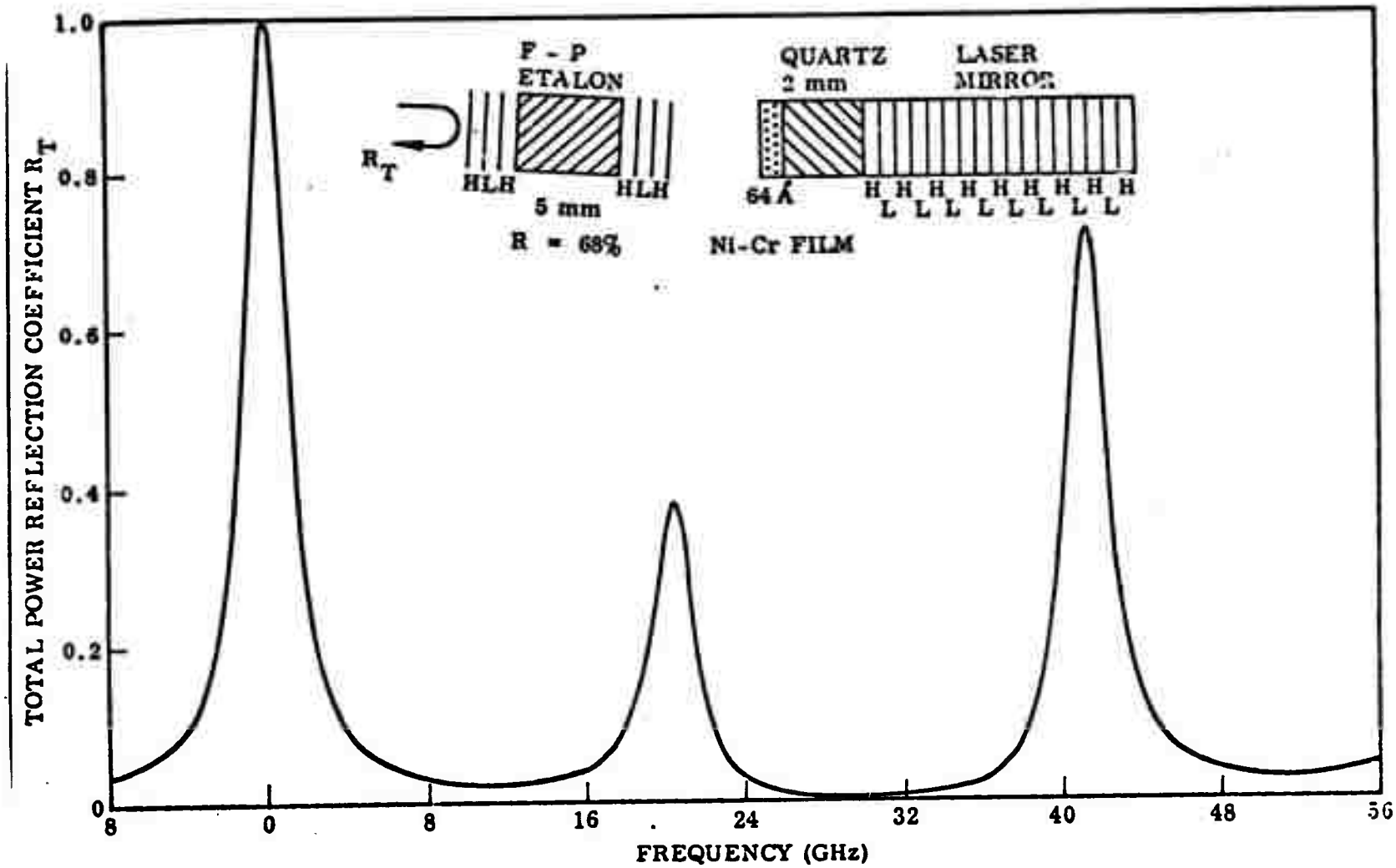

(a) Frequency Response for 5-mm, 68% Reflective Quartz F-P Etalon and 2-mm, 64% Å Nichrome Film-Laser Mirror Quartz Etalon

Fig. 2-1 Tilted Fabry-Perot Etalon – Nichrome Film Mode Filter for Single-Frequency Nd:YAG Lasers. Total power reflection coefficient versus frequency deviation from resonance condition

LOCKHEED PALO ALTO RESEARCH LABORATORY
LOCKHEED MISSILES & SPACE COMPANY
A GROUP DIVISION OF LOCKHEED AIRCRAFT CORPORATION

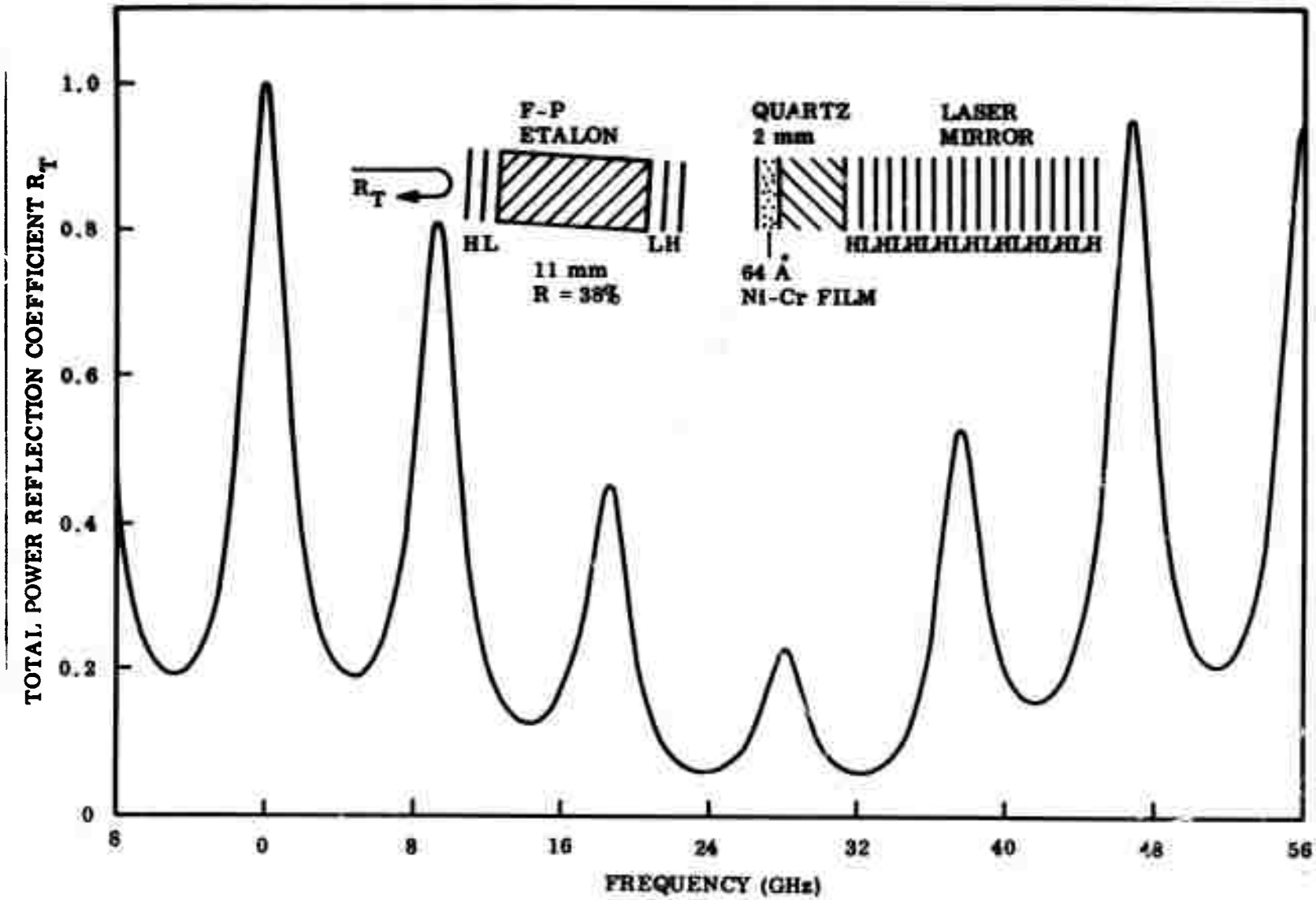

(b) Frequency Response for 11-mm, 38% Reflective Quartz F-P Etalon and 2-mm, 64 Å Nichrome Film-Laser Mirror Quartz Etalon

Fig. 2-1 (Cont.)

LOCKHEED PALO ALTO RESEARCH LABORATORY
LOCKHEED MISSILES & SPACE COMPANY
A GROUP DIVISION OF LOCKHEED AIRCRAFT CORPORATION

designs for frequencies well away from resonance. A more complete formulation dealing with the multilayer problem has been derived which gives the phases of the transmission and reflection coefficients.

Such mode filters for single-frequency operation of Nd:YAG lasers are adequate for the low-gain lasers (~ 5%) pertinent to the present development. The insertion losses are small and selectivity sufficient for suitable designs. The laser output may be taken through the nichrome film with very small losses at the desired operating frequency. Designs may be optimized for any desired cavity configuration.

For high gain lasers (20 to 30%), the etalon reflectivity and the axial mode spacing of the laser should be adjusted to avoid the possibility of the tilted etalon itself acting as the laser mirror. In this connection it may be shown that the 68% reflective etalon has an overall power reflection coefficient of 96.5% at minimum transmission, while the corresponding figure for the 38% reflective etalon is 80%. Such a possibility can be eliminated by tilting the F-P etalon so that reflections from it are outside the cavity mode. The additional tilt-loss introduced for the desired transmission mode of the etalon may not be too serious for such high gain lasers, but should be reduced as far as possible by using the largest possible axial mode spacing of the cavity resonances to reduce the selectivity required.

In general, such difficulties do not arise with the low gain lasers of primary interest. Etalon coating reflectivities of 35 to 60% with appropriate thicknesses of the quartz substrate give adequate selectivity for typical cavity configurations. Single-frequency operation has been achieved with relative ease for all but the more sensitive cavity configurations that have been used to boost up the TEM_{00} mode volume in the rod. These are under further investigation.

2.2.2 Tilt Loss of the Intracavity Fabry-Perot Etalon

Some discussion of the tilt loss was given in the semiannual report, where the use of the etalon as in transverse mode filter for modes TEM_{00} through TEM_{70} was indicated.

In that report the concept of the angular spectrum of plane waves, corresponding to the various modal distributions of the electric field in the cavity, was developed. For the desired TEM_{00} mode of operation, the electric field distribution and its associated angular spectrum at the waist position in the cavity are given by

$$E_x(x) = e^{-x^2/a^2}$$

$$B(k_x) = (2\sqrt{\pi})^{-1}\, a\, e^{-k_x^2 a^2/4} \tag{2.2}$$

where a is the radius of the beam waist, and k_x is the x component of the wave vector $\underline{k}$ corresponding to the direction of propagation of the given plane wave.

The power reflection and transmission coefficients of the tilted etalon have been deduced and are given by

$$P_r = \pi\eta_o \int \frac{|B(k_x)|^2\, 4\, R \sin^2 [(k_z' + k_z)\, d/(2 \cos \phi_t)]}{1 - 2\, R \cos [(k_z' + k_z)\, d/\cos \phi_t] + R^2}\, dk_x$$

$$P_t = \pi\eta_o \int \frac{|B(k_x)|^2\, (1 - R)^2}{1 - 2\, R \cos [(k_z' + k_z)\, d/\cos \phi_t] + R^2}\, dk_x \tag{2.3}$$

where

η_o = the admittance of free space

$k_z' = k_z \cos (2\, \phi_t) - k_x \sin (2\, \phi_t)$

$k_x = \left(k^2 n^2 - k_x^2\right)^{1/2}$,

n = the refractive index of the etalon

R = reflectivity

ϕ_t = the tilt angle

The integrals may be normalized such that $P_t = 1$ when $R = 0$. Normalized values which yield $P_t = 1$ and $P_r = 0$ when $R \neq 0$ then represent zero tilt loss in the etalon. Finite values of $P_t < 1$, and $P_r > 0$ correspond to insertion losses in the intracavity etalon and may be calculated as functions of the etalon parameters (reflectivity or selectivity, thickness, refractive index, and tilt angle) for various beam waist radii and modes of the cavity.

Figure 2-2a shows computed values of the tilt loss for a quartz etalon 1 cm thick as a function of its reflectivity for various TEM_{oo} mode waist radii, and for a typical tilt angle of 3 min. The importance of an adequate size of beam waist at the etalon is clearly emphasized by the curves. LMSC cavity designs produce beam waist radii of 0.8 to 1.0 mm at the etalon and use reflectivities of 30 to 60%. The requirement to use large beam waists to reduce losses is consistent with the requirement of an adequate beam spot size in the laser for efficient operation.

Curves of power reflection loss of the tilted etalon versus etalon length are shown in Fig. 2-2b for different waist sizes, an etalon reflectivity of 50%, and a tilt angle of 3 min. These results show that the power reflection loss is approximately proportional to L^2, where L is the thickness of the etalon. The designs being experimented with at LMSC will have relatively low insertion loss ~0.1% or better.

Figure 2-2c shows the tilt loss versus tilt angle for various waist sizes, an etalon thickness of 1 cm, and an etalon reflectivity of 50%. It is seen that for the smaller waist radii ~0.2 mm, some loss occurs even at normal incidence or zero tilt angle. The insertion losses are small for the nominal values of tilt angle ~3 min used in practice with our 5%-gain Nd:YAG lasers. Finally, Fig. 2-2d shows the tilt loss as a function of the refractive index of the etalon substrate for a reflectivity of 50%, an etalon thickness of 1 cm, and a tilt angle of 3 min. It is clear from these curves and Eq. (2.1) that the tilt loss of the etalon can be reduced, for a given selectivity and

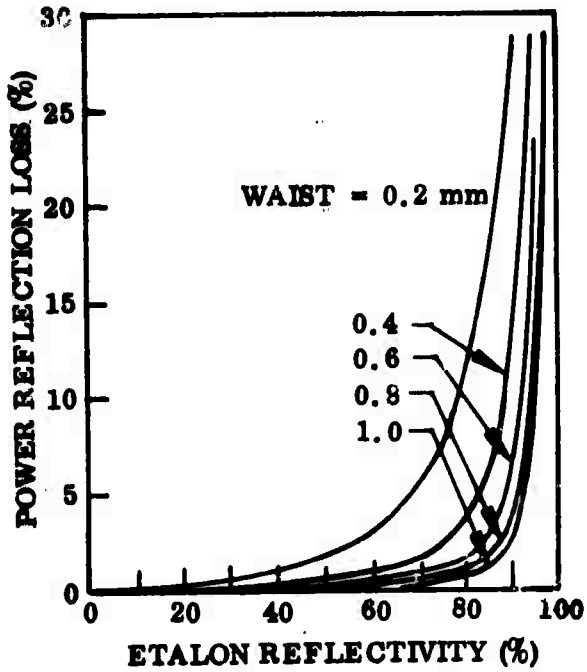

a. Etalon reflectivity. Beam waist. Etalon thickness, 1 cm; refractive index 1.5; tilt angle, 3 arcmin.

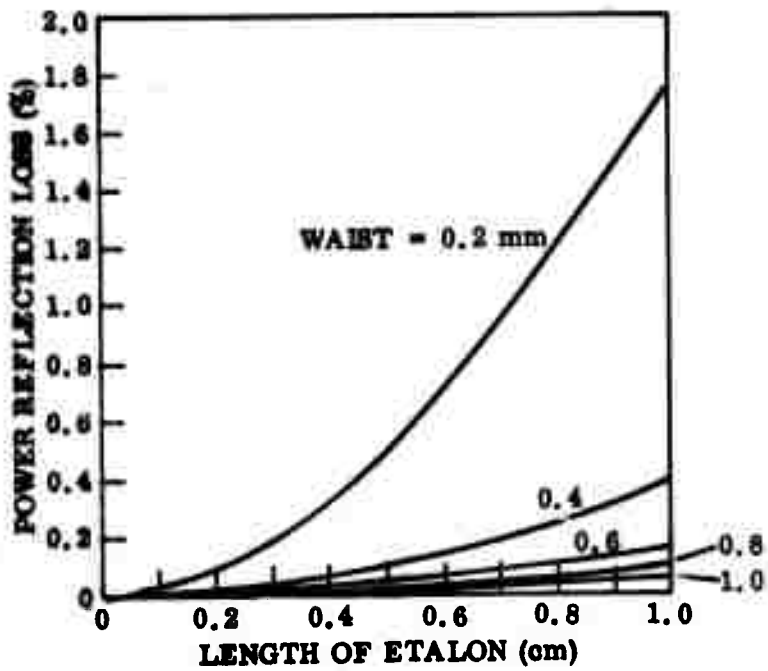

b. Etalon thickness. Beam waist. Etalon reflectivity, 50%; refractive index 1.5; tilt angle, 3 arcmin.

Fig. 2-2 Power Reflection Coefficients or Power Loss of the Tilted Fabry-Perot Etalon Versus Design Parameters for TEM_{00} Mode

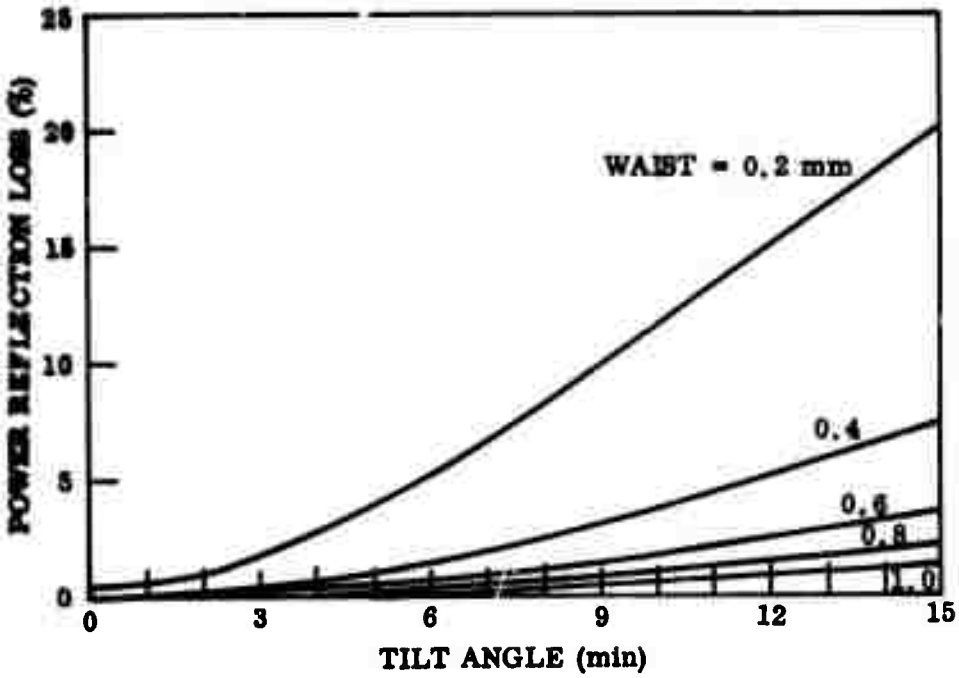

c. Etalon tilt angle. Beam waist. Etalon thickness, 1 cm; etalon reflectivity, 50%; refractive index, 1.5.

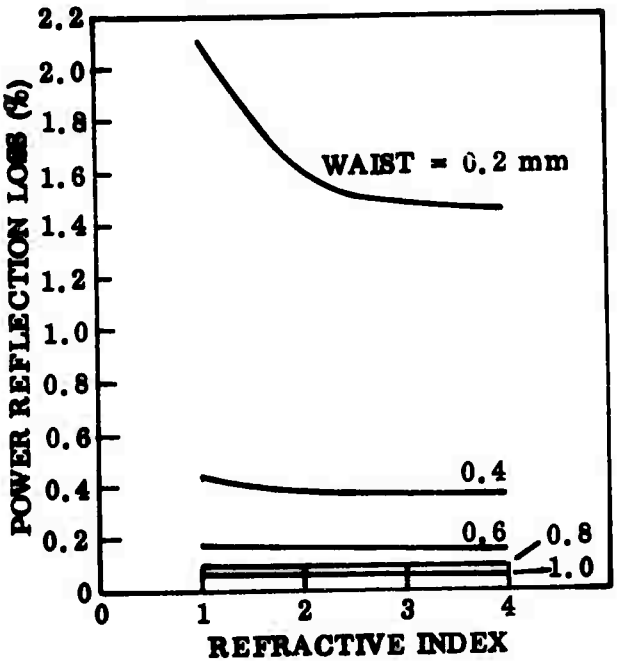

d. Refractive index. Beam waist. Etalon thickness, 1 cm; etalon reflectivity, 50%; tilt angle, 3 arcmin.

Fig. 2-2 (Cont.)

reflectivity, by increasing its refractive index, thus allowing a decrease in the etalon thickness.

Summing up these theoretical results show that intracavity tilted Fabry-Perot etalons can be used for efficient mode selection in low gain (~ 5%) Nd:YAG lasers, and that the insertion losses may be kept small (~ 0.1%) for appropriate cavity designs producing beam waist radii in the etalon of ~ 1 mm. Such low-loss etalons may be designed for lasers of most nominal axial mode separations (300 MHz or greater), and this, together with the relative case in their practical use (discussed in subsection 2.5), makes them very satisfactory as a component part of mode selectors for single-frequency operation. Some experimental verification of these results was given in the Third Quarterly Report.

2.2.3 Insertion Loss of the Metallic Film – Reflector Etalon

Figure 2-3 shows the thin nichrome film – reflector etalon which is used to eliminate possible additional laser oscillations at other frequencies within the gain curve of Nd:YAG. These could occur at frequencies corresponding to other resonances spaced at the free spectral range of the tilted etalon (~ 20 GHz apart for a 5-mm-thick fused quartz etalon). Such additional oscillations will not have a node of the electric field at the nichrome film, when the film-mirror etalon is tuned to the desired frequency, and hence will suffer loss. It is important to deduce the magnitude of such losses as a function of the frequency deviation from resonance of the mirror etalon for various thicknesses of the nichrome film. Such computations also allow the deduction of the loss introduced by such films for the desired mode of operation.

Referring to Fig. 2-4, which represents the transmission or characteristic matrix of a single layer (Refs. 2-2 and 2-3), and its amplitude reflection and transmission coefficients, we may deduce from impedance considerations that

$$r_{n+1} = \frac{[2A - (B + C)]\, r_n + B - C}{2A + B + C - (B + C)\, r_n} \qquad (2.4)$$

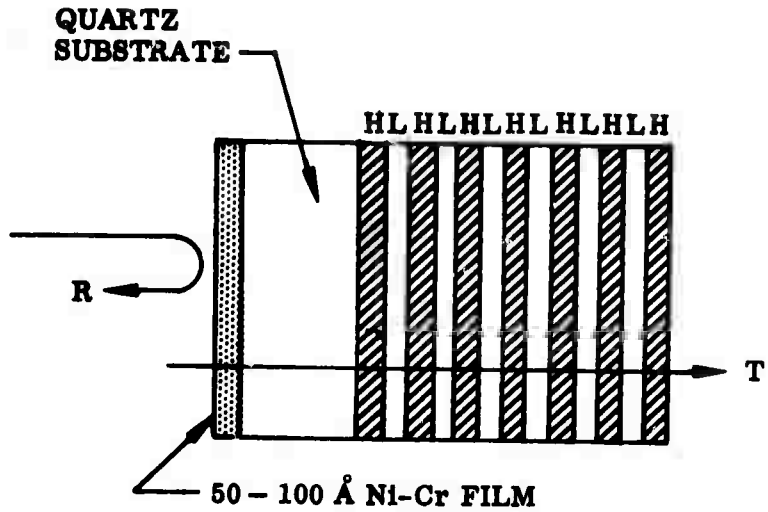

Fig. 2-3 Single Metallic Layer Multilayer Reflector Etalon

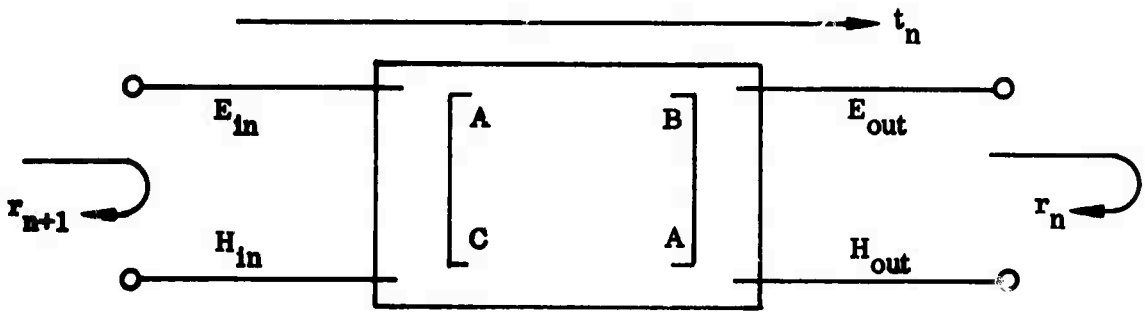

Fig. 2-4 Diagram Showing the Parameters Used for Computations on a Single Layer of the Reflecting System

This is the recurrence relation between the reflection coefficients for the cascaded layers, where the reflection coefficients at the indicated planes are with reference to incidence in free space. Similarly, the transmission coefficient through the layer is given by

$$t_n = \frac{2}{2A + B + C - (B - C)\, r_n} \tag{2.5}$$

and the overall transmission through a number of such layers is then the product of the transmission coefficients of the individual layers.

For a dielectric layer, the transmission matrix is given by

$$\begin{bmatrix} E_{n+1} \\ H_{n+1} \end{bmatrix} = \begin{bmatrix} \cos k_z d & Z_d \sin k_z d \\ \sin k_z d/Z_d & \cos k_z d \end{bmatrix} \begin{bmatrix} E_n \\ H_n \end{bmatrix} \tag{2.6}$$

where

d = the thickness of the layer

k_z = $2\pi n_d/\lambda$

n_d = the refractive index

Z_d = $1/n_d$ = the normalized characteristic impedance of the dielectric for normal incidence

For the metallic film n_d is equal to $n - ik$, where k is the extinction coefficient. The tranmission matrix for this then becomes

$$\begin{bmatrix} E_{n+1} \\ H_{n+1} \end{bmatrix} = \begin{bmatrix} \cosh \gamma \ell_m & Z_m \sinh \gamma \ell_m \\ \sinh \gamma \ell_m / Z_m & \cosh \gamma \ell_m \end{bmatrix} \begin{bmatrix} E_n \\ H_n \end{bmatrix} \tag{2.7}$$

where

$$\gamma = 2\kappa(k+in)/\lambda$$

$$Z_m = 1/(n - ik)$$

$$\ell_m = \text{the thickness of the metallic film}$$

Thus, by inserting these matrix elements for each layer into Eqs. (2.4) and (2.5), the overall reflection and transmission coefficients of the composite nichrome film – multilayer reflector shown in Fig. 2-3 can be determined.

The results of such computations are shown in Fig. 2-5 for a 50 Å nichrome film on one side of a 2-mm-thick quartz etalon with various numbers of quarter wave dielectric layers on the other. The values $n_\ell = 1.35$ and $n_h = 2.30$ (Ref. 2-4) for the low and high refractive indices were used in these computations. Figure 2-6 shows similar results for the 100 Å-thick nichrome film, where the parameters used were $n = 2.40$, and $k = 3.50$. These results show that the frequency response of the nichrome film-mirror etalon becomes sharper as the film thickness increases within limits since the film will eventually become opaque at thicknesses of 500 to 1000 Å at 1.06 μm. The shape of these response curves has been verified experimentally, and the agreement with the theoretical results was very good. It is quite striking that the reflectivity of the 100 Å nichrome film-mirror etalon falls to zero at 20 to 30 GHz from a resonance of the etalon, which result has also been experimentally verified.

The response curves shown in Figs. 2-1a and 2-1b represent the overall response or reflectivity of the composite tilted etalon shown, plus the nichrome film-mirror etalon, and are thus curves of the effective mirror reflectivity for laser oscillation. Laser oscillation will occur at reflectivities such that laser threshold is reached. The mode filters permit threshold to be reached only at the desired single-frequency corresponding to a single axial mode of the laser, even in the presence of spatial hole burning.

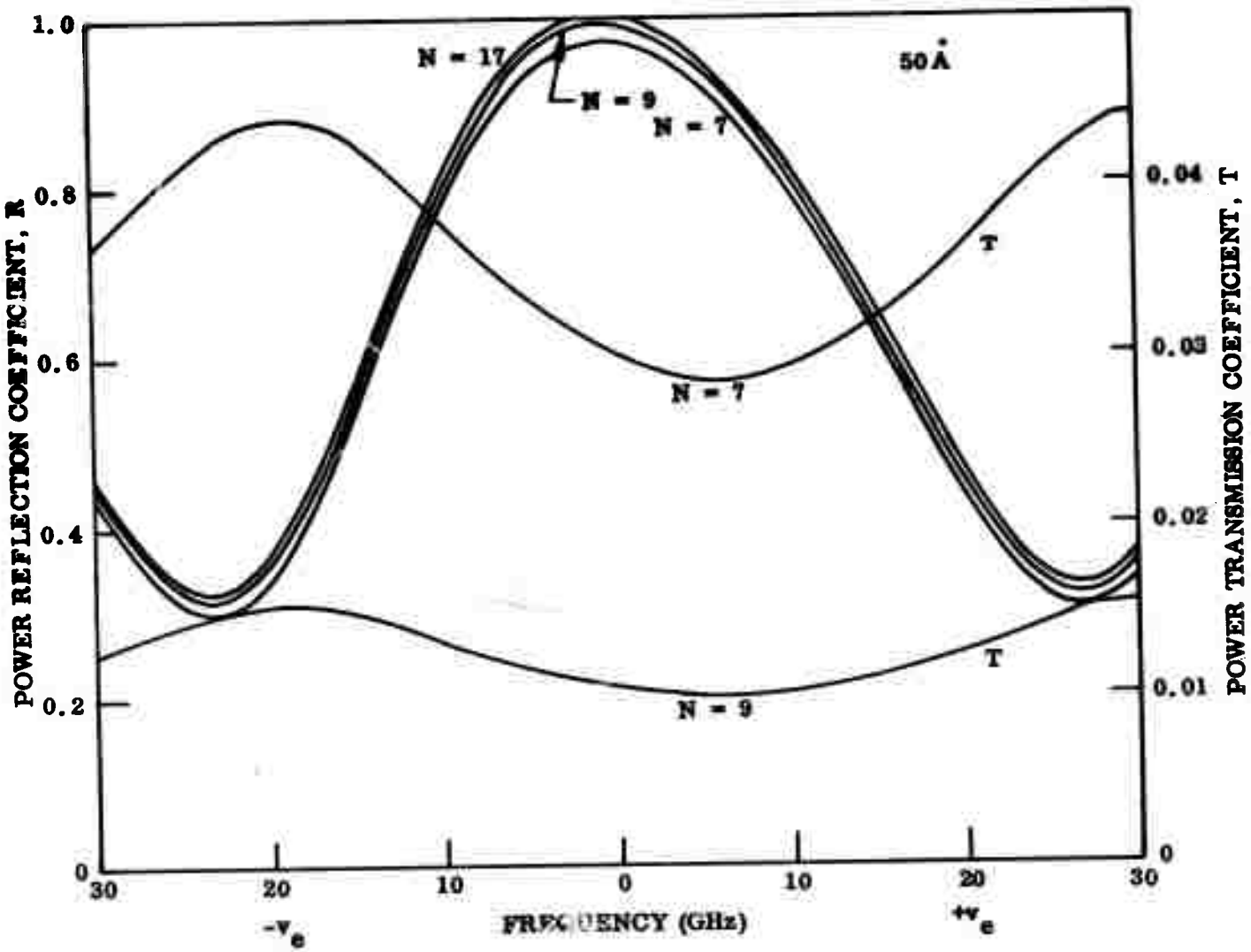

Fig. 2-5 Power Reflection and Transmission Coefficients of a 50-Å-Thick Ni-Cr Film on a 2-mm-Thick Quartz Etalon for Various Numbers N of Quarter-Wave Dielectric Layers on the Reflector Side

LOCKHEED PALO ALTO RESEARCH LABORATORY
LOCKHEED MISSILES & SPACE COMPANY
A GROUP DIVISION OF LOCKHEED AIRCRAFT CORPORATION

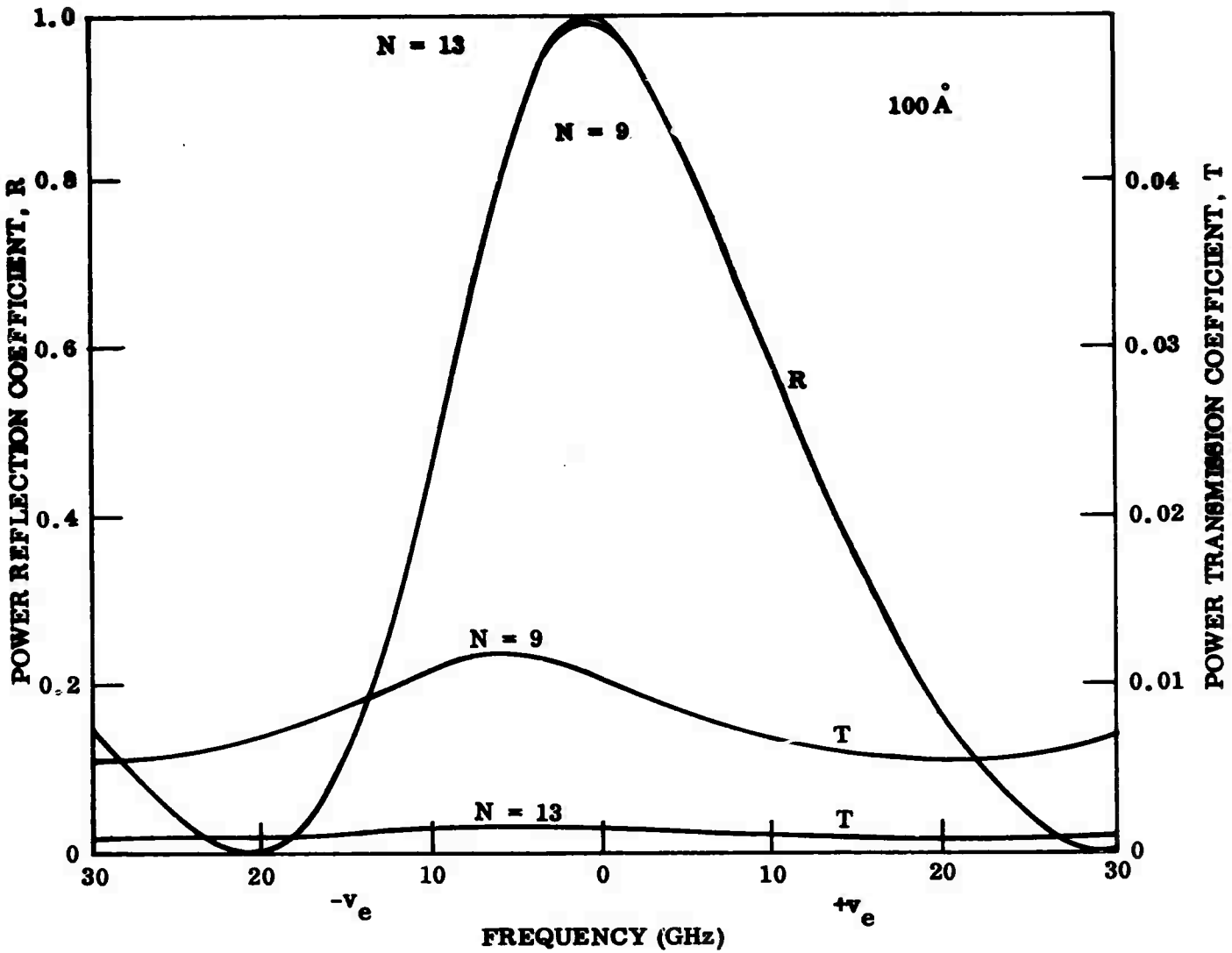

Fig. 2-6 Power Reflection and Transmission Coefficients of a 100-Å-Thick Ni-Cr Film on a 2-mm-Thick Quartz Etalon for 13 and 9 Quarter-Wave Dielectric Layers on the Reflector Side

LOCKHEED PALO ALTO RESEARCH LABORATORY
LOCKHEED MISSILES & SPACE COMPANY
A GROUP DIVISION OF LOCKHEED AIRCRAFT CORPORATION

Table 2-1 gives the values of the peak-power reflection and transmission coefficients R and T of the 50 A nichrome film etalon for various numbers N of quarter-wave dielectric layers. These occur at the indicated frequency deviation Δf from resonance of the quartz substrate.

Table 2-1

POWER REFLECTION AND TRANSMISSION COEFFICIENTS FOR A 50 Å NICHROME FILM AND MULTILAYER REFLECTOR ETALON FOR VARIOUS NUMBERS N OF QUARTER-WAVE DIELECTRIC LAYERS

N	Δf (MHz)	R	T	1 - (R + T)
17	-300	0.99977	0.00015	0.00008
13	-300	0.99865	0.00126	0.00009
9	-300	0.98936	0.01057	0.00009
7	-200	0.96057	0.03025	0.00008

These results show that there is very little insertion loss for a 50 Å nichrome film, and that the laser output may be taken from the film end. Table 2-2 gives similar results for the 100 A nichrome film. The loss in the film is now >0.1%.

Table 2-2

POWER REFLECTION AND TRANSMISSION COEFFICIENTS FOR A 100 Å NICHROME FILM ON A MULTILAYER QUARTZ ETALON

N	Δf (MHz)	R	T	1 - (R + T)
13	-700	0.99759	0.00126	0.00115
9	-700	0.98829	0.01054	0.00117

Thus, for nichrome film thicknesses up to around 100 Å, there is no serious loss in the film when the quartz etalon is tuned to the desired frequency, and the laser output may be taken through the nicrhome film-reflector combination.

In conclusion, the two-component tilted Fabry-Perot etalon-nichrome film mode filter developed by LMSC under the first phase of this contract may be designed for low

overall insertion loss and adequate selectivity. Hence it is very suitable for the efficient, single-frequency operation of low-gain Nd:YAG lasers using standing wave resonant cavities.

2.3 DOUBLE-NICHROME-FILM QUARTZ ETALON MODE FILTER

This type of mode filter for the single-frequency operation of Nd:YAG lasers was discussed in the First Quarterly report. An example is illustrated in Figs. 2-7a and 2-7b, together with curves of the overall reflectivity versus the frequency deviation from resonance. Sharp changes in the impedance presented to the film by the reflector occur as the frequency changes from the resonance condition and the insertion loss increases rapidly for unwanted modes.

Such a mode filter may be made selective enough to suppress axial modes adjacent to the desired mode by adjusting the distance between the double-film etalon and the laser mirror. The computed results for such spacings of 22 mm and 11 mm are shown in Figs. 2-7a and 2-7b. The larger spacing gives an increased sharpness to the numerous responses. These are due to the free spectral range of the etalon – mirror distance and constitute a serious disadvantage for this type of mode selector as compared with the much cleaner response of the tilted Fabry-Perot etalon – nichrome film mode selector shown in Fig. 2-1a. The fall-off in the reflection coefficient at these multiple resonances is due to the double nichrome film etalon and increases with increased nichrome film thickness. However, the insertion losses also increase with film thickness and it is difficult to suppress all possible laser oscillations at these multiple resonances, while still maintaining an adequate selectivity against adjacent axial modes. This is compounded by the obvious difficulty in avoiding coincidences of the resonances of the etalon-mirror distance and of the double nichrome film etalon within the wide gain curve of the Nd:YAG laser transition.

The double-nichrome-film mode selector also requires very good laser stability since both films must be positioned at nodes of the electric field of the desired cavity

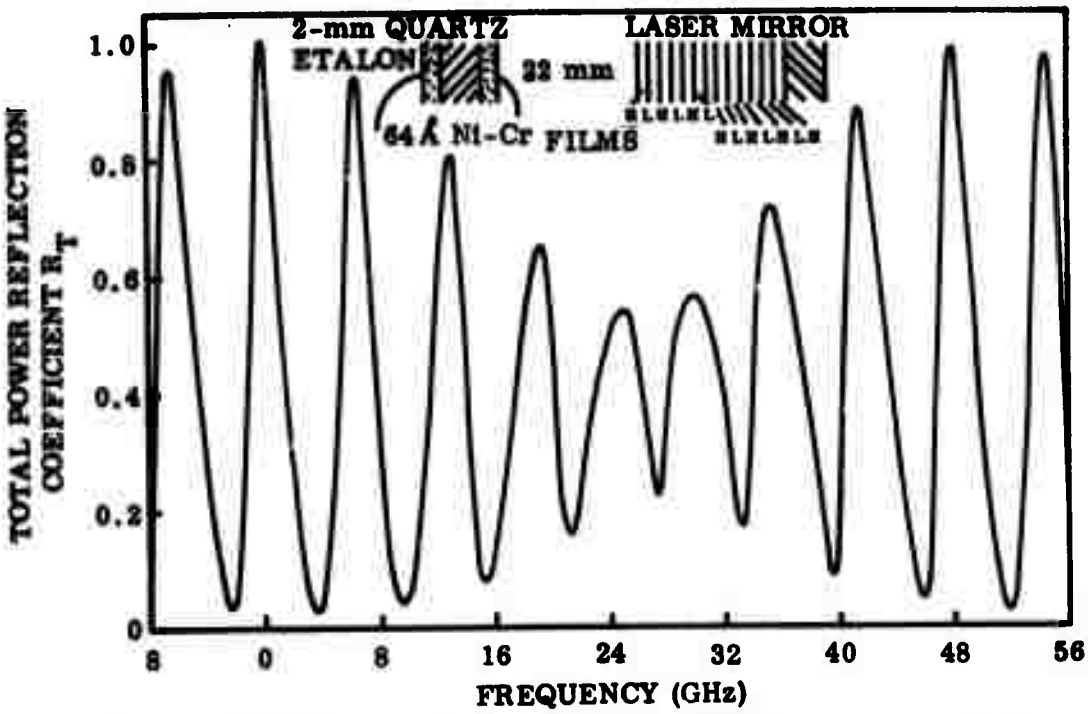

(a) Frequency Response for 64 Å Nichrome Films on a 2-mm Quartz Etalon Spaced at 2.2 cm From the Laser Mirror

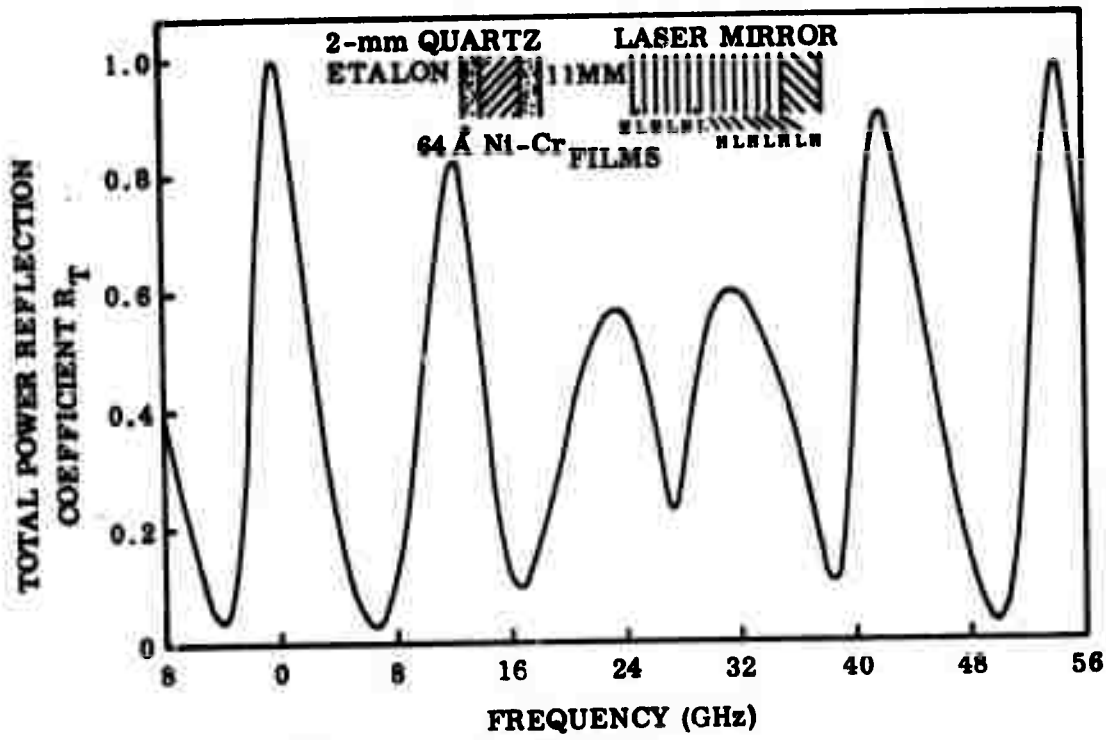

(b) Frequency Response for 64 Å Nichrome Films on a 2-mm Quartz Etalon Spaced at 1.1 cm From the Laser Mirror

Fig. 2-7 Double-Nichrome-Film Quartz Etalon Mode Filter for Single-Frequency Nd:YAG Lasers; Total Power Reflection Coefficient Versus Frequency Deviation From Resonance Condition

mode. This proves to be difficult to maintain in practice as confirmed by our experiments on such mode filters. In insertion loss, this mode selector is similar to that obtained earlier for single-metallic films, and our experiments so far indicate that it is smaller than that of tilted Fabry-Perot etalons of comparable selectivity. However, its application to the single-frequency operation of Nd:YAG lasers has proved difficult because of the positioning constraints involved within the laser cavity. As detailed in the Third Quarterly report, the single-frequency power output obtained with our present double-nichrome film etalon mode filters is lower than that obtained using the tilted Fabry-Perot etalon-nichrome film mode filter. Also, experiments so far have substantiated the practical advantages of transmission-type mode filters as compared with double-nichrome-film devices which require precise positioning within the laser cavity.

2.4 LASER CAVITY DESIGN FOR EFFICIENT SINGLE-FREQUENCY Nd:YAG LASERS

Design curves for efficient single-frequency Nd:YAG lasers were given in the Third Quarterly report, where the steady-state operation of the laser was deduced from the equation (Ref. 2-5)

$$\frac{2\,g_o}{1 + 2SP_c} = L + T \tag{2.8}$$

where

g_o = unsaturated single-pass gain

S = saturation parameter of the particular laser

P_c = circulating power flow in the cavity

L = double-pass cavity loss

T = transmission of the output mirror with the other laser mirror being perfectly reflecting

From Eq. (2.8), we obtain the expressions

$$\left.\begin{aligned} P_c &= \frac{1}{2S}\left(\frac{2g_o - (L+T)}{L+T}\right) \\ P_{out} &= T\,P_c \\ T_{optimum} &= \left(2g_o\,L\right)^{1/2} - L \\ P_{out}^{max} &= \frac{1}{2S}\left(\sqrt{2g_o} - \sqrt{L}\right)^2 \end{aligned}\right\} \qquad (2.9)$$

The importance of the saturation parameter S is evident from these results since both the circulating and output power levels of the laser are proportional to 1/S. This factor increases with the mode volume in the YAG rod and emphasizes the importance of optimum cavity designs and of a knowledge of the value of 1/S for the particular laser design. As detailed in the Semiannual report, the use of a laser output mirror with a continuously variable power transmission coefficient allows a determination of the operating parameters g_o, L, and S of the particular laser from such experimental curves of power output versus mirror transmission.

An optimum laser resonant cavity design must match the cavity mode into the image of the pump lamp in the Nd:YAG rod to give the maximum TEM_{oo} mode volume and thus optimize the efficiency of the laser. This is accomplished at LMSC by using intracavity focusing elements such as a lens or, more appropriately, by shaping the Nd:YAG rod to act as the focusing element. The stability of such resonators and the mode waists and spot sizes throughout the resonator have been deduced using the paraxial ray theory and the ray transfer matrices (Ref. 2-6) of the various optical components.

Consider first the arrangement shown in Fig. 2-8, in which one end of the Nd:YAG laser rod has a radius of curvature R and acts as its own internal lens. Such a design is preferred for an efficient low-gain Nd:YAG laser at the 1-W level of output, where minimal cavity loss is of paramount importance. The overall ray matrix (the ABCD matrix) for this internal optical system is then deduced as

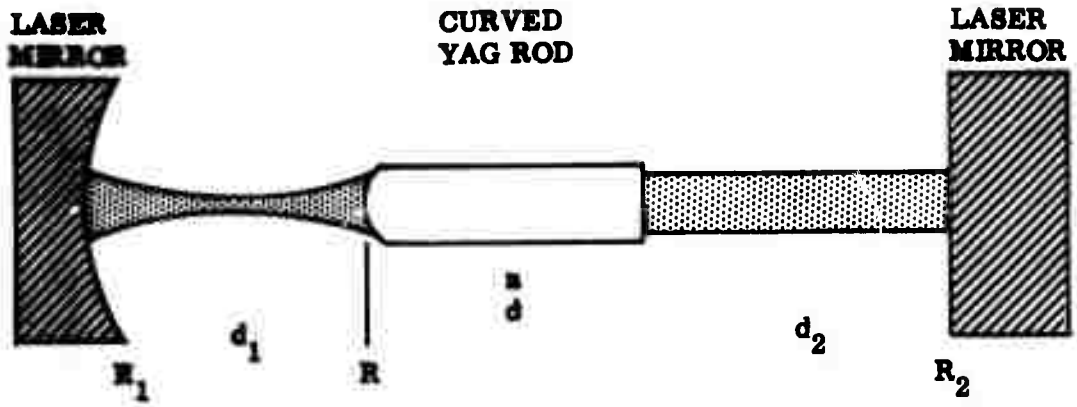

Fig. 2-8 Use of Laser Rod As Intracavity Focusing Lens With Appropriate Curvatures R on Rod

$$\begin{bmatrix} A & B \\ C & D \end{bmatrix} = \begin{bmatrix} 1 - \frac{(d + nd_2)}{nf} & d_1 + d_2 + d/n - \frac{(dd_1 + nd_1d_2)}{ng} \\ -\frac{1}{f} & 1 - d_1/f \end{bmatrix} \tag{2.10}$$

where

$$f = R/(n - 1) \tag{2.11}$$

is the equivalent focal length of the YAG rod, and n is its refractive index. The three basic laser resonator parameters, the Fresnel number and stability factors, may now be written in terms of the above ray matrix. The Fresnel number is given by

$$N = \frac{a_1 a_2}{\lambda B} \tag{2.12}$$

and the stability factors are given by

$$G_1 = \frac{a_1}{a_2}\left(A - \frac{B}{R_1}\right) \quad ; \quad G_2 = \frac{a_2}{a_1}\left(D - \frac{B}{R_2}\right) \tag{2.13}$$

where $2a_1$ and $2a_2$ are the diameters of the respective laser mirrors (Ref. 2-7). For a stable, low-loss resonator, we must have

$$0 \leq G_1 G_2 \leq 1 \tag{2.14}$$

These equations, therefore, allow stable laser cavity configurations to be deduced.

The beam radii, or spot sizes, w_1 and w_2 on the respective mirrors of the resonator with the internal focusing element, are then given by (Ref. 2-7)

$$w_1 w_2 = \frac{\lambda d_o}{\pi}\left(1 - G_1 G_2\right)^{-1/2} \tag{2.15}$$

and

$$\frac{w_1}{w_2} = \frac{a_1}{a_2}\left(\frac{G_2}{G_1}\right)^{1/2} \tag{2.16}$$

where the distance d_o in Eq. (2.15) is given by the matrix element B in Eq. (2.10), and represents an effective distance between the mirrors as modified by the internal focusing element. For cases where d_o is very small, the ray angles of interest become rather large and such cases are excluded. The formulae (Ref. 2-6)

$$w^2(z) = w_0^2\left[1 + \left(\frac{\lambda z}{\pi w_0^2}\right)^2\right] \tag{2.17}$$

and

$$R(z) = z\left[1 + \left(\frac{\pi w_0^2}{\lambda z}\right)^2\right] \tag{2.18}$$

where w_0 is the beam waist radius, may now be used, together with the consequential relation

$$\frac{\lambda z}{\pi w_0^2} = \frac{\pi w^2(z)}{\lambda R(z)} \tag{2.19}$$

to determine the beam radius $w(z)$ and the radius of curvature $R(z)$ of the wave front throughout the laser cavity. Optimum designs of the laser cavity for given Nd:YAG rod dimensions and lamp pumping geometries have thus been established.

Figure 2-9 shows the results obtained for the beam spot radius at the YAG rod versus the curved mirror-rod distance d_1 for various mirror radii R_1 and focal lengths of the laser rod. The Gaussian beam spot radius at the YAG rod and the beam waist are relatively independent of the distance d_2 from the plane mirror near which the mode filters for single frequency operation are situated. These curves show that an adequate spot radius w_R at the laser rod is obtainable in such cavity designs. For example, a mirror radius R_1 of 10 cm and a radius R on the rod of 25 cm will produce a spot radius at the rod of 0.8 mm, while a radius R_1 of 5 cm will give a spot radius of 1.1 mm. These large spot radii provide adequate TEM_{oo} mode volume in the rod, and thus reduce the saturation parameter S and make more effective use of the excited Nd ions. Measurements made on our operating lasers are in good agreement with these theoretical curves and demonstrate the validity of the ray transfer method of optimizing cavity design.

Variants of the cavity design shown in Fig. 2-8 are possible. Thus, the mirror R_1 may be made convex so as to provide a virtual waist with the same adequate mode volume in the laser rod and with a shorter overall cavity design.

As another alternative, one might use the arrangement shown in Fig. 2-10, which has an internal lens of focal length f placed at distances d_1 and d_2 from the respective mirrors. The internal optical system then comprises the spacing d_1, the lens of

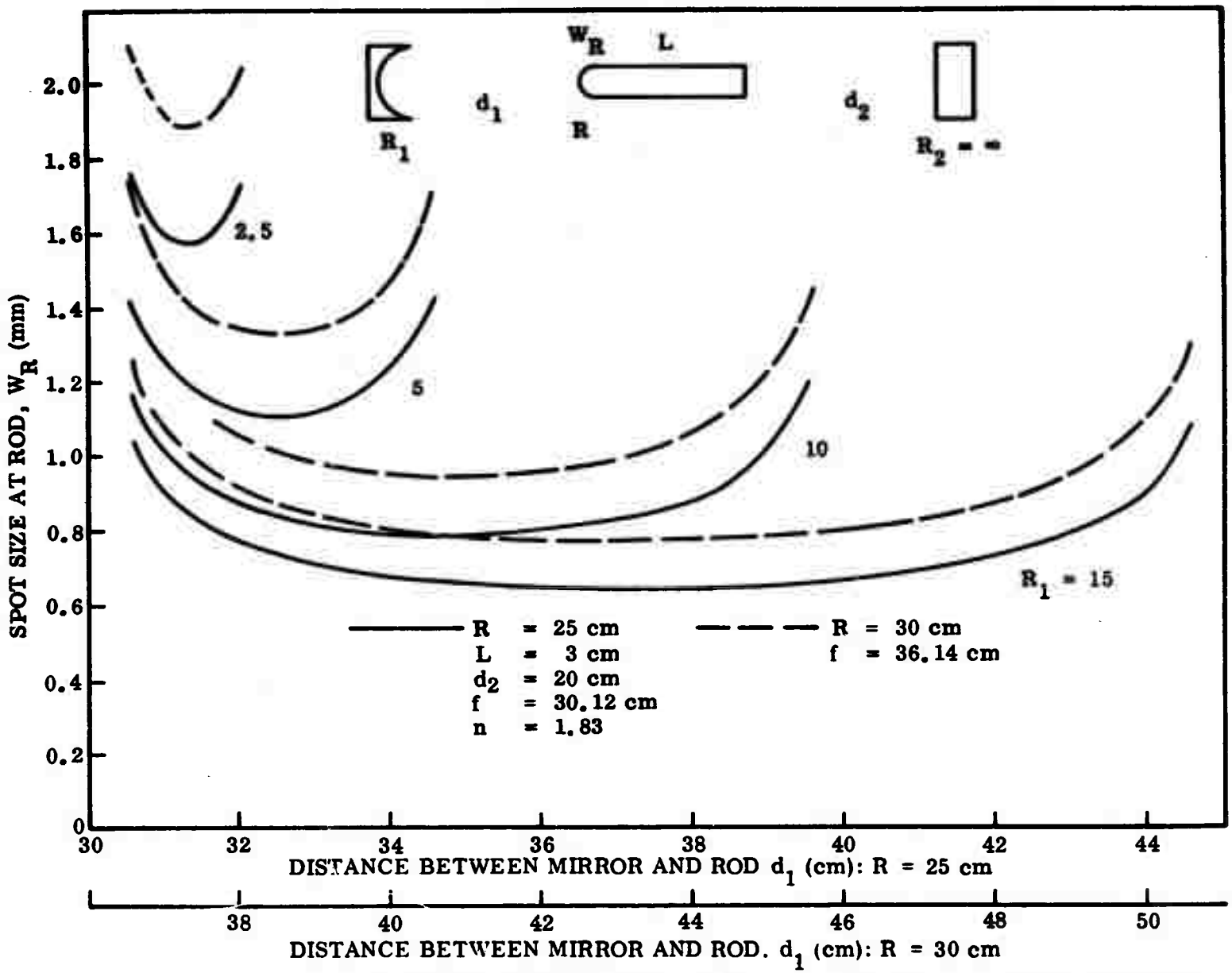

Fig. 2-9 Beam Spot Radius at the YAG Rod Versus Curved Mirror – Rod Distance d_1 for Various Mirror Radii R_1 and Focal Lengths of the Laser Rod

LOCKHEED PALO ALTO RESEARCH LABORATORY
LOCKHEED MISSILES & SPACE COMPANY
A GROUP DIVISION OF LOCKHEED AIRCRAFT CORPORATION

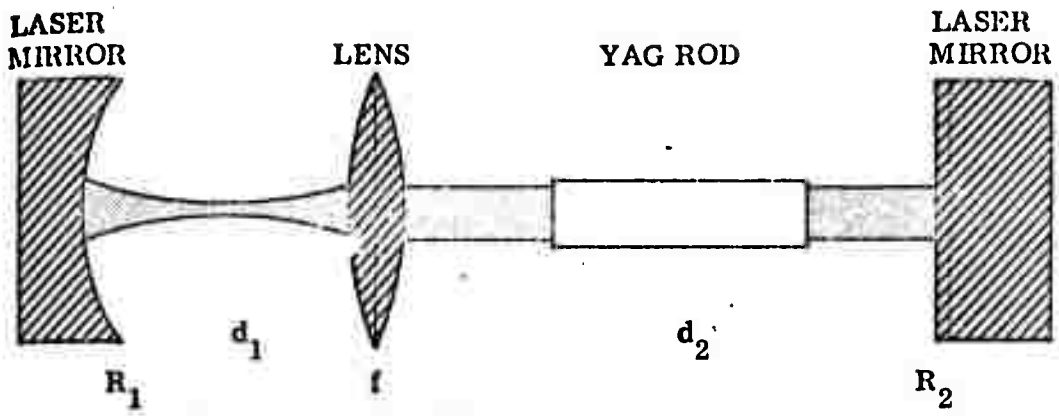

Fig. 2-10 Increasing the TEM_{00} Mode Volume in the Laser Rod With an Intracavity Focusing Lens

focal length f, and the spacing d_2, for which the paraxial ray transfer matrix is given by

$$\begin{bmatrix} A & B \\ C & D \end{bmatrix} = \begin{bmatrix} 1 - d_2/f & d_1 + d_2 - d_1 d_2/f \\ -1/f & 1 - d_1/f \end{bmatrix} \tag{2.20}$$

The expressions for the complete TEM_{00} mode parameters within the laser cavity are deduced as before for appropriate values of f and d_1. From these results, optimum cavity designs have been determined which adequately fill the laser rod with the TEM_{00} mode. The mode design must be made compatible with the pumping geometry in order to obtain the best efficiency. Since it avoids introducing additional components into the laser cavity, the self-focusing laser rod geometry is preferred. This arrangement may also be designed to avoid difficulties due to the thermal self-focusing of the laser rod by making the geometrical lens affect the dominant one.

2.5 EXPERIMENTAL RESULTS

2.5.1 Laser Design

The Nd:YAG laser developed at LMSC during the initial contract phase uses a 30-mm-long by 5-mm-diameter rod pumped by a 30-mm-long by 5-mm-diameter filament

tungsten-iodine quartz lamp in a 8-in.-diameter spherical, gold-coated, pumping cavity. This spherical cavity geometry approaches the maximum possible coupling or pump efficiency for short laser rods and lamps. It represents a suitable standard of pumping arrangement for the comparison of other pump sources such as elliptical cylinders or close-coupled methods which are more suitable for longer lamps and rods. By increasing the TEM_{oo} mode volume in the rod as detailed in subsection 2.4, a level of single-frequency output of 1 W should be obtained in this Nd:YAG laser at the 1-kW pump power level using the tungsten-iodine lamp, and 0.8-W single-frequency output has already been achieved.

In conjunction with this effort work has proceeded on improving the overall efficiency of the single-frequency operation of the Nd:YAG laser by incorporating the new potassium-rubidium lamps into the laser design. Under the proper conditions of pressure and temperature, the potassium resonance lines radiate efficiently at the infrared absorption lines of Nd^{3+} in YAG. Results show that an approximate threefold improvement in pumping efficiency over the tungsten filament lamp is possible (Ref. 2-8).

The first laser cavity arrangement used is shown schematically in Fig. 2-11, where the distance between the reflectors is some 40 cm giving an axial-mode spacing of 360 MHz. The initial work on the development and testing of the mode filters was done in the laser cavity shown. This cavity had a TEM_{oo} mode radius of about 0.6 mm. After the mode filters were developed and the fabrication techniques established, laser mirrors with radii of 10 cm and finally 5 cm were used (in conjunction with a curvature on the rod) instead of the 4-m-radius mirror in order to increase the TEM_{oo} mode volume in the laser rod and thus to increase the single-frequency power output of the laser. Mechanical stability was obtained by mounting the laser reflectors in substantial end plates and using vibration damped Invar rods as spacers. The laser rod holder was designed so that the cooling water is directed to the rod through three ports at right angles to each other. This was found to reduce substantially the mechanical vibrations encountered in our earlier one-port cooling jacket. An iris was used to obtain TEM_{oo} mode operation, although the mode selectors also provided some rejection of off-axes modes.

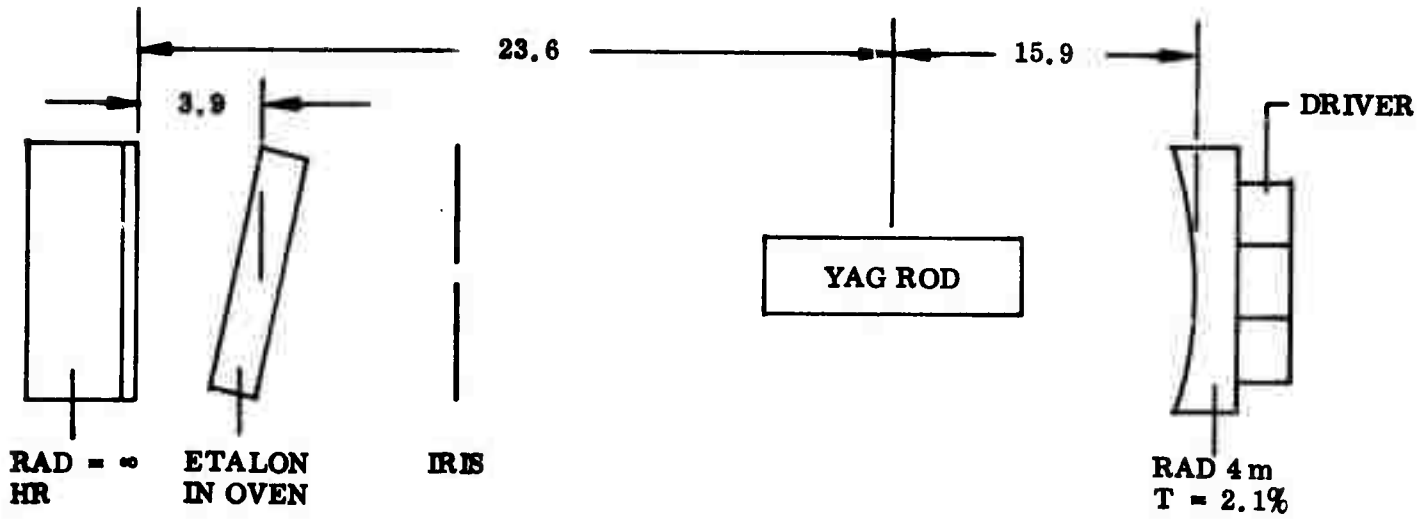

Fig. 2-11 Nd:YAG Laser Configuration Used in Mode Selector Experiments

2.5.2 Tilted Fabry-Perot Etalon and Metallic-Film Mode Selector Experiments

The performance of a number of mode filters for the single-frequency operation of our Nd:YAG laser has been evaluated and optimum designs have been established. Intracavity 5-mm-thick fused-quartz etalons, both uncoated and with 45 and 60% reflective coating, and an 11-mm-thick fused-quartz etalon with 35% reflective coatings were investigated. Single-metallic-film-reflector mode selectors were also fabricated and their performance ascertained. This type of selector was then used in conjunction with the 11-mm-thick fused-quartz etalon to suppress laser oscillations at the next free spectral range (9.35 GHz) of this intracavity etalon as discussed in subsection 2.2. In most of these experiments, the laser was operated at a 1-kW pump power level at which the unsaturated single-pass gain of our laser is about 5 percent.

Figure 2-12a shows a typical frequency spectrum of the laser output without any mode filter; the spectrum obtained with a confocal scanning interferometer of 8 GHz free spectral range. Since the free-running Nd:YAG laser has multimode oscillation widths some 30 GHz wide, the spectrum displayed consists of competing oscillations on a number of cavity modes. Furthermore, the observed spectrum is not stationary but shows continuous mode hopping with accompanying fluctuations in the laser output. A similar spectrum was obtained with the 5-mm-thick fused quartz etalon inserted normal to the laser beam.

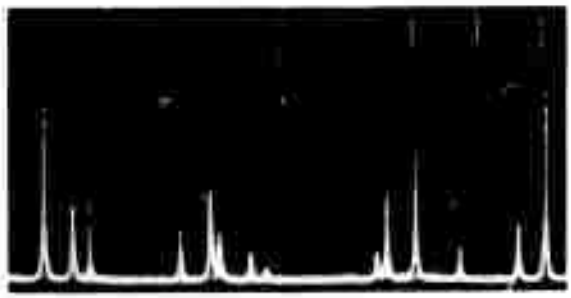

(a) Typical frequency spectrum of the free-running laser as displayed by a scanning interferometer with a free spectral range of 8 GHz. Frequency scale, 1 GHz/cm

Reproduced from best available copy.

(b) Same as (a) but with a 5-mm-thick quartz etalon of 60% reflectivity in the laser cavity. Etalon tilt angle, 3 arcmin. Output power, 200 mW

(c) Same as (a) but with a 5-mm-thick uncoated quartz etalon inside the laser cavity. Tilt angle now 2 arcmin. Output power, 430 mW

Fig. 2-12 Output Frequency Spectra of Operating Nd:YAG Laser

As the etalon was tilted, the spectrum became increasingly cleaner. With such a 60-% reflective coated etalon, three axial modes were observed at a tilt angle of 1.5 arcmin, two modes at 2 arcmin tilt, and finally, at a tilt angle of 3 arcmin, a single stable axial-mode oscillation with an output power of 0.2 W was obtained as shown in Fig. 2.12b. However, the free spectral range of the 5-mm-thick quartz etalon (20.5 GHz) was not sufficient to completely eliminate oscillation at its next resonance. This is apparent in Fig. 2.12b, although the undesired oscillation is quite weak. The present laser gave a multimode TEM_{oo} output of 0.55 W.

Experiments were performed using a uncoated 5-mm-thick quartz etalon which had its reflectivity determined by the Fresnel reflection at the dielectric-air interface. As expected, the reflectivity was too low to reduce the laser oscillations to a single frequency, although when the etalon was tilted by 1 arcmin, the spectrum reduced to 3 adjacent axial modes, as shown in Fig. 2-12c. No mode hopping was observed and the output was extremely quiet and stable.

As was observed with all the etalons, the 11-mm-thick etalon with 35% reflective coatings produced no change in laser threshold and output then inserted normal to the laser beam. In contrast to the 5-mm-thick etalons it did, however, effect some mode selection even at normal incidence. The reason for this is probably its greater selectivity, as deduced from Eq. (2.1); thus, some decoupling from the laser reflector occurs with this etalon even at normal incidence. A typical spectrum observed for normal incidence is shown in Fig. 2-13a. Three adjacent modes are oscillating, and the spatial inhomogeneity of resultant population inversion is sufficiently small in this case so that no oscillations occur at the next resonance of the etalon, which is 9.35 GHz away.

When the etalon is tilted by 2.6 arcmin, the oscillations on adjacent axial modes are suppressed, and the new frequency spectrum is shown in Fig. 2-13b. There is now sufficient residual gain at some portions of the rod to allow two more oscillations at 9.35 GHz away from the main one. The position of their display arises from the overlapping orders of the scanning interferometer. When a 64-Å-thick nichrome

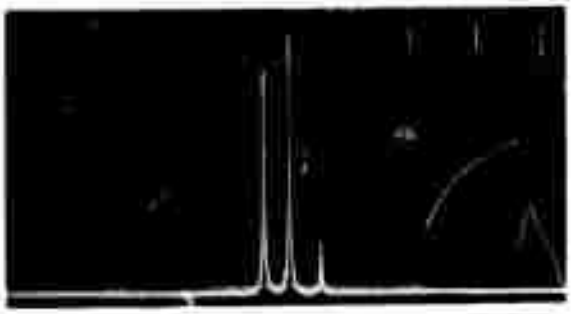

(a) Fabry-Perot quartz etalon 11-mm-thick with 35% reflectivity inside the laser cavity. Normal incidence. Output power, 550 mW

Reproduced from best available copy.

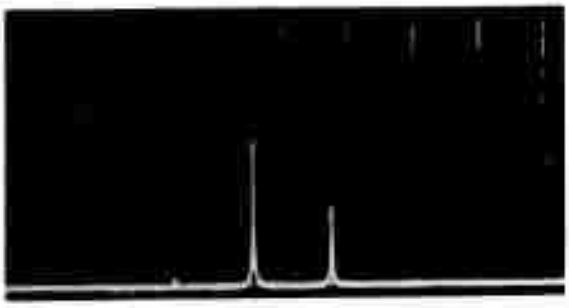

(b) Same as (a) but with etalon tilted 2.6 min of arc. The satellite modes are displayed from overlapping orders of the scanning interferometer and occur at 9.35 GHz from the main mode. Output power, 300 mW

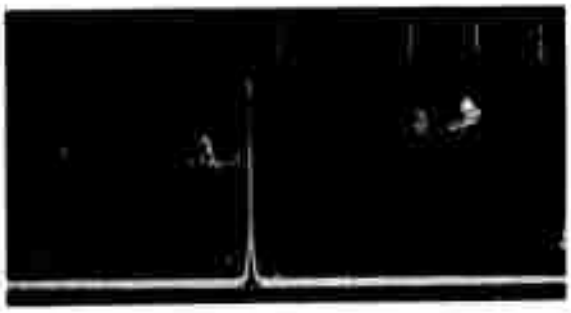

(c) Single-frequency, operation with tilted 11-mm-thick etalon and metal film reflector combination. Frequency scale as before. Output power, 200 mW

Fig. 2-13 Output Frequency Spectra of Operating Nd:YAG Laser

film-reflector etalon (5 mm thick) was used in conjunction with the 11-mm-thick Fabry-Perot etalon, these undesired oscillations were completely eliminated and a stable single-frequency Nd:YAG laser output was obtained, as shown in Fig. 2-13c.

These initial investigations were mainly concerned with the design and fabrication of Fabry-Perot etalons and with developing the thin film techniques required for the depositions of 50 to 100 Å thick nichrome films onto fused quartz etalons. The cavity configuration shown in Fig. 2-11 with its 4-m-radius mirror gave a beam spot radius at the YAG rod of only 0.6 mm. Such a TEM_{00} mode volume uses only a small portion of the pumped rod resulting in low efficiency and low TEM_{00} output power (0.55 to 0.6 W) in this case. Thus, the efficiency and single-frequency power outputs were increased in the next phase by increasing the mode volume in the rod.

The cavity configuration was modified to use a Nd:YAG laser rod with a fairly short radius of curvature (25 to 30 cm) ground in one end in conjunction with short radius mirrors (5 to 10 cm) instead of the 4-m-radius mirror. In agreement with the theory in subsection 2.4, this increased the TEM_{00} mode volume in the rod and TEM_{00} power outputs of 1.5 W were obtained in one such laser cavity with a 1-kW tungsten lamp. This cavity consisted of a laser rod with a 30-cm radius on one end and a 10-cm-radius laser reflector.

In another cavity configuration using a radius of 25 cm on one end of the rod in conjunction with a 10-cm-radius reflector, we have obtained 1.1 W TEM_{00} output power with a 1 kW tungsten lamp. The calculated TEM_{00} mode radius at the rod for this configuration is 0.75 mm, and hence the mode still uses only a small portion of the pumped rod. With this arrangement we have obtained a stable, single-frequency TEM_{00} output by 0.5 W at the 1-kW pump level.

We are presently investigating the use of a 5-cm-radius reflector which would increase the mode radius at the rod to about 1.05 cm. This should increase the TEM_{00} output power to 2 W and would then give 1 W of single-frequency output at 1.064 μ. In initial experiments with a 5-cm-radius reflector and a 25-cm-radius on one end of the laser

rod, we have obtained TEM_{00} output power of 2 to 2.8 W in agreement with these predictions. However, because of the increased sensitivity of such short radius mirror cavities to perturbations, as can be seen from the curves in Fig. 2-9, some difficulty has been experienced in producing stable single frequency of oscillation with present mode selection etalons in such a cavity.

A single-frequency output power of about 0.8 W has been observed, and further work to eliminate the instability is underway. This may require a more flexible cavity design and larger radii of curvature on the laser rod. The radii would then allow a larger radius mirror to be used for the same mode volume in the rod, and also reduce possible aberration effects in the laser rod because of the tilting of mode selection Fabry-Perot etalon. Also, it may be beneficial to reduce the reflectivity of the etalon, using a longer etalon to obtain the required selectivity as discussed in subsection 2.1.

2.5.3 Double Metallic Film Mode Selector

Some of the experimental results obtained with this mode filter were given in the Third Quarterly progress report. In general, these substantiate the conclusions reached in subsection 2.3. Both single-metallic-film mode selectors and the double-metallic-film etalon were investigated. A 64-Å nichrome film was deposited on one side of a 5-mm-thick quartz etalon and a high-reflectivity coating on the other. Stable laser operation was achieved with this, but the selectivity was insufficient for single-frequency operation in our laser. A frequency spectrum similar to that shown in Fig. 2-12c was obtained for the uncoated 5-mm-thick-intracavity etalon.

A double-metallic-film mode selector with 42-Å-thick nichrome films on a 5-mm-thick quartz etalon was also tested in the Nd:YAG laser. The closest spacing between the end reflector and the metal film possible in our present laser was 4 cm, and this together with the 42 Å film thickness did not provide sufficient selectivity at other free spectral ranges for this spacing for single-frequency operation at the full 1-kW level of pump power. The experiments, however, did verify the main theoretical

conclusions reached in subsection 2.3. These may be summarized as follows:

(1) The mode filter can provide excellent discrimination against adjacent axial modes.

(2) It is difficult to suppress laser oscillations at the other numerous resonances corresponding to the etalon-mirror distance.

(3) The practical use of the double-metallic-film mode filter is difficult be-case of the positioning constraints involved and the high degree of laser stability required for stable operation.

(4) Indications are that its insertion loss is smaller than that of tilted Fabry-Perot etalons of comparable selectivity.

Some additional experimental results were given in the Third Quarterly report. The conclusion reached in the experimental investigation is that the tilted Fabry-Perot etalon and metal film-mirror etalon combination is a good practical two-component mode filter for the single-frequency operation of Nd:YAG lasers for all nominal values of unsaturated single-pass gains. The laser output may be taken through the metallic film-mirror etalon without any additional loss.

2.6 COMPARISON OF KNOWN AND POTENTIAL SINGLE-FREQUENCY TECHNIQUES

2.6.1 LMSC Two-Component Tilted Fabry-Perot Etalon and Metallic Film Mode Filter

The properties which make this filter practical for the single-frequency operation of Nd:YAG or Nd:YALO lasers may be enumerated as follows:

(1) True single-frequency operation is possible for all nominal levels of laser gain, thus eliminating the possibility of amplitude and phase fluctuations due to mode competition.

(2) The two-component mode filter is suitable for all cavity designs, and in particular for the longer cavities required in some applications.

(3) Its insertion loss as measured by threshold measurements is low (~ 0.1%), which allows efficient laser operation.

(4) Because of its low insertion loss, and despite the usual spatial hole burning in the inverted population, 1 W of single-frequency output at 1.06 μm from a Nd:YAG laser is feasible with a nominal unsaturated single-pass gain of only 5%. This gain should be achievable with a potassium-rubidium lamp pump source.

(5) The laser frequency is controlled by the transmission etalon and remains stable when feed-back controls stabilizing the cavity length are applied. There is no frequency hopping or erratic changes in the frequency of the laser.

(6) No external geometrical constraints are imposed in the laser with this mode filter as would be the case with any mode filter devised using, say, external magnetic fields.

(7) This two-component mode filter can be engineered into a rugged, stable design using low-expansion materials such as CER-VIT and represents a very practical solution for a space-qualifiable single-frequency Nd:YAG laser.

(8) These conclusions are well substantiated by the LMSC experimental work performed under this contract. A single-frequency output of 0.8 W at 1.06 μm has already been obtained with a 1-kW tungsten lamp. Further experiments indicate that this can be increased to the 1-W level of single-frequency output.

2.6.2 Uniform Cavity-Field Intensity Longitudinal Mode Technique

This technique (Ref. 2-9) is illustrated in Fig. 2-14 and uses a method (Ref. 2-10) for avoiding spatial hole burning by the potential elimination of the axial variation of laser light intensity along the laser rod. A spatially homogeneous population inversion can be created by placing the rod between two quarter-wave plates suitably oriented and placing a Brewster's angle plate in front of one end mirror. The quarter-wave plates transform linearly polarized light at the mirrors into circularly polarized light beams

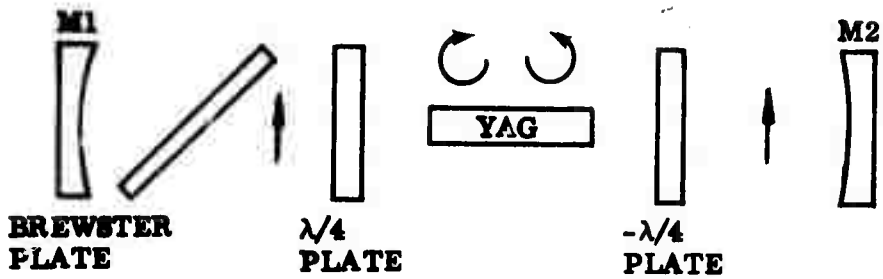

Fig. 2-14 Mode Selection Using Uniform Cavity-Field Intensity in the Rod

inside the rod. The characteristics of this mode filter may be briefly stated as follows:

(1) There are six reflecting surfaces inside the cavity which require AR coatings. With present AR coating techniques, single-pass cavity losses as high as 1.5% are possible. Such high insertion losses are prohibitive in low-gain Nd:YAG lasers.

(2) True single-frequency operation was not attained with this device. "Satellite modes" leading to frequency and amplitude instabilities were always present.

(3) For pump powers in excess of 1 kW from a tungsten lamp, the maximum power output attained was 0.5 W under nearly unstable cavity conditions which gave the larger mode volume in the laser rod.

(4) There is no definite element governing the laser frequency in this system and mode hopping, and other spurious frequency changes are prone to occur.

2.6.3 Spatial Homogeneous Single-Frequency Operation by Translation of the Nd:YAG Rod

The spatial modulation of the rod inversion can also be smoothed out by translating the excited ions relative to the cavity standing wave. This can be done by moving the

rod relative to the mirrors (Ref. 2-11). Comments on this method are as follows:

(1) Practically, this would be an extremely difficult method because of alignment problems and also because of the velocity of the rod which must be reversed at some stage in the process.

(2) Such movements within the cavity and consequent changes in impedances lead to cavity instabilities and mode changing, and there is again no dominant frequency-controlling element.

(3) A single-frequency power output of 0.065 W was obtained, but no indication of the potential of the method for higher output powers was given.

2.6.4 Single-Frequency Operation by the Electrooptic Elimination of Spatial Hole Burning

In this method, the rod is placed between two intracavity electrooptical phase modulators as shown in Fig. 2-15 (Ref. 2-12).

Comments relating to this method are as follows:

(1) The technique is excessively complicated requiring two high-quality lithium niobate intracavity phase modulators and associated circuitry.

(2) Intracavity losses are again serious and offset any advantages regarding the efficient use of the inverted population.

(3) To avoid fluctuations due to multiple-reflection effects, the modulator crystals had to be tilted at 12 deg, which introduced even more serious insertion losses. At this juncture, the output power was reduced to 0.023 W.

Fig. 2-15 Arrangement Used for Demonstrating Electrooptic Elimination of Spatial Hole Burning. Two lithium niobate crystals with their c-axes as shown are modulating the phase of the standing wave pattern in the rod

2.6.5 Other Potential Methods for Single-Frequency Operation

The LMSC two-component mode filter devised for the single-frequency operation of Nd:YAG or Nd:YALO lasers thus represents a good practical solution for a low-gain, single-frequency 1.06 μm laser. Despite some deficiencies in the efficient use of the available inverted population due to the standing wave electric field within the laser rod, this technique is capable of providing 1 W of single-frequency output at 1.06 μm by optimization of the laser design.

However, it would be advantageous to eliminate the spatial hole burning due to the standing wave cavity field, particularly from the viewpoint of overall efficiency. Various types of Zeeman lasers have been considered with this in mind, but no satisfactory solution has been reported which would use a straight Zeeman splitting of the laser transition. This is primarily due to the large linewidths involved (~ 150 GHz). The elimination of spatial hole burning in a standing wave laser with such technique appears difficult.

One is therefore led to the consideration of a ring-type laser in which one of the two oppositely traveling waves is attenuated to allow only a single traveling wave mode of oscillation to build up. Such an oscillation would use all the inverted population within the pumped rod giving no spatial hole burning and hence eliminate directly the possibility of any other oscillation occurring within the gain curve of the laser. This idea is very attractive and Fig. 2-16 shows one way in which such a single traveling wave oscillation may be obtained. Here we have a ring-type laser with a Faraday rotation, a half-wave plate and a polarizer inserted. The direction of rotation of the polarization of the Faraday rotator is nonreciprocal; it depends only on the direction of the applied magnetic field and not on the direction of travel of the laser beam. The direction of rotation of the polaization due to the half-wave plate changes with the direction of travel of the laser beam. Thus, conditions may be arranged so that the desired polarization as fixed by the polarizer suffers no rotation on passing through the Faraday rotator and the half-wave plate, while the oppositely traveling wave has its polarization rotated by an angle 2 θ_f, where θ_f is the rotation produced by the Faraday rotator.

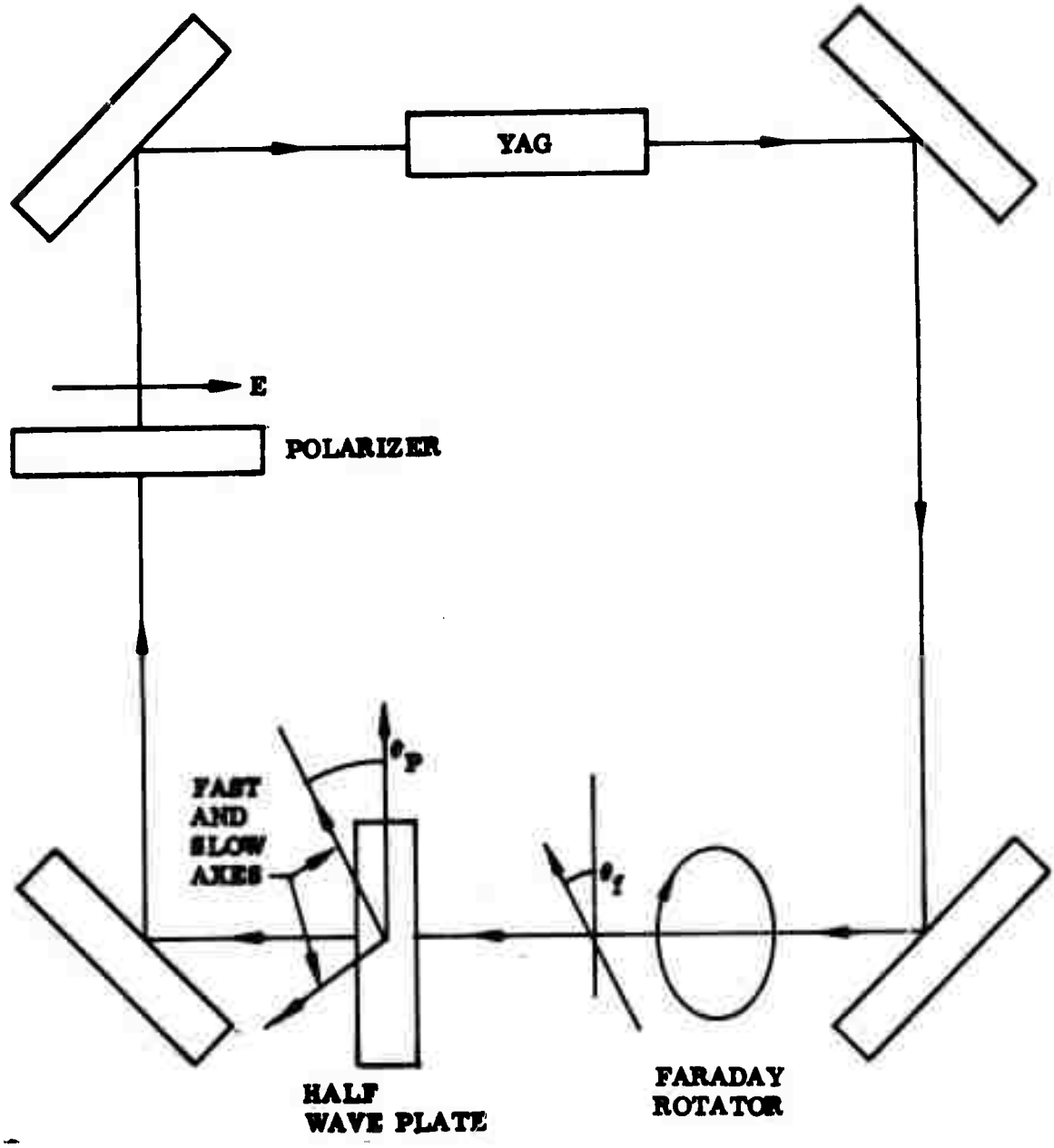

Fig. 2-16 Single Traveling Wave Ring Type Laser for Single-Frequency Operation of the Nd:YAG Laser Without Spatial Hole-Burning

The eigenstates of polarization of the system and the eigenvalues are readily determined. We find that if θ_p is the angle made with the vertical by the fast axis of the half-wave plate, then when the Faraday rotation θ_f is equal to $2\,\theta_p$, one traveling wave suffers zero attenuation while the oppositely traveling wave has a power attenuation of $\cos^2(2\theta_f)$. It would appear that adequate Faraday rotators of low loss can be devised to give a sufficient degree of rotation so as to allow a single-traveling-wave oscillation to build up. The use of a single-traveling-wave laser thus appears quite possible. Its insertion loss may be greater than that of the two-component intracavity mode filter in a standing wave laser depending on available materials and components. However, the more efficient use of the total population inversion in the laser rod could offset this possible disadvantage. Also its implementation and operation could be less critical than the tilted Fabry-Perot etalon – metallic film mode filter.

Section 3
WIDE-BANDWIDTH OPTICAL MODULATOR

In our efforts to improve the ultrawide-bandwidth optical modulator previously developed, work has proceeded on the theoretical analysis of the interdigital filter structure containing the electrooptic crystal, the theoretical and experimental tests on the interferometric mode of modulation, the design and construction of an automatic electro-optic/thermal controller for maintaining the optical bias of the modulator, and the evaluation of various crystals for use in the modulator. The basic modulator design shown in Fig. 1-1, has been demonstrated experimentally to have a modulation bandwidth of 1.2 GHz (0.9- to 1.2-GHz band) and a depth of modulation of 60% for 0.5145-μm light with 5-W rf input. However, this basic modulator will give only about a 30% modulation depth at 1.06 μm with 5-W rf drive, so that a means of increasing its efficiency must be pursued. Such means have been investigated under this contract, as reported below. However, in the interest of conciseness, only the salient points of the work done during the first three quarters are reported in subsection 3.1, since the details were presented in the earlier quarterly and semiannual reports. Work performed in the fourth quarter is discussed in detail in subsection 3.2.

3.1 SUMMARY OF WORK PERFORMED DURING THE FIRST THREE QUARTERS

3.1.1 Study of the Modulator Circuit

The modulator circuit is basically an interdigital bandpass filter having the electro-optic (EO) crystal at the output capacitance gap. The uniform electric field in this gap induces optical modulation on light focused through the crystal. Therefore, to increase the modulation index of the optical beam for a given rf drive power, the filter design must be so modified that either the internal or the terminating characteristics of the output section can be varied independently as design parameters in order to increase

the rf voltage across the modulating crystal. It has been determined, during this study, that it is preferable, in arriving at a theoretical design, to vary the terminating characteristics to maximize the desired rf voltage. Of course, any such variation must take into account the requirements of bandwidth (BW) and attenuation ripple within the passband (PB).

Choice of Low-Pass Prototype (LPPT) Filter: The Tchebyscheff Filter. Among the various standard filter types, the Tchebyscheff (equal ripple) is preferred for the modulator because of its simplicity and versatility. It is well known that for a Tchebyscheff filter, the specified maximum attenuation ripple L_{Ar} and the cutoff characteristics L_A determine the number of poles required in the LPPT (Ref. 3-1). For an optical modulator, because maximizing the rf E-field across the modulating crystal is the primary concern, the design specification on the value of L_{Ar} need not be very tight. The value of L_{Ar} has been varied within some reasonable limits to maximize the rf voltage across the crystal.

It has been shown that for a given value of L_{Ar}, one reaches a state of diminishing returns when $n > 4$. On the other hand, one requires $n \geq 4$ to achieve the required impedance transformation within the filter structure when the LPPT is transformed to the desired bandpass (BP) configuration. Therefore, for structural simplicity and high rf voltage at the EO crystal, $n = 4$ has been chosen for the modulator design. Upon transformation to the BP configuration, this results in four resonating interdigits. After L_{Ar} and n have been chosen, the normalized circuit elements for a LPPT ladder network to realize such L_{Ar} characteristics can be obtained from tables (Refs. 3-1 and 3-2).

For the modulator design, $L_{Ar} = 0.5$ dB has been chosen. This corresponds to a theoretical maximum power transmission loss of 11%. In practice, a loss of 15% may be expected. This amount of loss (reflected toward the generator) is not considered significant enough to cause concern. However, the phase characteristics within the PB do deteriorate with increasing L_{Ar} and may eventually become a limiting factor in an actual communication system. With $L_{Ar} = 0.5$ dB, $n = 4$, the LPTT ladder network is schematically shown in Fig. 3-1.

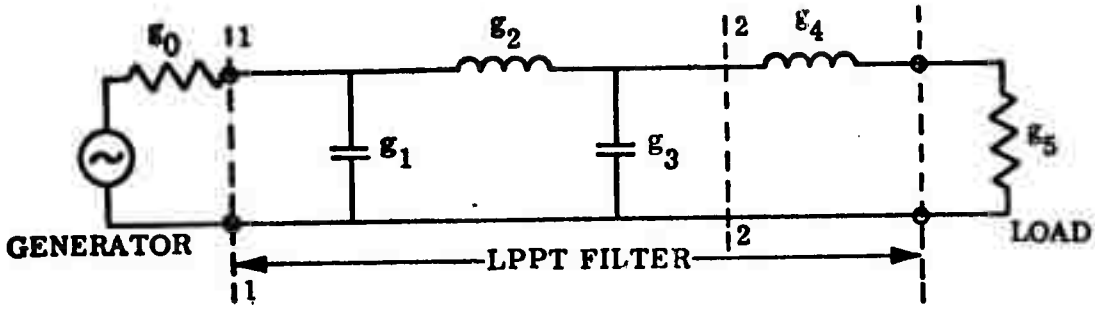

Fig. 3-1 A Low-Pass Prototype Tchebyscheff Filter Circuit, Normalized to $\omega_1' = 1$ rad/sec and Generator Impedance $g_0 = 1\,\Omega$. Values of g's are: $g_0 = 1\,\Omega$, $g_1 = 1.6703$ F, $g_2 = 1.1926$ h, $g_3 = 2.3661$ F, $g_4 = 0.8419$ h, and $g_5 = 1.9841\,\Omega$ (Ref. 3-1)

Bandpass Transformation and Physical Realization. Using standard design methods, the series inductance branches in the LPPT are transformed into series resonant branches in the BP circuit, while the shunt capacitance branches in the LPPT are transformed into shunt resonant branches. At microwave frequencies, approximations must be used to realize the lumped-element BP circuit. Many techniques of approximation exist resulting in different microwave structures. To simplify our analysis of the modulator, the capcity-loaded interdigital line (CLIL) circuit using Matthaei's technique (Refs. 3-3, 3-4, and 3-5), has been selected because it has the necessary capacitance gap for the modulating crystal.

It has been shown that an equivalent circuit of the CLIL shown in Fig. 3-2 is as shown in Fig. 3-3. To determine the values of the various circuit elements in Fig. 3-3, the image admittances, phases, reactances and susceptances of the various sections of the CLIL and the LPPT are analytically forced to agree at some key frequencies. By going through this forced-matching procedure, a set of design equations has been obtained (Refs. 3-1 and 3-5).

Once the LPPT circuit elements are obtained by specifying L_{Ar} for maximum voltage across the crystal, a BP-CLIL can be obtained by using the design equations mentioned. The result of using the design equations is to relate the CLIL elements C_1, $C_2, \ldots Z_1$, $Y_2, \ldots$, etc., to the known LPPT elements (the g's). The values obtained for the C's and Z's can be related to actual conductor dimensions, spacings, gap width, etc., by a set of charts published by Getsinger (Ref. 3-6).

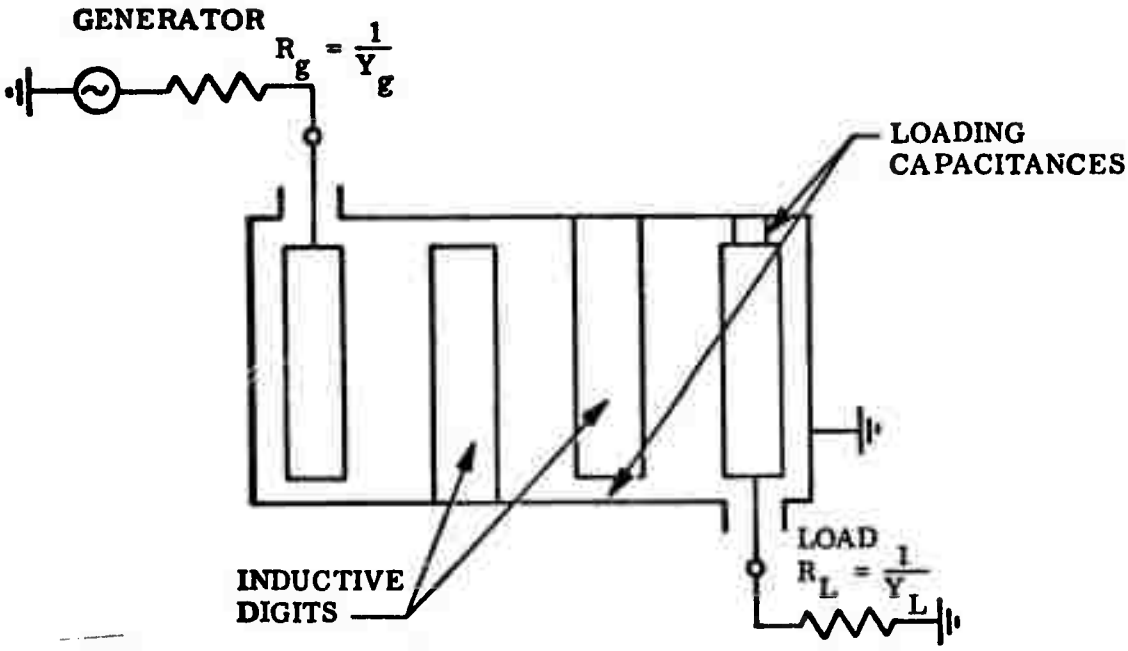

Fig. 3-2 The Strip-Line Capacity-Loaded Interdigital Line Filter, Together With Its Generator and Load

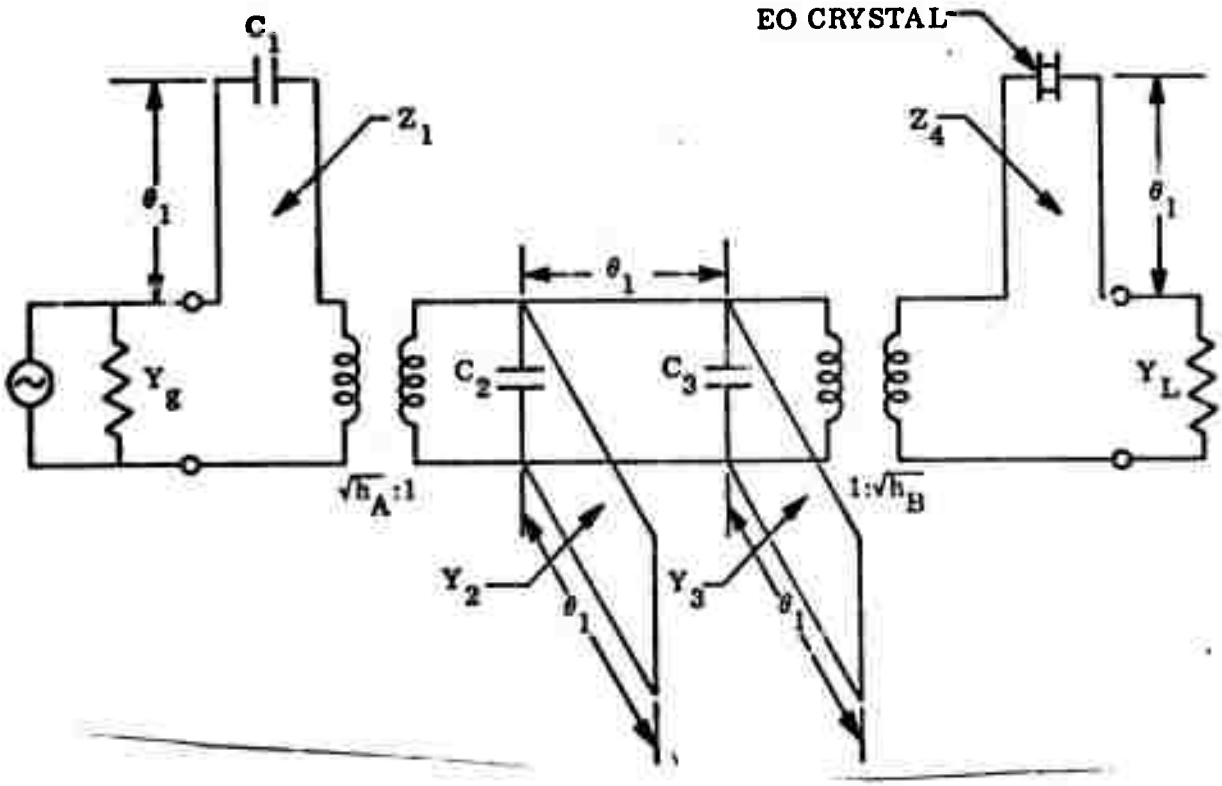

Fig. 3-3 An Approximate Equivalent Circuit for the Four-Element Capacity-Load Interdigital Line Filter

Relationship Between Attenuation Ripple and RF Voltage at the EO Crystal. Consider the output section of the CLIL equivalent circuit shown in Fig. 3-4. At midband frequency, the output section is a series-resonant circuit, with the load impedance R_L acting as the damping element of the resonant circuit. It has been shown that the peak-rf-voltage across the crystal V_{rf} is related to the power P dissipated in the load R_L by (Ref. 3-7)

$$V_{rf} = \sqrt{2P}\, Z_4 \sin \theta_1 / \sqrt{R_L} \tag{3.1}$$

where Z_4 is the characteristic line impedance and θ_1 is the electrical length of the output section. Clearly, to increase V_{rf}, the factor $Z_4 \sin \theta_1 / \sqrt{R_L}$ should be increased as much as possible.

For an EO crystal of given size, the resonating capacitance C is fixed. The resonating condition then fixes the inductance $Z_4 \tan \theta_1$, i.e., $Z_4 \tan \theta_1 = \text{constant} = \omega_0 L$

$$\therefore Z_4 \sin \theta_1 = Z_4 \tan \theta_1 \cos \theta_1 = \omega_0 L \cos \theta_1 = \cos \theta_1 / \omega_0 C \tag{3.2}$$

or

$$V_{rf} = \sqrt{\frac{2P}{R_L}} \cdot \frac{\cos \theta_1}{\omega_0 C} \tag{3.3}$$

which has its maximum at $\theta_1 = 0°$. This condition is obviously impractical, since it demands that $Z_4 \to \infty$ so that $Z_4 \tan \theta_1$ remains constant. In practice, one would therefore strive to make Z_4 as large as practical (i.e., make the conductor as thin as practical) to allow a small value of θ_1, contingent upon the allowable crystal size. For $\theta_1 < 45°$, this optimization may reach the state of diminishing returns.

On the other hand, if R_L is decreased, V_{rf} increases quite rapidly. Again, R_L cannot be arbitrarily decreased since it is related to the circuit matching and bandwidth. To understand this, it is instructive to consider, first, the LPPT circuit as

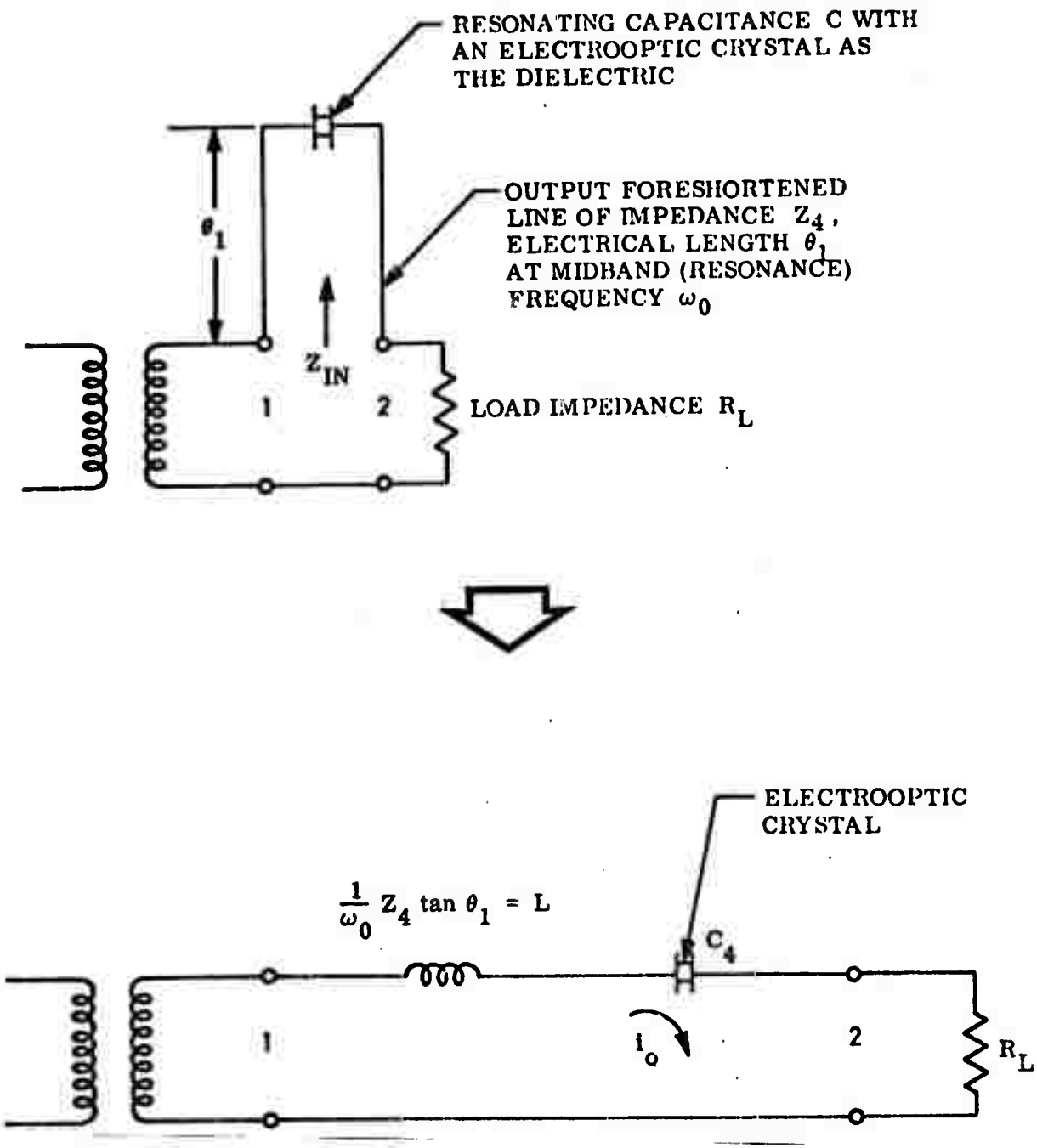

Fig. 3-4 Approximate Equivalent Circuits of the Output Section of the Capacity-Loaded Interdigital Modulator. The electrooptic crystal serves as the resonating capacitance for the inductive length of the line

a matching network to the load at terminal plane 22 in Fig. 3-1, consisting of an inductance $g_4 = L_4$ and a conductance $g_5 = G_5$. From Bode's relationship (Ref. 3-8), it can be deduced that

$$\int_0^\infty \ln \left|\frac{1}{\Gamma}\right| d\omega \leq \frac{\pi}{G_5 L_4} = \frac{\pi}{g_4 g_5} \tag{3.4}$$

where Γ is the reflection coefficient looking into terminal plane 11 in Fig. 3-1. This equation defines the best match that can be obtained over the entire frequency range; i.e., the area under the $\ln |1/\Gamma|$ versus ω curve is constant. Thus, one can either spoil the match (large $|\Gamma|$, small $\ln |1/\Gamma|$) to obtain poor power transfer over a large frequency range, or obtain a good match (small $|\Gamma|$, large $\ln |1/\Gamma|$) over a small frequency range.

From Eq. (3.3), it is clear that the parameter defining the "goodness" of the match is $1/g_4 g_5$. Therefore, for n-element filters and matching networks, since one is interested in a "good" match over a frequency range of $\omega' = 0$ to $\omega' = \omega_1'$, a "goodness parameter" decrement δ, defined as

$$\delta = \frac{1}{\omega_1' g_n g_{n+1}} = \frac{1}{\omega_1' g_1 g_0} \tag{3.5}$$

is frequently used as a design parameter. Since the g values are completely specified by the characteristics of the match (or attenuation ripple) and the number of poles, choice of any two of the three paramterers, δ, n, and L_{Ar}, uniquely determines the third.

Upon transformation into BP configuration, the decrement transforms to

$$\delta = \frac{1}{wQ} = \frac{\omega_0^2 R_L C}{\Delta\omega} \tag{3.6}$$

where w is the fractional bandwidth $(\Delta\omega/\omega_o)$, Q is the Q factor of the output section and R_L and C are as defined in Fig. 3-4. From Eq. (3.1), it is clear that δ should be small for high V_{rf}. That is, the match within the PB should be sacrificed somewhat to obtain high modulation efficiency. For this modulator design as a four-element Tchebyscheff filter, L_{Ar} has been increased from the usual filter design of 0.01 dB to 0.5 dB so that δ can be reduced from 1.4 to 0.6. This corresponds to a reduction of R_L by a factor of 2.33 for the same crystal capacitance, or an increase of V_{rf} by a factor of 1.53 for the same rf drive power.

Examples of Modulator and Transformer Design. In an actual modulator design of given L_{Ar} and n, once given the generator and load admittances Y_g and Y_L, the variables left to the choice of the designer are the line length at midband θ_1, the admittance scaling factors h_A and h_B (see Fig. 3-3), and a splitting factor d in the LPPT circuit. Proper choice of these parameters will result in a physically realizable structure.

For a generator admittance of 0.02 ℧ (50 Ω) and a load admittance of 0.0525 ℧ (19 Ω, as determined by the allowable decrement), calculations have been made for various combinations of θ_1, h_A, h_B, and d. Unfortunately, with n = 4, the circuit impedances of the internal digits became too high to be physically realizable. On the other hand, when both the generator and the load impedances as seen by the modulator circuit are both 19 Ω, physical realization can be readily obtained with n = 4. In the interest of keeping the modulator compact, it was decided to use n = 4 and external transformers together with a 19-Ω modulator circuit. The results of computer analysis also showed that for a 7-mm-long $LiNbO_3$ of square cross section with R_L = 19 Ω, values of θ_1 as low as 30° were realizable. However, since the increase in V_{rf} for a change from θ_1 = 40° to θ_1 = 30° was only 11%, while the circuit realization became quite cumbersome, θ_1 = 40° was chosen for the design. The dimensions arrived at are given in Fig. 3-5.

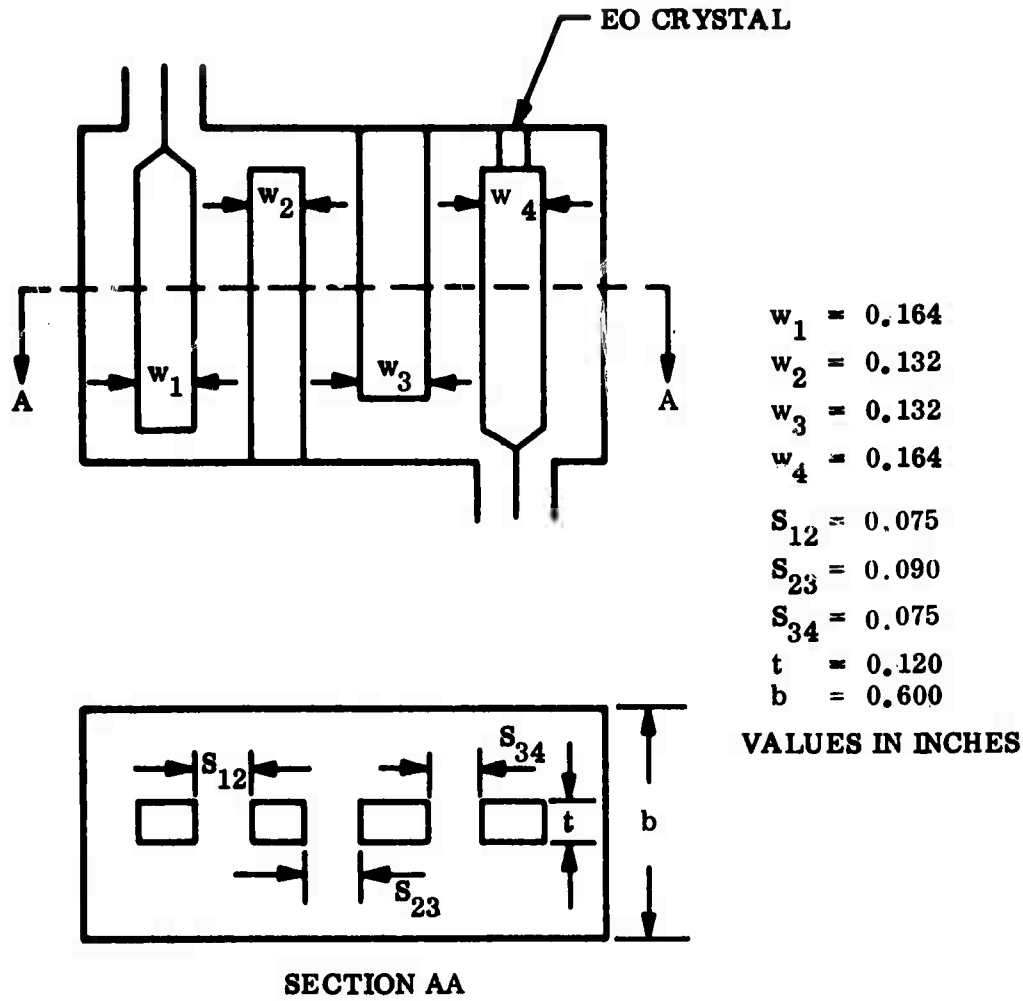

Fig. 3-5 Modulator Circuit Design: Effective Generator Impedance, 19 Ω; Load Impedance, 19 Ω

For the transformers between 19 Ω and 50 Ω, the most desirable kind for the octave-bandwidth requirement is a short-step Tchebyscheff transformer because of its simplicity and physical dimensions (Ref. 3-9). These were designed to have 100% bandwidth to ensure that they would not limit the bandwidth performance of the final modulator. The dimensions are shown in Fig. 3-6.

RF Tests and Fine Adjustments on Model 1. Since the theory used for the design of these circuits is approximate because of the distributed nature of the high-frequency

circuits, certain empirical design allowances must be provided for in defining the circuit parameters of the numerical analysis. These include bandwidth, band center frequency, and circuit parasitics. Even with such allowances, much effort had to be spent on "cold testing," "fine tuning," and modifying the circuits after fabrication.

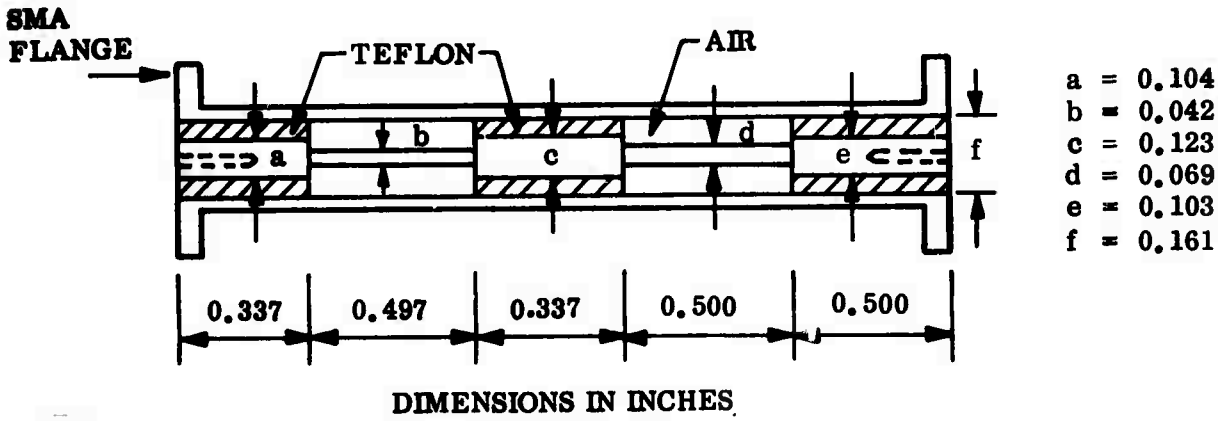

Fig. 3-6 A Four-Section Short-Step Tchebyscheff Transformer for 50:19 Ω Impedance Transformation

At the end of the third quarter, rf performance approximating the design values had been obtained. Figure 3-7 shows the input VSWR as a function of frequency where the two transformers were connected back-to-back. That is, the transformers were combined so that the two 19-Ω ends were connected, giving 50-Ω input and output impedances for the combination. The reference trace shown in Fig. 3-7 was for a VSWR of 1.67. Therefore, the VSWR of the transformer combination was less than 1.67 over the entire 1 – 2 GHz band. Figure 3-8 shows the input VSWR of the modulator/transformer combination together with a reference VSWR of 2.3. This combination is referred to as Model 1. From Fig. 3-8, it was clear that despite the allowance made in the design parameters, the actual bandwidth was still narrower than the desired 1 GHz. During the fourth quarter, the design was further improved so that the rf bandwidth was extended to greater than 1 GHz.

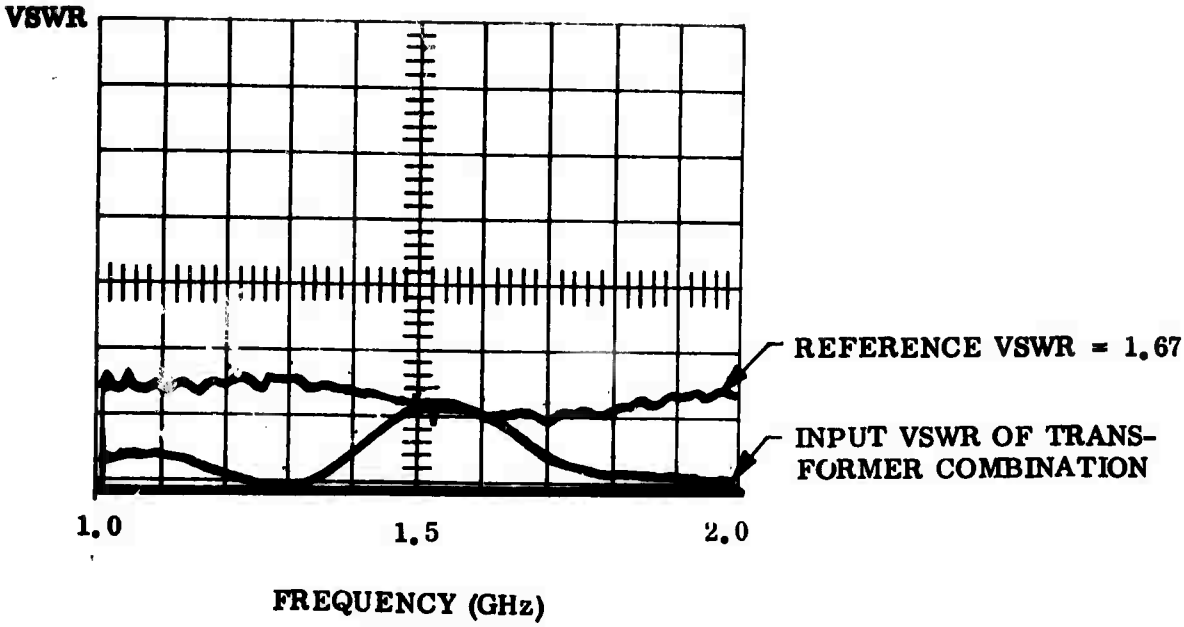

Fig. 3-7 Input VSWR of Two 50:19 Ω Transformers Connected Back-to-Back

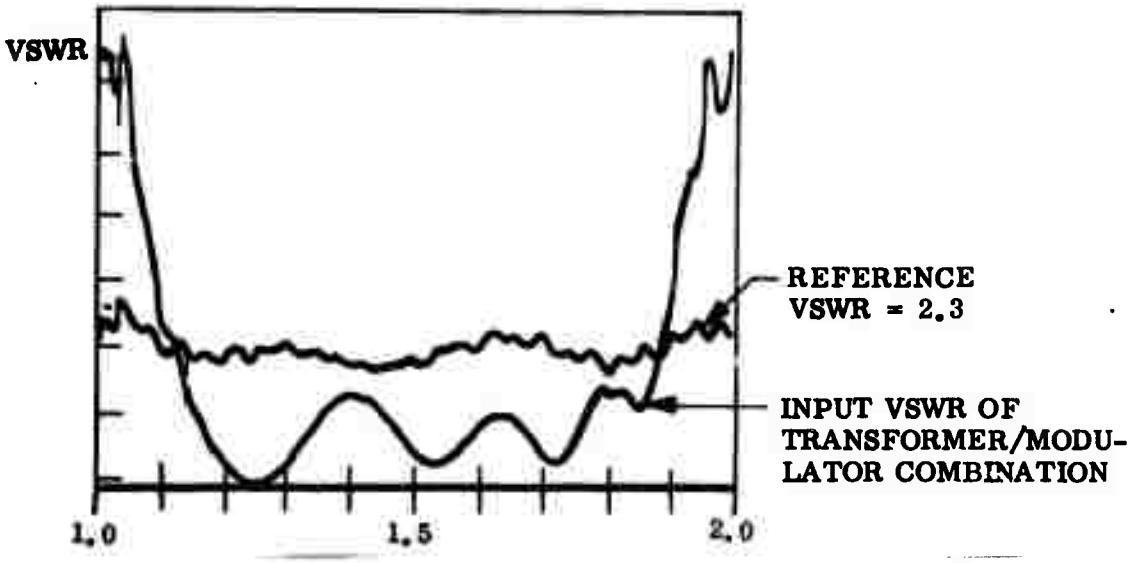

Fig. 3-8 Input VSWR of the Modulator/Transformer Combination Shown in Fig. 3-4

3.1.2 Interferometric Modulation Studies

In the interferometric mode of modulation, the modulator crystal behaves as a Fabry-Perot etalon whose effective optical length is varying at the modulating signal frequency. By properly selecting and controlling the quiescent optical length of the crystal (via temperature or dc bias), the modulator can be biased so that an rf signal applied to the electrooptic crystal will cause intensity modulation of single-mode laser radiation transmitted through and reflected back from the crystal. In this mode of operation, the depth of modulation is defined as the peak-to-peak change in the light intensity (at the fundamental frequency) divided by the cw intensity of the incident laser light so as to correspond to the conventional "depth of modulation" definition for the birefringence modulation at quarter-wave optical bias.

As the crystal reflection coefficients are increased in the interferometric modulator, the number of partial waves having significant amplitudes increases. Because of the finite propagation time of each partial wave within the modulating crystal, the rf modulation impressed on each partial wave will be the time average during this propagation time. The modulation will be shifted in phase from that on the previous partial wave. For higher reflection coefficients, less rf power is required to attain the same depth of modulation, but at the same time, more distortion and phase delay are produced in the modulation. Computer analysis were used to show the tradeoffs between these quantities.

Computer runs for $LiNbO_3$ crystals, of dimensions 0.5 by 0.5 by 5 mm and 0.5 by 0.5 by 7 mm having various reflectivities, were made for the modulation of 0.6328-μm light at various rf drive levels. Some of the results were included in earlier reports and will not be repeated here. The reflectivities and crystal dimensions used corresponded to actual experimental conditions. Results indicated that the reflected beam had a greater depth of modulation but possessed higher harmonic distortion and phase deviation than the corresponding transmitted beam. Higher reflectivity produced greater depth of modulation; however, harmonic distortion and phase deviation increased more rapidly than the depth of modulation.

Theoretically, the choice of crystal surface reflectivity for use in a given communication system depends critically on the tolerance of the system to harmonic distortion and phase deviation. In practice, since the crystals obtainable from vendors were not truly homogeneous and the faces were not exactly flat and parallel, the wavefront of light is distorted with each pass within the crystal. This distortion was found to be the limiting factor for interferometric modulation, limiting the maximum useful reflectivity.

Computer results showed that for a reflectivity of 0.35 the approximation of using only two round-trip reflections within the crystal yielded a modulation depth that was only 3.2% below that for a very large number of reflections. For a reflectivity of 0.5, four round-trip reflections were required for a result that was within 1.5% of that for a very large number of reflections. For this reason, a reflectivity in the range of 0.3 to 0.35 was judged best for currently available crystals.

The high index of refraction of the $LiNbO_3$ crystals (~2.2) causes the uncoated crystals to have a surface reflectivity of 0.14 in the visible. One round-trip reflection (two partial waves) within the crystal produces modulation that is within 3.5% of that for many reflections. Five crystals of dimensions 0.5 by 0.5 by 7 mm were measured in the laboratory and produced depths of modulation of 20 to 30% with 5 W of drive power. The computer analysis predicted a 35% modulation depth, so there was reasonable agreement between the analysis and the measured results. Within the group of five crystals, the static reflection curve varied. Crystals having a lower reflection ratio produced a smaller depth of modulation.

Two of the above five crystals were selected for coating with 0.3 to 0.35 reflectivity in the visible for further experimentation. The coating operations, performed simultaneously on both crystals, did not produce equal reflectivities on each end: the measured reflectivity of one surface was 0.26; of the other, 0.32. Experimental results showed that for a 2-W drive, a modulation depth of 30% was obtainable for the transmission mode. This compared well with a theoretical value of about 35%. However, as the drive power was increased, further crystal heating, which resulted

in greater distortion of the crystal and consequently of the interferometer configuration, caused the interfering wavefronts to distort considerably. No substantial increase in modulation depth was obtained at drive levels greater than 2 W. Thus, the successful testing of this type of modulation will have to await the availability of better quality crystals with lower rf loss tangents and improved cutting techniques.

3.1.3 Electrooptic/Thermal Control Circuit

With the interferometric type of modulation, adjustment of the optical bias point cannot be effected by means of an optical compensator, since the change of the optical length has to occur inside the reflecting surfaces of the crystal. Control of the crystal temperature to change the crystal length may be used, but that alone is not fast enough to respond to the microwave power fluctuations that normally occur. To respond to such fluctuations, an electronic circuit, which combines the electrooptic effect with thermal control to provide continuous automatic control of the optical bias point, was devised. The electrooptic effect is used to provide fast, short-term control; the temperature is used to provide long-term control. Clearly, this type of control is also useful for the birefringence modulation when fast response time is required as would be the case in an actual high-data-rate communication system. Such a circuit was designed, built, and tested.

A schematic view of the controller for use with birefringence modulation is shown in Fig. 3-9. Two photodiodes are used to define the optical bias point by sensing the optical power in the two orthogonal polarizations after the modulator. The diodes are electrically loaded so that, at the desired optical bias point, equal signals are produced. During operation, the difference between the two signals (representing a deviation from the desired bias point) is amplified by a differential amplifier followed by a high-voltage stage. The high-voltage stage is capable of applying a nominal ±300V to the modulator crystal and of following transients with time constants of several milliseconds to provide good "instantaneous" control of the bias point.

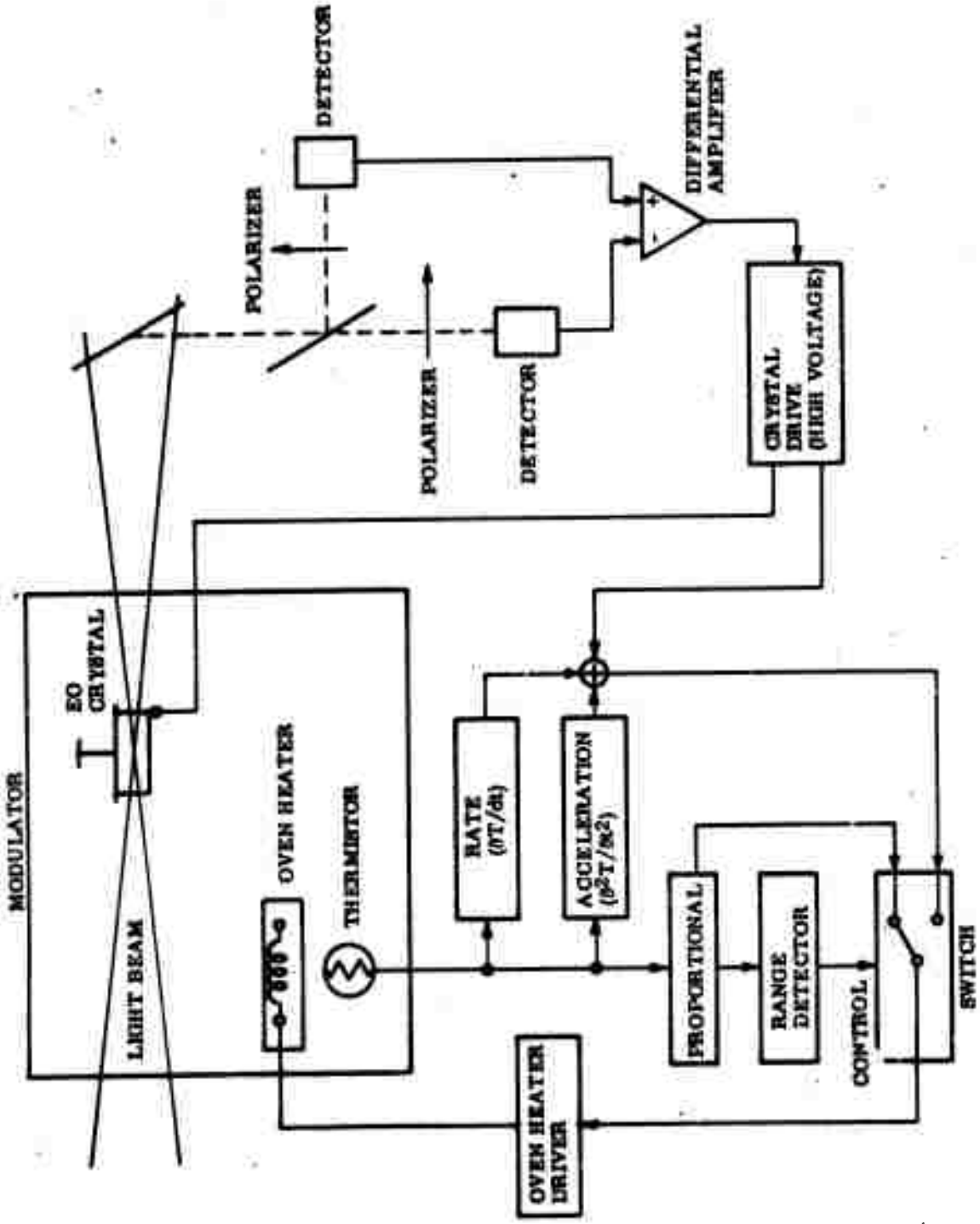

Fig. 3-9 Automatic Bias Control of Modulator

Since it was observed that a high bias electric field on the crystal caused a certain amount of beam distortion, the compensating field should always approach zero in its quiescent state. In the first controller design, this was accomplished by using this crystal bias voltage to actuate the crystal-oven heater control circuit so as to change the oven temperature to make the bias voltage approach zero. The crystal temperature will then vary to the necessary temperature to maintain proper bias. Since the thermal time constant of the oven is of the order of several minutes, thermal control was relatively slow. Under these conditions, if the fluctuation in microwave power was strong, it was still possible for the oven temperature to become too high or too low. For this reason, the oven temperature was monitored while it is being controlled by the crystal bias voltage, and if the temperature went outside a predetermined range of operation, the oven control was automatically switched to a thermistor probe for a period of time. After the temperature had time to center itself in the operating range, the control was automatically switched back to the crystal bias voltage. This circuit had successfully kept the oven temperature within a reasonable operating range for a variety of changing laboratory conditions.

While the oven heater was controlled by the crystal bias voltage, the temperature could go into slow oscillations, which would prevent stable operation. This was due to the fact that there was a long time delay before the crystal reacted to any thermal change in the oven heater. To stabilize the oven temperature, both the first and second derivatives of the temperature were combined with the optical bias voltage to provide an error signal for the oven heater. With such an error signal, the heater was electrically damped so that the temperature could not change at a rate too fast for the crystal to follow. This was satisfactory for achieving automatic compensation for long periods of time, although tighter thermal coupling between the heater and the crystal was still desirable. Modifications of this design were made as described in subsection 3.2.3.

3.1.4 Beam Profile Studies in $LiNbO_3$ and Evaluation of Efficient Crystals

Crystal Damage and Beam Profile Studies. It is well known that shorter wavelength radiations induce more optical damage in the form of inhomogeneities in refractive indexes than longer wavelength radiations in crystals such as lithium niobate. Therefore, tests were made on $LiNbO_3$ crystals, 0.3 by 0.3 by 7.0 mm, in a modulator using the output of an argon laser consisting of several lines in the 0.4880 – 0.5145-μm range, totaling about 3/4 W of optical power rather than using 1.06 μm radiation. Since the crystals did not suffer from damage at these wavelengths, there will be no problem in operating at 1.06 μm using the same optical power. At 180°C, up to 700 mW of optical power between 0.4880 and 0.5145 μm was focused to 80-μm diameter through the crystal, corresponding to a power density of 14 kW/cm^2, without any observable damage. The far-field pattern of the transmitted beam was scanned using a pinhole, showing little change from the Gaussian beam. (The details of these measurements have been reported in the First Quarterly and the Semiannual reports.) Therefore, it was concluded that there would be no optical damage problem with 1.0 W of 1.06-μm radiation focused through this type of crystal, so long as it was maintained at 180°C.

Preliminary tests were also run on a sample of strontium barium niobate (60% Sr to 40% Ba). After irradiation using 0.4880 and 0.5145 μm at power densities up to 9 kW/cm^2, the crystal showed brownish discoloration which faded away slightly after removal of the radiation. However, annealing at high temperatures did not remove the discoloration, but rather changed its position. It was suggested by the vendors that the discoloration was due to slight inclusion of platinum during growth and poling. No further experiments were made on this sample. No beam profile measurement was made, since the sample was not optically polished.

It has also been informally reported that $LiNbO_3$, after being operated in air at elevated temperatures (e.g., 180°C) for a period of time, became yellow. It had been speculated that this discoloration was due to the gradual loss of oxygen atoms,

under heat, from the crystal structure. The experience in our laboratory, with $LiNbO_3$ operating in air at 180°C for over a year, did not support this observation. However, to ascertain that such problem will not occur when $LiNbO_3$ operates in vacuum, tests were run in the laboratory by heating a 5 by 5 by 5 mm sample of $LiNbO_3$ in a vacuum bell jar while its transmission is monitored at 0.6328 μm. After 23 hr at about 200°C, and then 3 hr at 350°C, no decrease in transmission was observed. In addition, the transmission of the crystal from 0.25 to 1.2 μm was also measured in a Cary Model 14 spectrophotometer before and after the vacuum test; no degradation in transmission, especially near the absorption edge of 0.3 to 0.4 μm, was observed. Since the shift in absorption edge was a very sensitive measure of yellowing, it was concluded that under our test conditions, no degradation in optical transmission was observed.

Evaluation of Efficient Crystals. Although it was anticipated that good-quality, efficient crystals such as barium sodium niobate (BANANA) would become availabe for this study, crystals were not obtained until late in the second quarter; one each of barium sodium niobate and strontium barium niobate (SBN 50-50). Unfortunately, the optical quality of these crystals was rather poor, and many fringes in the birefringence extinction pattern were observed. It appeared that these fringes were due mainly to the strains induced during crystal fabrication, although some intrinsic problems such as crystal nonuniformity and striations were also present. The details had been reported in the Semiannual report.

Although the BANANA quality was poor, tests for birefringence modulation were made. Results obtained were discouraging. At 2-W drive level, 28% modulation depth, as compared with a theoretical 55%, was the best obtainable. For SBN 50-50, matching to the present circuit was not possible because of its high dielectric constant. Also, because of its poor optical quality, it was not deemed advisable to design a circuit specially for this crystal.

3.2 WORK PERFORMED DURING THE FOURTH QUARTER

3.2.1 Study of the Modulator Circuit

Modulation Tests on Model 1. Modulation tests were performed on Model 1 containing a $LiNbO_3$ modulating crystal of dimensions 0.3 by 0.3 by 7 mm, AR coated for minimum reflectivity at both 0.53 and 1.06 μm. For convenience, an Argon laser radiating at 0.5145 μm was used as the laser source. A TIXL55 silicon avalanche photodiode whose frequency response had been calibrated was used as the detector and substitution method was used to determine the modulation index (Ref. 3-9). Modulation index versus modulating frequency curves were obtained, as shown in Fig. 3-10, which varied with the tuning of the modulator.

It can be seen from Fig. 3-10 that for 5-W rf input, the modulation index for 0.5145-μm radiation at the low-frequency end of the rf band was about 78%. The high-frequency 3-dB point (i.e., the point at which the modulation index is 0.707 times the peak value) was found to be 1.86 GHz. It is also clear from the figures that the center frequency of the modulator is down-shifted. This downshifting was due to the overcompensation allowed in the finger lengths to account for the approximateness of the design equation. Such a downshift can be corrected for in a new design by allowing less excess length in the finger lengths. Throughout the tests, it was also found that the combined rf reflection and rf insertion losses of the modulator were high: they were about 2 dB over the major portion of the band and about 3-dB in the 1.4 to 1.6 GHz and in the 1.8 to 2.0 GHz region. Nevertheless, the modulation index obtained over the band was still reasonable across the 1.0 to 1.85 band, as evidenced by the plot.

Theoretically, the modulation index M_d for birefringence modulation at quarterwave optical bias is given by (Ref. 3-9)

$$M_d = 2 J_1\left[\sqrt{2}\, k(\ell/d)\left(Z_4^2/R_L\right)^{1/2} P^{1/2} \sin \theta_1\right] \tag{3.7}$$

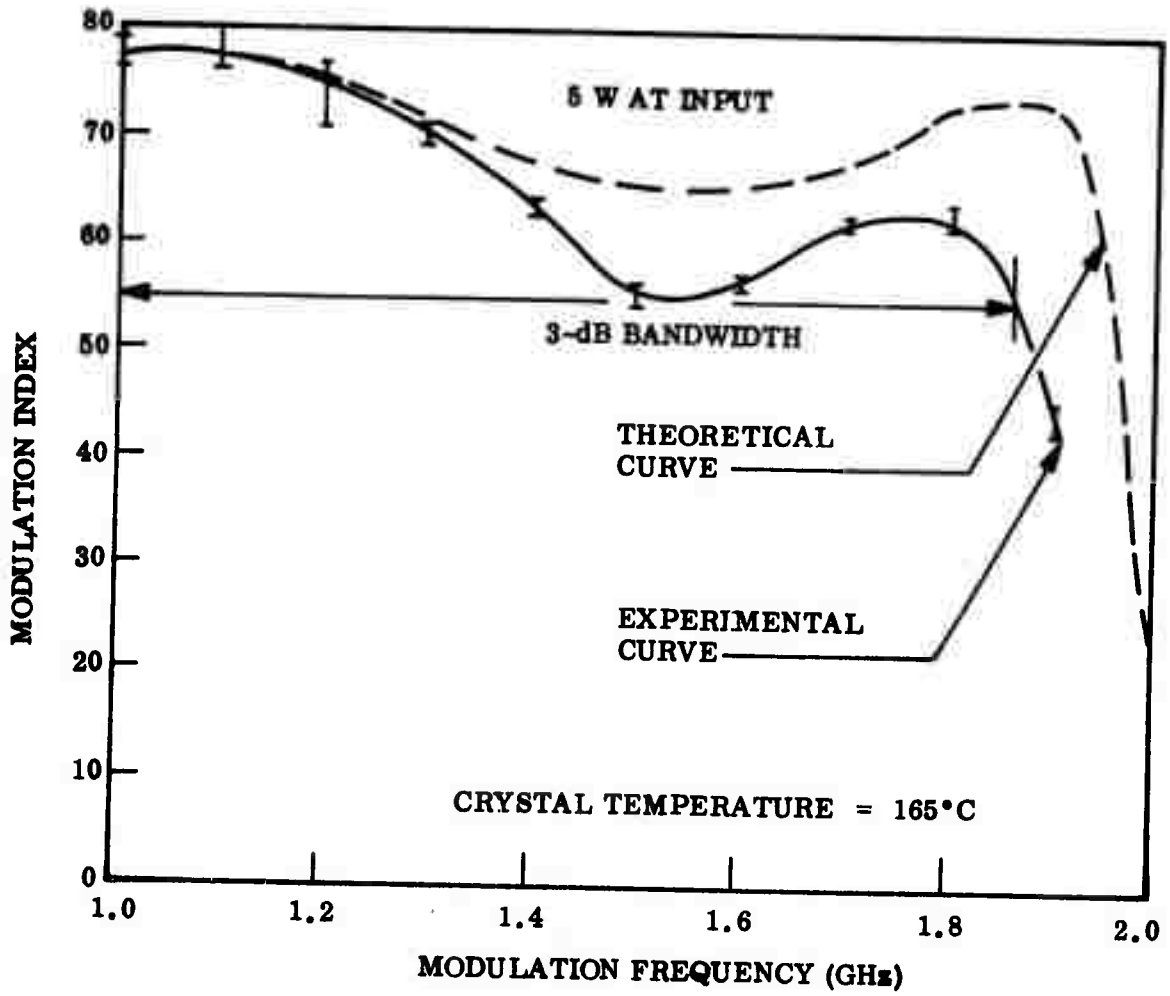

Fig. 3-10 Modulation Index as a Function of Frequency of 5-W of rf Drive Power at the Input

where

J_1 = Bessel function of the first kind, first order

k = constant containing the appropriate optical coefficients, $(\pi/\lambda_o)\ (n_e^3\, r_{33} - n_0^3\, r_{13})$

ℓ/d = crystal length-to-thickness (aspect) ratio and other symbols explained earlier in this report

For $LiNbO_3$, $k \approx 1.35 \times 10^{-3}$ at $0.5145\ \mu m$, and for this modulator circuit and crystal, $\ell/d \approx 7/0.3 = 23.3$, $Z_4 = 68.2\,\Omega$, $R_L = 19\,\Omega$, $\theta_1 = 40°$. As has been mentioned earlier, the combined reflection and insertion losses of the modulator was high so that the power transmitted through to the rf load was typically about 2 to 3 dB below that at the input, i.e., the rf power available for setting up modulation voltage, P was lower than the 5 W at the input to the circuit by 2 to 3 dB. Using these numbers, one could then arrive at theoretical values for modulation indexes at various frequencies. These are plotted in Fig. 3-10 as the theoretical curves; it is obvious that good agreement has been obtained.

In a practical modulator, obviously, high reflection and attenuation losses are undesirable since one must provide the high input driving power for producing the desired modulation index. The losses can be attributed in part to the nonplated brass circuit elements and in part to the high rf losses in the crystal. During tests it was observed that by switching on the 5-W rf input power, temperature changes in the crystal caused a total change of 11 to 28 birefringence fringes. (One fringe corresponds to a temperature change of 1.4°C in $LiNbO_3$.) Clearly, considerable rf power loss was occurring within the crystal. For this reason, the power was not increased beyond 5 W at the input for this modulator.

Design of Modulator Model 2. During the fourth quarter, another modulator, having different design bandwidth and digit length allowances, was designed and constructed. The design parameters were:

$Y_A = Y_B = 0.0525\mho$ (19 Ω system)

$\theta_1 = 40°$

$\omega_o = 2\pi \times 1.65 \times 10^9$ rad

$\Delta\omega = 2\pi \times 1.2 \times 10^9$ rad

b = 0.6 in.

t = 0.12 in.

These resulted in a design as shown in Fig. 3-11.

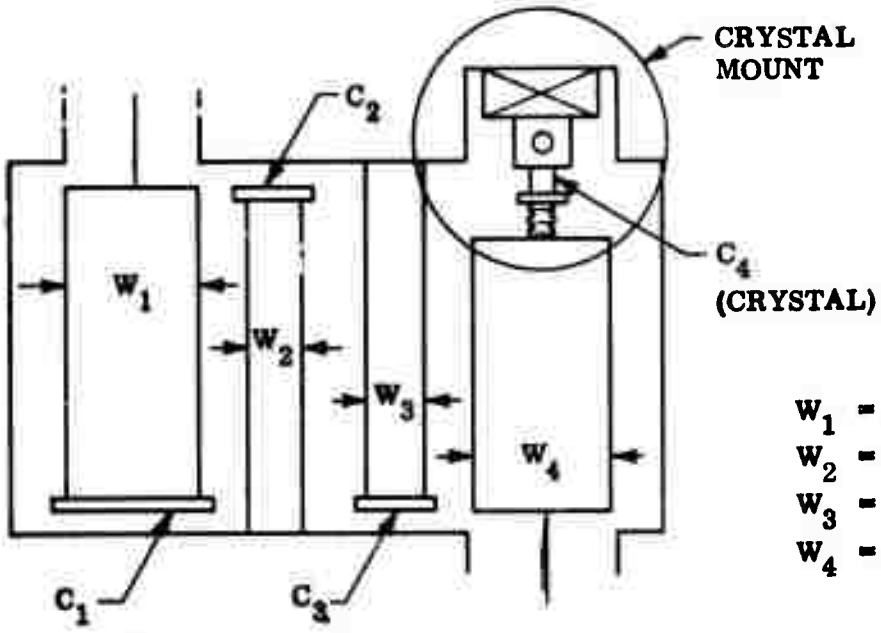

$W_1 = 0.2094$ in.
$W_2 = 0.08166$ in.
$W_3 = 0.08162$ in.
$W_4 = 0.2094$ in.

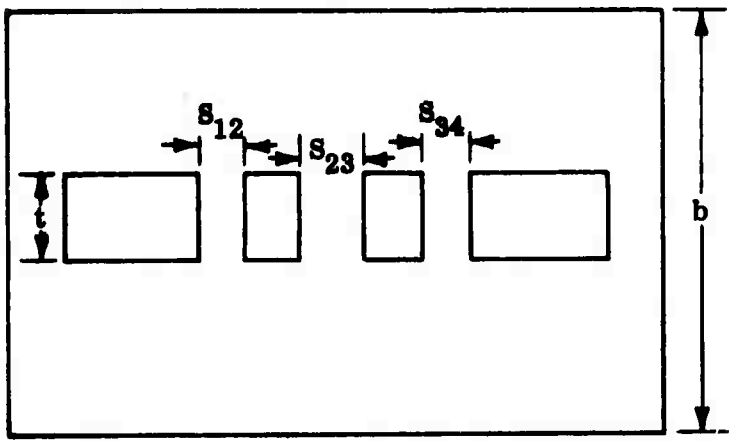

$C_1 = 1.8741$ pF
$C_2 = 1.4456$ pF
$C_3 = 1.4456$ pF
$C_4 = 1.4456$ pF

$S_{12} = 0.0666$ in.
$S_{23} = 0.0930$ in.
$S_{24} = 0.06658$in.

Fig. 3-11 Design Values for Modulator Model 2

The detailed view of the crystal mount is shown in Fig. 3-12.

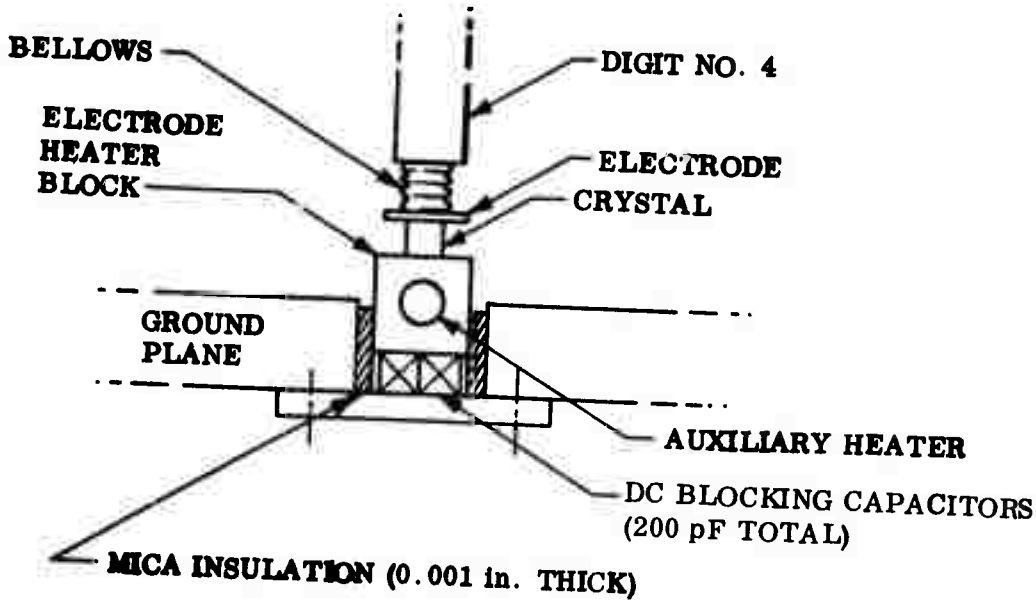

Fig. 3-12 Details of the Crystal Mount

Comparison of this construction with that shown in Fig. 1-1 indicates that the inductance of the bellows was made a part of the inductive digit, thereby eliminating much of the uncertainty of the rf ground point. Good rf ground was further provided by large dc blocking capacitors which were soldered to the electrode/heater block which in turn was rf-grounded through thin mica wafers. An auxiliary heater was provided in the electrode/heater block to give fast thermal reaction time to the crystal during normal operation in the electrooptic/thermal compensation mode. In this way, the temperature reaction time was reduced to about 5 sec from the original 15 min. This was done to reduce the choice of mode of operation error under extreme circumstances. Obviously, the controller design had to be changed to accommodate this feature; this is discussed in subsection 3.2.3.

The 50- to 19-Ω transformer was redesigned and fabricated to take into account the results of our experience with fine tuning. The final dimensions are as shown in Fig. 3-13.

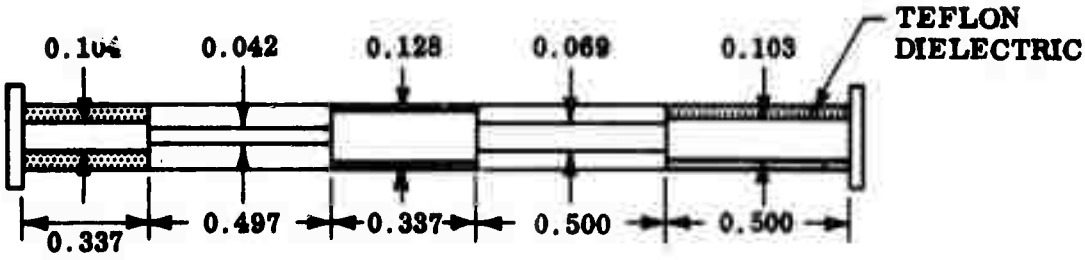

ALL DIMENSIONS IN INCHES.

Fig. 3-13 Design of Transformer Model 2

All the metal parts were silver or gold electroplated to minimize rf losses.

RF Tests of Modulator and Transformer Model 2. The transformers operated satisfactorily, as can be seen from the VSWR traces shown in Fig. 3-14. Curve 1 was taken for one transformer and a 19-Ω combination, while curve 2 was taken for both transformers connected back-to-back with a 50-Ω load. The reference trace was for a VSWR of 1.67.

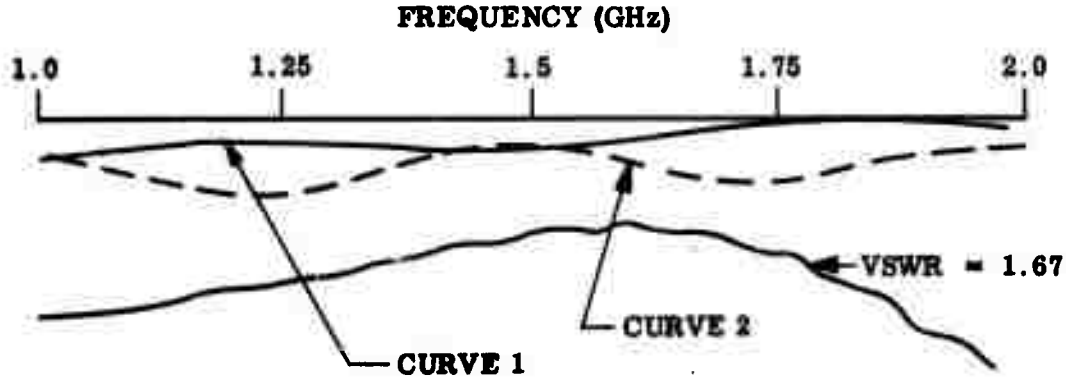

Fig. 3-14 Input VSWR of the Model 2 Transformers. Curve 1: Transformer Model 2 and 19 Ω load combination. Curve 2: Two transformers connected back-to-back with 50 Ω load

The modulator originally had its frequency response shifted toward high frequencies because of undercompensation of the digit lengths this time. When it was first

fabricated, it showed a good 4-ripple Tchebyscheff's type of response between 1.2 and 2.4 GHz. After much retuning, the response curve was downshifted to cover the 1 to 2 GHz band. However, after the retuning procedure, a problem appeared with the rf ground in this construction: A broad resonance centered at about 1.25 GHz was observed. If the electrode/heater block was dc grounded, this spurious resonance could be readily tuned out. Rather than delaying the optical tests to determine the cause of this resonance, we decided to operate with the dc ground condition. The results of the VSWR measurements are shown in Fig. 3-15. Curve 1 shows the VSWR trace of the transformer/modulator combination taken while the modulator was at room temperature, and curve 2 shows the VSWR of the combination at 175°C. It is seen that the VSWR deteriorated slightly at higher temperature. The rf insertion loss, however, was constant at about 1 dB, as shown in Fig. 3-16. Quick measurements performed outside the 1 to 2 GHz band indicated that good rf responses between 0.9 to 1.0 and 2.0 to 2.3 GHz were also obtainable.

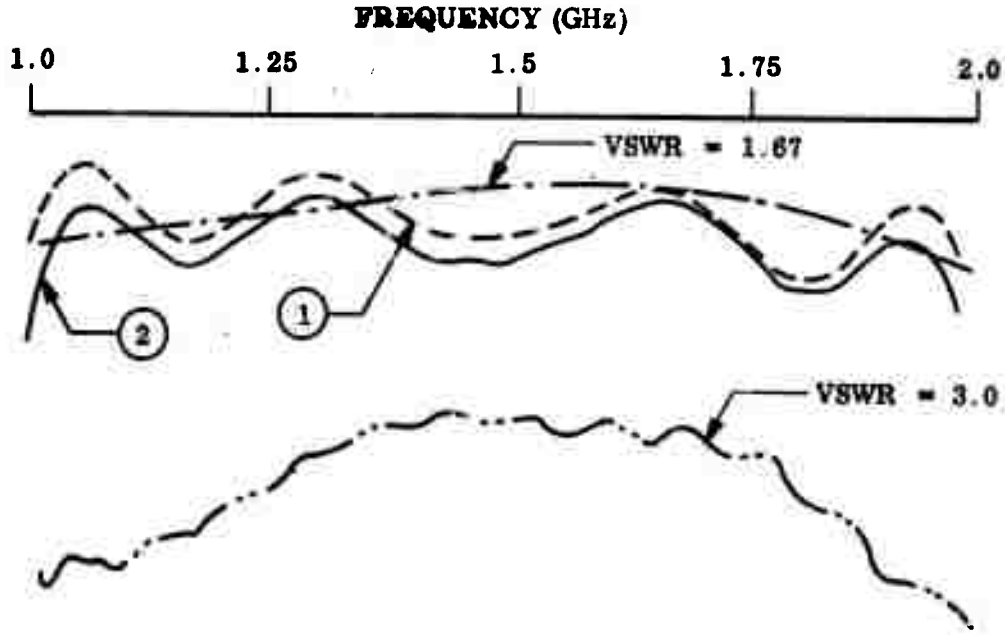

Fig. 3-15 Input VSWR of Model 2 Transformer/Modulator Combination. Curve 1: room temperature. Curve 2: 175°C. Two reference traces are also shown

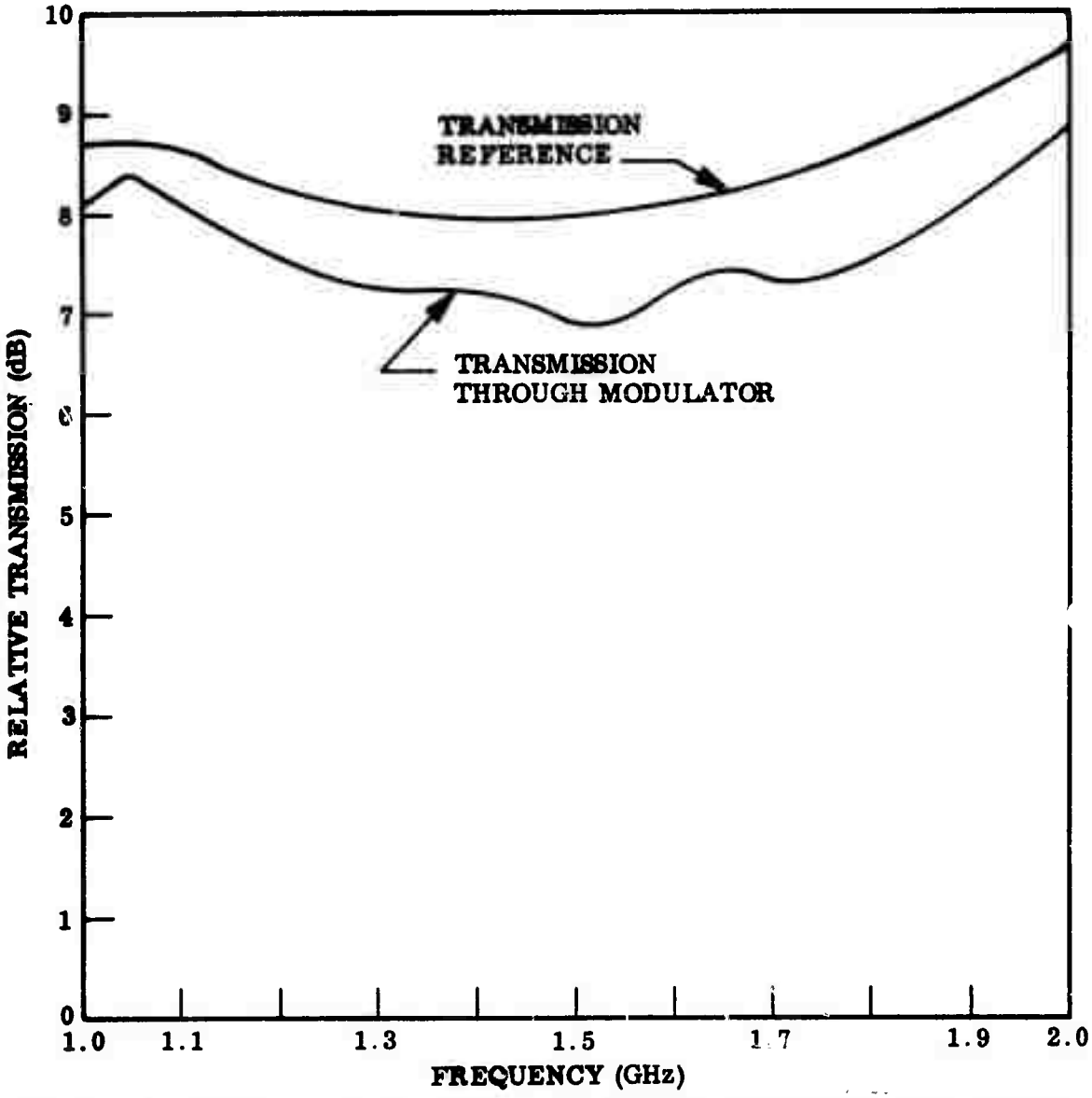

Fig. 3-16 Insertion Loss of Transformer/Modulator Combination (Crystal IV-I-1-3, No dc Blocking Capacitor in Crystal Mount)

Optical Modulation Tests on Model 2. Tests on modulation index were made on Model 2 transformer/modulator by the substitution method using the TI XL 55 diode. The modulating crystal used was a 0.3 by 0.3 by 7 mm $LiNbO_3$ crystal, AR-coated for both 0.53 and 1.06 μm. The radiation that was modulated was again the Argon 0.5145-μm line for convenience. Curves of modulation index versus frequency were obtained and are shown in Figs. 3-17a and 3-17b.

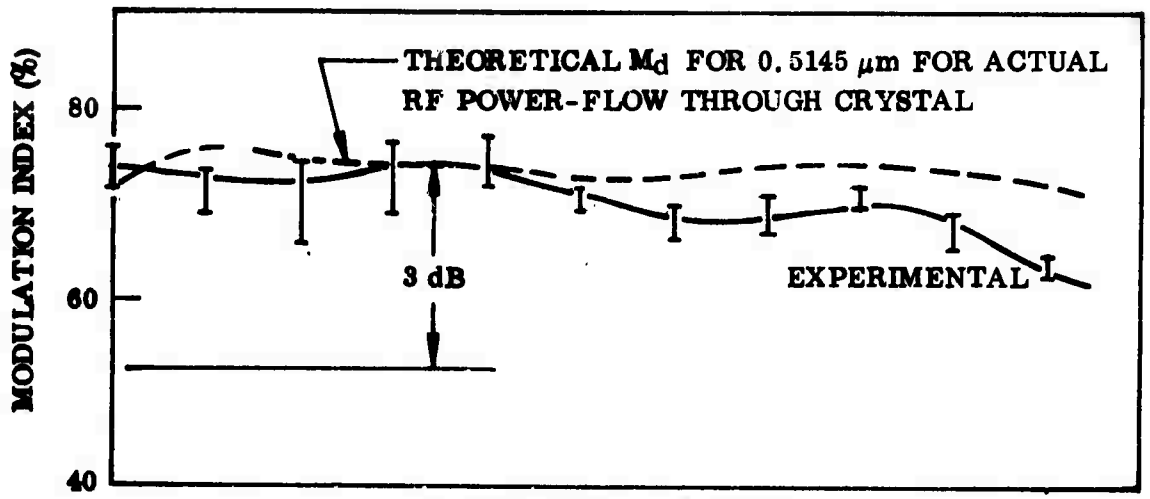

A. 5-W RF POWER AT INPUT

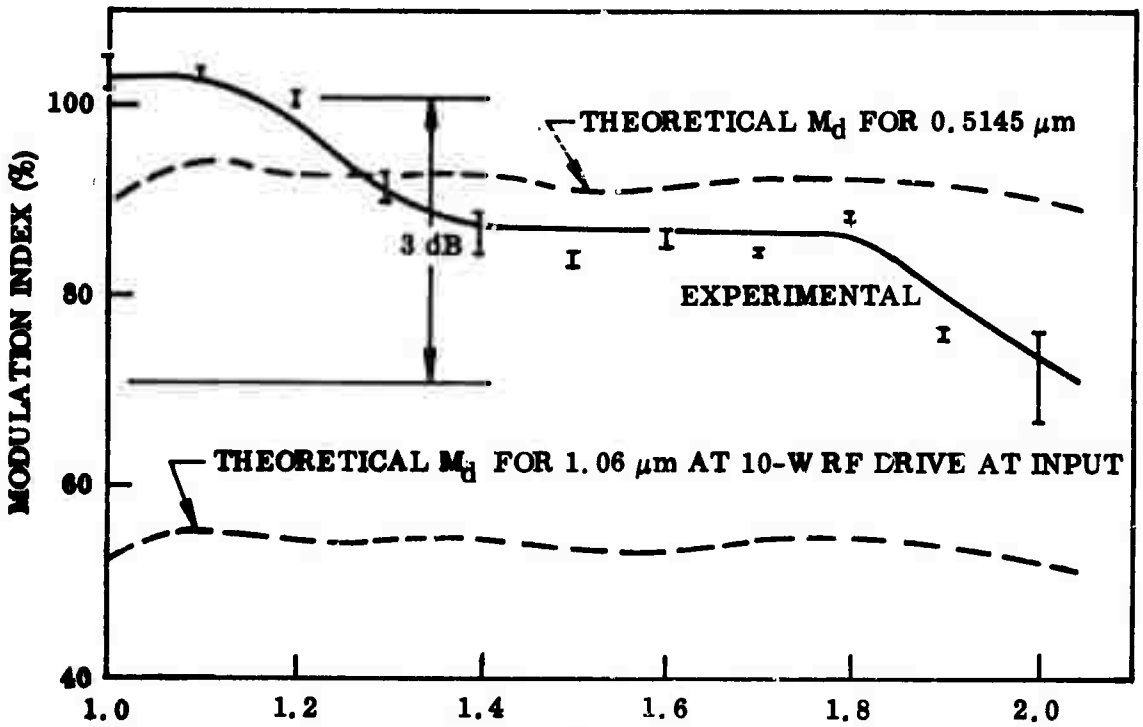

B. 9-W RF POWER AT INPUT

Fig. 3-17 Modulation Index as a Function of Frequency for Various rf Drive Levels at the Input

Figure 3-17a is that for 5-W rf drive at the input. It is seen that approximately 70% modulation depth has been obtained across the band; the droop in modulation depth above 1.8 GHz is primarily due to the uncertainty in diode frequency response calibration. In any event, taking the peak value of M_d (modulation index) as 74%, the 3-dB points will fall on 52.3%, which is much below the measured value of M_d at the band edges. Therefore, this modulator has 3-dB bandwidths much greater than 1 GHz. From our approximate measurements (subsection 3.2.1) on total rf bandwidth, it is estimated that the modulation band of this modulator may be 0.9 to 2.3 GHz, for a 1.4-GHz bandwidth.

Theoretically, Z_4 for this modulator is 61.4 Ω. Substituting this value into Eq. (3.7), the theoretical values of M_d at various frequencies for the actual power flowing through the modulator crystal (about 1.4 dB below that at the input due to insertion and cable losses), have been calculated. These are also shown in Fig. 3-17a; it is seen excellent agreement is obtained with the measured values.

Figure 3-17b shows that for 9-W input, both experimental and theoretical curves for 0.5145 μm are shown. Again, it is seen that good agreement is obtained. On the same figure a theoretical curve is also shown for modulation depths at 1.06 μm at 10-W rf drive at the input. It is seen that about 52% modulation depth at 1.06 μm is theoretically obtainable for this modulator. Since good agreement between theoretical and experimental results has always been obtained; we are confident that 50% modulation depth for 1.06 μm radiation at 10-W input drive level can be achieved in practice using modulator Model 2.

3.2.2 Crystal Fabrication

There have been continuing problems in obtaining crystals whose optical quality has not been degraded by induced strains in the final cutting and grinding process. Since vendors have been unable to perform this final fabrication satisfactorily, LMSC began an in-house supported program to develop the techniques. The goal is to cut

and grind the modulator crystals to final size, as small as 0.25 × 0.25 mm in cross section and as long as 10 mm, while inducing very low strain. The results obtained to date on $LiNbO_3$ crystals show that considerable progress is being made.

We have found that using a reciprocating diamond-impregnated wire saw for cutting the crystals induced much less strain than using the more conventional loop-type of wire saw. Proper adjustment of the cutting speed and coolant rate has resulted in a negligible increase in the observable strain after cutting. For the grinding operation, the preferred technique uses diamond-impregnated copper wheels rotating at low speed and employs a copious supply of coolant. As an example, Fig. 3-18a shows the uniform birefringence extinction pattern of a $LiNbO_3$ crystal, of dimensions 0.25 by 0.3 by 5 mm, cut and ground by the present method. The extinction ratio obtained was greater than 20 dB. This was a vast improvement over the typical pattern of samples obtained from vendors, shown in Fig. 3-18b (0.3 by 0.3 by 7 mm), having an extinction ratio of 16 to 13 dB.

3.2.3 Modification of the Electrooptic/Thermal Control Unit

Under extreme conditions optical bias instabilities can develop due to the long thermal reaction time of the crystal if its temperature is controlled just by the oven heating control. To alleviate this condition, we decided to incorporate an auxiliary heater near the crystal. Experiments showed that a reaction time of 5 sec was possible. To use this method for control, the controller circuit had to be modified. Figure 3-19 shows the schematic of the modification.

As before, the two detectors and polarizers monitor the optical bias point. A drift in bias results in an error signal which actuates the high voltage bias control as well as the control to the auxiliary heater which, as can be seen from Fig. 3-12, is directly underneath the crystal. This results in a sufficiently fast reaction time that the control loop should be stable using only the first derivative of temperature in combination with the optical bias voltage to provide the error signal for the auxiliary heater. As before, a predetermined range switching control is provided so that any

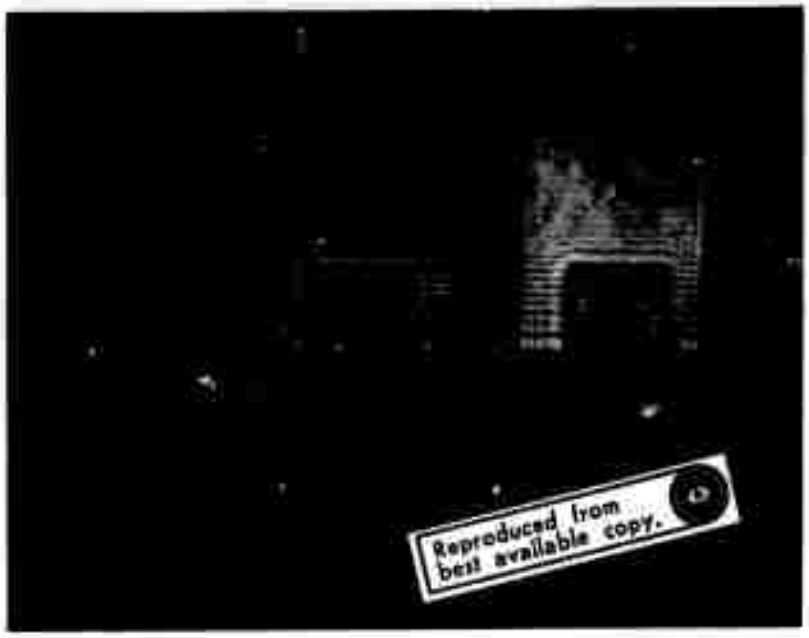

(a)

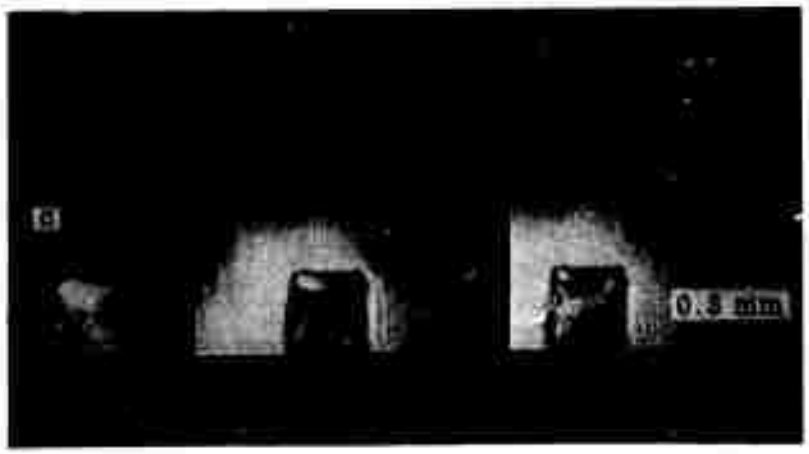

(b)

Fig. 3-18 Birefringence Extinction Pattern of $LiNbO_3$ Crystals at Three Settings of Compensator. (a) Typical crystal cut at LMSC, dimensions 0.25 by 0.3 by 5 mm, extinction ratio 20 dB over the dark area. (b) Typical crystal supplied by vendors, dimensions 0.3 by 0.3 by 7 mm, extinction ratio 16 dB

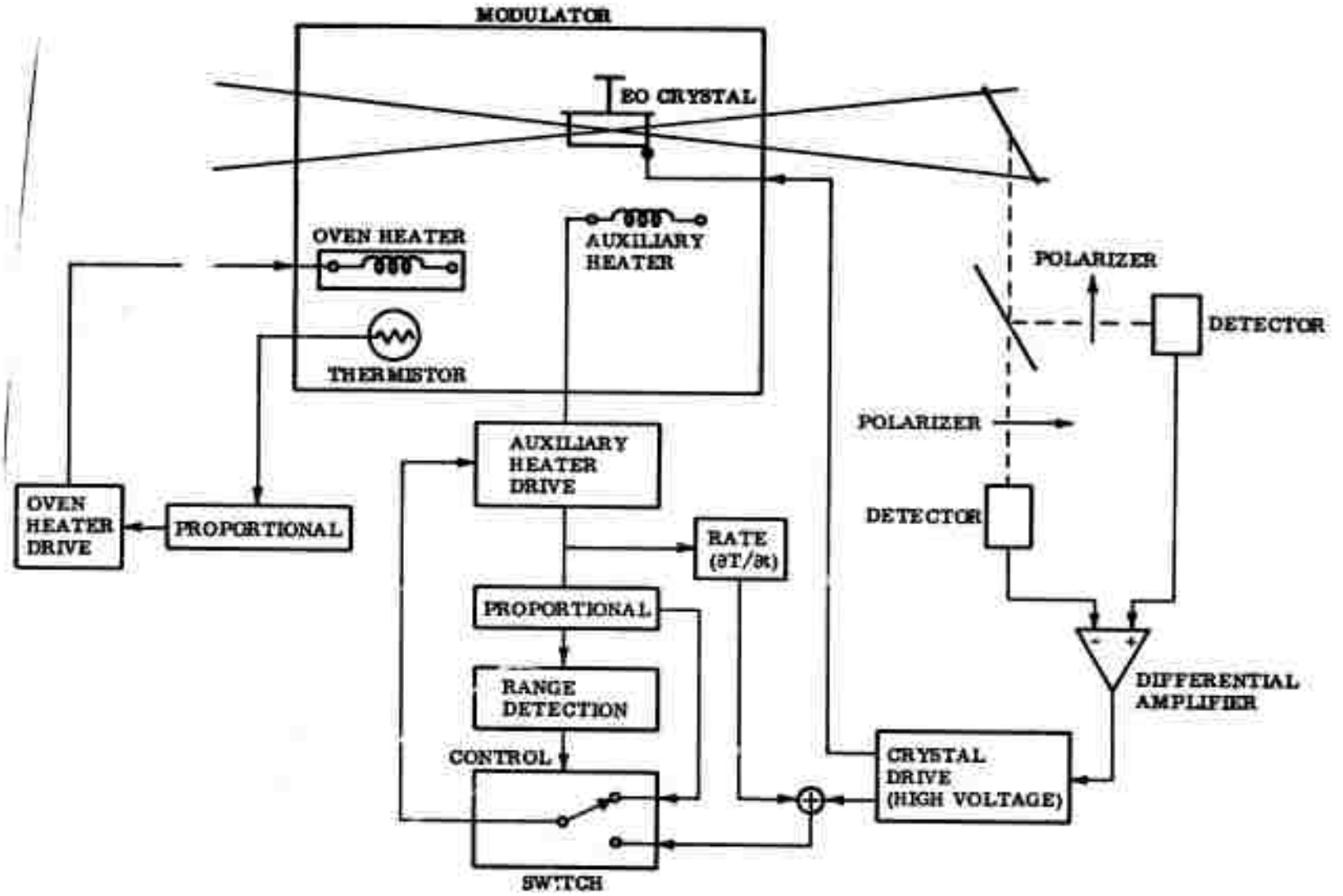

Fig. 3-19 Block Diagram of the Modified Electrooptic/Thermal Control Unit

LOCKHEED PALO ALTO RESEARCH LABORATORY
LOCKHEED MISSILES & SPACE COMPANY
A GROUP DIVISION OF LOCKHEED AIRCRAFT CORPORATION

gross error can be compensated for thermally. It has been found that the temperature increase of the crystal is approximately proportional to the auxiliary heater power. Therefore, no additional sensing is necessary; the proportional control in the auxiliary heater loop is essentially a power monitor. The oven control is then entirely separate, being controlled by a preset proportional controller to within $\pm 0.1°C$.

Unfortunately, because of the problem encountered with the dc blocking in the modulator tuning, this controller has not yet been tested in an actual operating environment.

3.2.4 Crystal Damage Test

During this quarter it was suggested that the newly available, clear $LiTaO_3$ crystals had low susceptibility to optical damage at room temperature. In fact, it was informally reported that no damage at tens of kilowatts per square centimeter intensity at 0.5145 μm had been seen. LMSC obtained the same type of crystal and performed measurements on the sample at 0.5145 and 0.4880 μm. It was found that damage resulted at room temperature even at 3.6 kW/cm^2 for continuous exposures as short as a fraction of a second, and long and slowly sweeping exposures. The results obtained are shown in Fig. 3-20. Three settings of the static compensator were used to make the damage more evident. The lower dots were made at 3.6 kW/cm^2, while the large central dot was made at 24.8 kW/cm^2. It is clear from the picture that damage is readily effected in $LiTaO_3$ at room temperature at these power densities.

The earlier measurement we made on $LiNbO_3$ showed that it would not be damaged at 14 kW/cm^2 if it is held at 180°C. There appears to be no reason for LMSC to use $LiTaO_3$ instead of $LiNbO_3$ at this time, since both crystals must be kept in an oven, and since the optical quality of $LiTaO_3$ crystals we have received is not as high as the $LiNbO_3$ crystals.

Fig. 3-20 Birefringence Pattern of Examples of Optical Damage in $LiTaO_3$ at Room Temperature: Laser Wavelength, 0.5145 and 0.4880 μm. Large spot near center: damage at 24.8 kW/cm^2. Smaller spots near lower edge; damages at 3.6 kW/cm^2. Other spots were results of intermediate intensity and varying exposure times (all in seconds)

Section 4
CONCLUSIONS AND RECOMMENDATIONS

4.1 SINGLE-FREQUENCY LASER STUDIES

The following advances in the state-of-the-art were made during the past year.

(1) Techniques for the deposition of thin nichrome films (~ 25 to 100Å) were developed and measurements were made of their reflection and transmission coefficients. Satisfactory agreement with theoretical values was obtained.

(2) Single- and double-nichrome film mode filters were fabricated and tested for the single-frequency operation of Nd:YAG lasers.

(3) A two-component, tilted intracavity Fabry-Perot etalon and nichrome film mode filter with low insertion loss was devised. This is a good practical solution for the single-frequency operation of Nd:YAG laser at all nominal levels of laser gain and with good efficiency.

(4) The insertion loss of the tilted Fabry-Perot etalon was investigated theoretically and experimentally, and upper limits on the reflectivity of such etalons for low-loss, single-frequency operation were established. The tilt loss of the etalon was computed using the concept of an angular spectrum of plane waves constituting the model distribution of the electric field in the laser cavity. This is a useful theoretical approach which allows the deduction of the tilt loss for higher order transverse modes to be deduced and hence predicts the feasibility of using an intracavity etalon as a transverse mode filter.

(5) Laser cavities with internal focusing elements were developed and used to produce adequate TEM_{00} mode volumes in the YAG rod, and computerized solutions for such cavity designs were developed.

(6) Using a Nd:YAG rod with a curved end as an internal focusing element, together with a 5-cm-radius mirror, the TEM_{oo} beam radius in the rod was made greater than 1 mm. At present a single-frequency output of 0.8 W has been obtained from a low-gain (25%) Nd:YAG laser pumped by a 1-kW tungsten lamp. Some instability with the use of short radius laser rods and mirrors has been encountered with the intracavity tilted Fabry-Perot etalon. Further elucidation of this should allow the objective of 1-W single-frequency output at 1.06 μm to be attained.

(7) Additional investigation of single-frequency techniques shows that the two-component tilted F-P etalon, nichrome-film mode filter is the best practical solution for single-frequency operation in conventional standing-wave resonant cavities. Such a filter allows adequate cavity designs for good TEM_{oo} mode volumes in the laser rod. Its chief disadvantage – spatial hole burning – may be overcome by the use of a traveling wave ring-type laser as deduced earlier, but the full promise of this method depends on obtaining low-loss elements – Faraday rotators and polarizers – together with the same adequate TEM_{∞} mode volumes in the Nd:YAG rod.

(8) A paper on "Two-Component-Mode Filters for Optimum Single-Frequency Operation of Nd:YAG Lasers," was written on some of this work and appeared in the IEEE Journal of Quantum Electronics, Vol. QE-7, Aug 1971, pp. 381–387.

During the second phase of this program additional work in the following areas will be done:

(1) Further work on the design and operation of efficient resonant cavity Nd:YAG lasers with internal focusing elements, including the use of convex short-radius mirrors to obtain adequate TEM_{oo} mode volumes in the rod with shorter lasers and improved mode stability.

(2) Further optimization of the tilted Fabry-Perot etalon – nichrome film mode for use with short-radius mirrors and investigations on the modifications of the mode angular plane wave spectra and field distributions caused by such tilted etalons, with particular reference to the instabilities encountered within short-radius laser mirrors and rod curvatures.

(3) Measurements of the intracavity lasers, single-pass gains, and saturation parameters of optimum laser designs.

(4) Further work in the heat balance and efficient use of the potassium-rubidium lamp pump source in 8-in.-diameter spherical pump cavities. Use of appropriate selective reflective coatings in the pump cavity and cooling for efficient heat control and pumping of the Nd:YAG laser.

(5) Investigation of the thermal birefringence effects in the Nd:YAG rod when pumped by the potassium-rubidium lamp in such efficient spherical pump cavities. Other birefringent-host materials such as yittrium aluminate (YALO) will also be considered for final efficient laser designs.

4.2 OPTICAL MODULATOR STUDIES

Theoretical studies performed during this year have shown that to obtain high efficiency optical modulation (high modulation depth per unit bandwidth per unit power), the interdigital bandpass modulator must be designed to have low output impedance while maintaining the desired bandwidth. However, this results in an increase in attenuation ripple within the passband. Therefore, the proper design represents an optimization of all these factors.

For this study, an output impedance of 19 Ω has been chosen for a 4-section modulator, resulting in 0.5-dB attenuation ripple within the desired 1- to 2-GHz band. Two models of modulators and transformers have been designed, fabricated, and tested during this year. The insertion loss (combination of reflection and attenuation losses) of each is about 1 dB. Allowing for the loss, the performance of each modulator agrees well with theoretical predictions. In the use of Model 2 for example, 70% modulation depth for 0.5145-μm radiation is obtained for 3.6-W of drive power flowing through the circuit, and 87% depth is obtained for 6.7-W flowing through the circuit. These depths compare well with the theoretical values of 73% and 92%, respectively. The 3-dB bandwidth is greater than 1 GHz, and it is estimated the bandwidth may be as high as 1.5 GHz (0.9 to 2.4 GHz). From these results, it is concluded that for 1.06-μm radiation, 50% modulation depth will be found at 10-W rf drive at the input of the modulator (corresponding to 7.5-W flowing through the circuit).

Interferometric modulation has also been studied. Theoretically this type of modulation promises to be more efficient than the conventional birefringence type of modulation. However, because of the crystal quality, end-faces parallelism and cutting-strains in the commercially crystals, severe beam distortion was obtained and the results were somewhat worse than the berefringence modulation. For these reasons, LMSC began an in-house supported program to study cutting and grinding procedures during the last quarter. Much higher-quality finished crystals have now been obtained.

Automatic electrooptic/thermal controller circuits for the modulator have also been designed and tested. These circuits monitor the optical bias point and produce an instantaneous high voltage to compensate for the bias point drift. At the same time, the oven or auxiliary heater power is adjusted so as to reduce the high voltage and return the modulator to its steady state. Both circuits work well.

Studies on optical damages in crystals have also been conducted. It was found that for $LiNbO_3$ crystals, intensities as high as 14 kW cm^2 (0.5145 and 0.4880 μm) did not cause damage at about 180°C, although damage was practically instantaneous at room temperature. $LiTaO_3$ showed similar behavior. The optical beam profile transmitted through the $LiNbO_3$ crystal at 180°C showed little distortion. Tests of $LiNbO_3$ in vacuum at temperatures as high as 350°C did not show any discoloration. Thus, it is concluded that no damage or distortion problems will occur with 1.0 W of 1.06-μm radiation.

In the next phase of this program, bandpass optical modulators that will operate from 2- to 4-GHz will be designed, fabricated, and tested. Particular attention will be given to the rf insertion loss problem since such losses may well be even more severe than were found for the 1- to 2-GHz modulators. A further study will also be made on ways to apply a dc bias voltage without perturbing the rf or modulation characteristics.

Section 5
REFERENCES

2-1 W. Culshaw, "High Resolution Millimeter Wave Fabry-Perot Interferometer," IEEE Trans. Microwave Theory and Techniques, Vol. MTT-8, Mar 1960, pp. 182 – 189

2-2 L. Brilloiun, Wave Propagation in Periodic Structures, New York, Dover, 1953, pp. 193 – 226

2-3 M. Born and E. Wolf, Principles of Optics, New York, Pergamon, 1969, pp. 65 – 69

2-4 P. W. Smith, M. V. Schneider, and H. G. Danielmeyer, "High Power Single Frequency Operation of Gas and Solid State Lasers With Thin Metal Film Mode Selection Filters," Bell System Tech. J., Vol. 68, May/Jun 1969, pp. 1405 – 1419

2-5 J. E. Gensic et al., "Continuous 0.533 μm Solid-State Source Using $Ba_2NaNb_3O_{15}$," Appl. Phys. Lett., Vol. 12, May 1968, pp. 306 – 308

2-6 K. Kogelnik and T. Li, "Laser Beams and Resonators," Proc. IEEE, Vol. 54, Oct 1966, pp. 1312 – 1329

2-7 H. Kogelnik, "Imaging of Optical Modes – Resonators With Internal Lenses," Bell System Tech. J., Vol. 44, Mar 1965, pp. 455 – 494

2-8 I. Liberman, D. A. Larson, and C. H. Church, "Efficient Nd:YAG CW Lasers Using Alkali Additive Lamps," IEEE JQE, Vol. QE5, May 1969, pp. 238 – 241

2-9 D. A. Draegert, "Single Longitudinal Mode Nd:YAG Laser," 1971 IEEE/OSA Conference of Laser Engineering and Applications. Digest of Papers IEEE JQE, Vol. QE7, Jun 1971, p. 300. Also private communication

2-10 V. Evtuhov and A. E. Siegman, "A Twisted Mode Technique for Obtaining Axially Uniform Energy Density in the Laser Cavity," Appl. Optics, Vol. 4, Jun 1965, pp. 142 – 143

2-11 H. G. Danielmeyer and W. G. Nilsen, "Spontaneous Single-Frequency Output From a Spatially Homogeneous Nd:YAG Laser," Appl. Phys. Lett., Vol. 16, 1 Feb 1970, pp. 124 – 126

2-12 H. G. Danielmeyer and E. H. Turner, "Electrooptic Elimination of Spatial Hole Burning in Lasers," Appl. Phys. Lett., Vol. 17, 15 Dec 1970, pp. 519 – 521

3-1 G. L. Matthaei et al., Microwave Filters, Matching Networks and Coupling Structures, McGraw-Hill, New York, 1964

3-2 S. Gussow and G. Weathers, Computer-Aided Filter Design Manual, NASA SP-3049, Contract NAS 8-20055, Sperry Rand Corporation, Huntsville, Ala., 1969

3-3 G. L. Matthaei, "Design of Wide-Band (and Narrow-Band) Band-Pass Microwave Filters on the Insertion Loss Basis," IRE Trans. Microwave Theory & Tech., Vol. MTT-8, Nov 1960, pp. 580 – 593

3-4 G. L. Matthaei, "Interdigital Band-Pass Filters," IRE Trans. Microwave Theory & Tech., Vol. MTT-10, Nov 1962, pp. 479 – 491

3-5 G. L. Matthaei et al., Microwave Filters and Coupling Structures, Final Report, SRI Project 3527, Contract DA 36-039-SC-87398, Stanford Research Institute, Menlo Park, Calif., Feb 1963

3-6 W. J. Getsinger, "Coupled Rectangular Bars Between Parallel Plates," IRE Trans. Microwave Theory & Tech., Vol. MTT-10, Jan 1962, pp. 65 – 72

3-7 K. K. Chow and W. B. Leonard, "Efficient Octave Bandwidth Microwave Light Modulators," IEEE JQE, Vol. QE-6, Dec 1970, pp. 789 – 793

3-8 H. W. Bode, Network Analysis and Feedback Amplifier Design, D. Van Nostrand, New York, 1945

3-9 G. L. Matthaei, "Short-Step Chebyshev Impedance Transformers," IEEE Trans. MTT, Vol. MTT-14, Aug 1966, pp. 372 – 383